ARCHER, CATHRO & ASSOCIATES (1981) LIMITED
1016 - 510 West Hastings Street
Vancouver, B.C. V6B 1L8
Telephone: 604-688-2568 Fax: 604-688-2578

ASSESSMENT REPORT

describing

AIRBORNE VTEM AND MAGNETOMETER SURVEYS

at the

CARIBOU CREEK PROPERTY

CC 7-30	YB89118-YB89141
31-44	YB89977-YB89990
45-54	YB91616-YB91625

NTS 105C/01 & 08
Latitude 60º16´N; Longitude 132º03´W

in the
Watson Lake Mining District,
Yukon Territory

prepared by

Archer, Cathro & Associates (1981) Limited

for

TARSIS CAPITAL CORP.

by

William A. Wengzynowski, P.Eng.

March 2009

TABLE OF CONTENTS

	Page
INTRODUCTION	1
PROPERTY LOCATION, CLAIM DATA AND ACCESS	1
HISTORY AND PREVIOUS WORK	1
GEOMORPHOLOGY	2
GEOLOGY	2
MINERALIZATION AND GEOCHEMISTRY	3
GEOPHYSICAL SURVEYS	4
DISCUSSION AND CONCLUSIONS	5
REFERENCES	6

APPENDICES

I STATEMENTS OF QUALIFICATIONS

II GEOPHYSICAL REPORT BY GEOTECH LTD.

III GEOPHYSICAL REPORT BY CONDOR CONSULTING INC.

FIGURES

No.	Description	Follows Page
1	Property Location	1
2	Claim Locations	1
3	Tectonic Setting	2
4	Regional Geology	2
5	Property Geology	3
6	Copper Geochemistry	3
7	Gold Geochemistry	3
8	Silver Geochemistry	3
9	Lead Geochemistry	3
10	Zinc Geochemistry	3
11	VTEM: β-Field	4
12	VTEM: Total Magnetic Intensity	4

TABLES

		Page
I	Main Lithological Units	3

INTRODUCTION

The Caribou Creek property hosts a cluster of copper-lead-zinc soil geochemical anomalies believed to be associated with volcanogenic hosted massive sulphide (VHMS) style mineralization. The property is located in south-central Yukon and is owned 100% by Tarsis Capital Corp.

This report describes historical work and the results of a 2008 helicopter-borne versatile time domain electromagnetic (VTEM) geophysical surveys conducted by Geotech Ltd. on behalf of Tarsis. The author's Statement of Qualifications appears in Appendix I.

PROPERTY LOCATION, CLAIM DATA AND ACCESS

The Caribou claims are located in the southern end of the Englishman Range in the Cassiar Mountains of south-central Yukon, 180 km east of the community of Whitehorse and 180 km west of the community of Watson Lake at latitude 60□16´N and longitude 132□03´W on NTS map sheet 105C/01 and 105C/08 (Figure 1).

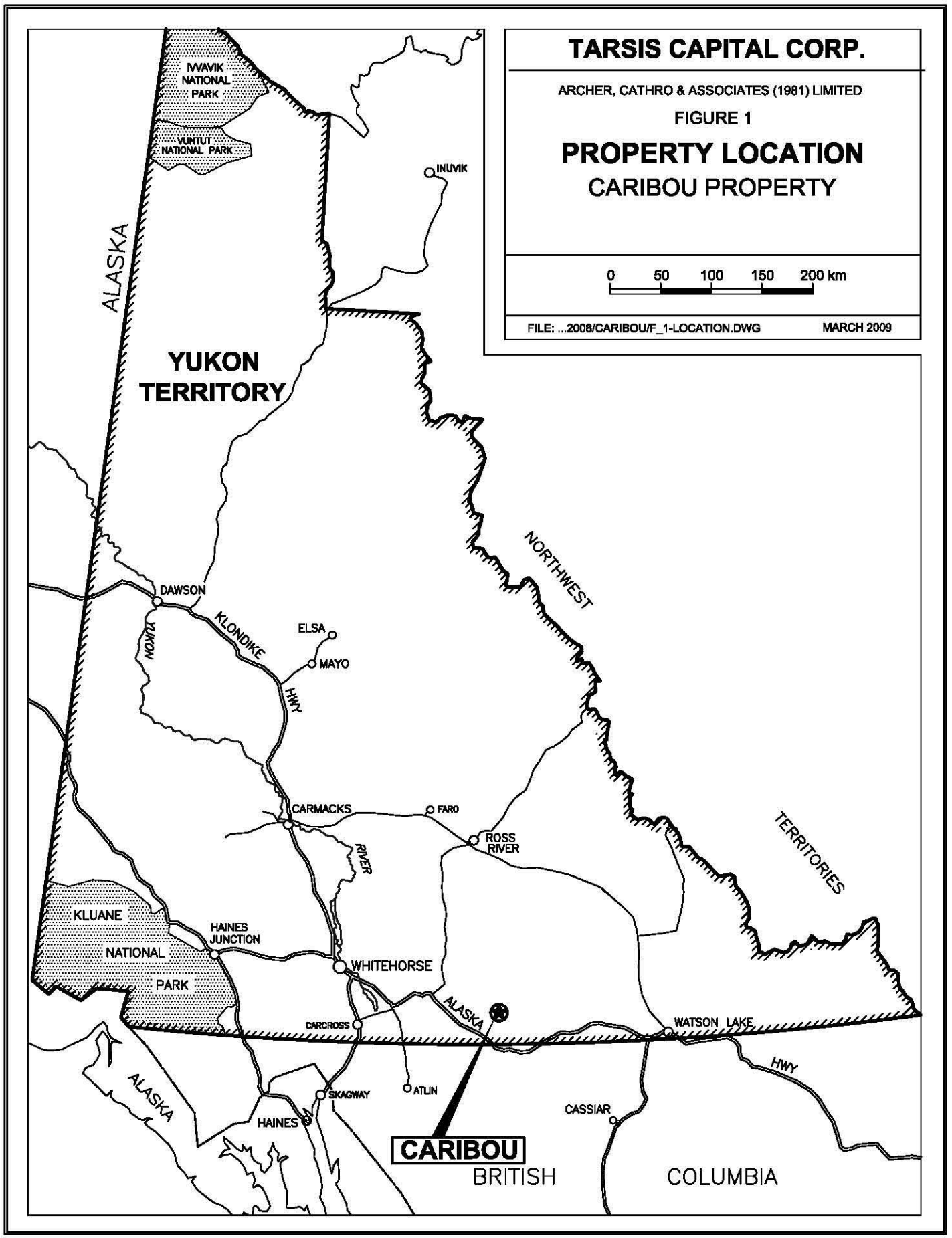
The property comprises 48 contiguous mineral claims covering approximately 1000 ha. All of the claims are registered with the Mayo Mining Recorder in the name of Tarsis. Claim registration data are listed below while the locations of individual claims are shown on Figure 2.

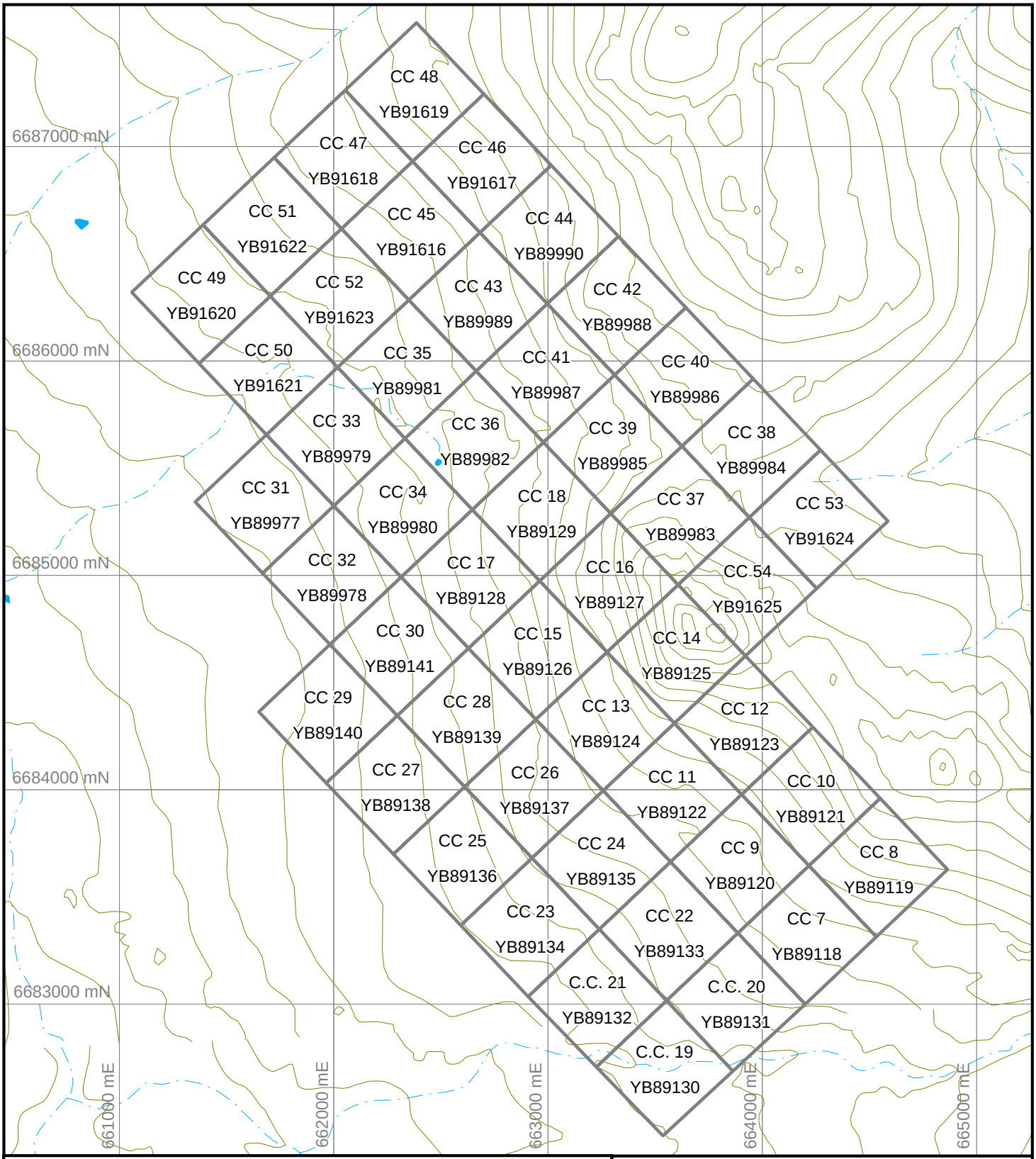
Claim Name	Grant Number	Expiry Date*
CC 7-30	YB89118-YB89141	April, 2014
31-44	YB89977-YB89990	April, 2014
45-54	YB91616-YB91625	April, 2014

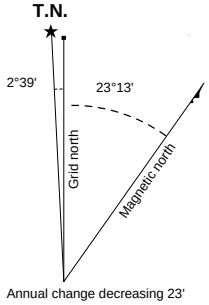
* Expiry date includes 2008 work which has been filed for assessment.

HISTORY AND PREVIOUS WORK

In 1980 reconnaissance level geochemical sampling was conducted by Cordilleran Engineering for Regional Resources limited. This work identified strong multi-element silt and soil geochemical anomalies and a small gossan in bedrock with significant levels of copper, lead and zinc. Follow up exploration consisted of reconnaissance level sampling by Fairfield Minerals Ltd. in 1996 and staking in 1997. The 1997 field program conducted by Fairfield included an 85 line-km airborne electromagnetic and magnetic survey, a 3 line-km ground IP survey, grid soil sampling for a total of 661 samples, and reconnaissance and follow-up sampling for a total of 8 soil samples, 6 silt samples and 11 rock samples. In 1998 Fairfield continued exploration with infill soil sampling, blast trenching and sampling of two new Showings plus additional prospecting. The claims were optioned from Fairfield in 1999 by Brett Resources Inc. which inspected the two showings and conducted additional geological mapping.


TARSIS CAPITAL CORP.
ARCHER, CATHRO & ASSOCIATES (1981) LIMITED
FIGURE 1
PROPERTY LOCATION
CARIBOU PROPERTY
0 50 100 150 200 km
FILE: ...2008/CARIBOU/F_1-LOCATION.DWG
MARCH 2009
IVVAVIK NATIONAL PARK
VUNTUT NATIONAL PARK
INUVIK
ALASKA
YUKON TERRITORY
NORTHWEST
TERRITORIES
DAWSON
YUKON
KLONDIKE
HWY
ELSA
MAYO
CARMACKS
FARO
ROSS RIVER
RIVER
KLUANE NATIONAL PARK
HAINES JUNCTION
WHITEHORSE
ALASKA
CARCROSS
WATSON LAKE
HWY
ALASKA
SKAGWAY
ATLIN
HAINES
CASSIAR
CARIBOU
BRITISH COLUMBIA





TARSIS CAPITAL CORP.

FIGURE 2

ARCHER, CATHRO & ASOCIATES (1981) LIMITED

CLAIM LOCATIONS

CARIBOU PROPERTY

0 0.25 0.5 0.75 1 km

UTM ZONE 8W, NAD 83, 105 C/8 & 105 C/1

...2008/CARIBOU/FIGURES/CARIBOU_CU.WOR | DATE: MARCH 2008

GEOMORPHOLOGY

The Caribou Creek property covers approximately 1000 hectares at the southern edge of the Englishman range in the Cassiar Mountains. Topography is generally gentle to moderate with the only steep slopes occurring along the flanks of a southeast trending ridge on the east side of the claim block. Elevations range between 1100 m and 1450 m.

The claim block is drained to the south and west by tributaries of Caribou Creek and to the north and east by a series of smaller creeks, all of which ultimately flow into the Pacific Ocean via the Teslin and Yukon Rivers.

Spruce, fir and pine form dense forests at lower elevation while grassy subalpine meadows are common at higher elevation, with little vegetation above 1400 m. Grassy marsh areas with willow, dwarf birch and stunted conifers are widespread across the property. Rock outcrops occur atop the ridge on the east side of the property and intermittently at lower elevations. Most of the area below the ridgelines is blanketed by Pleistocene glacial till.

GEOLOGY

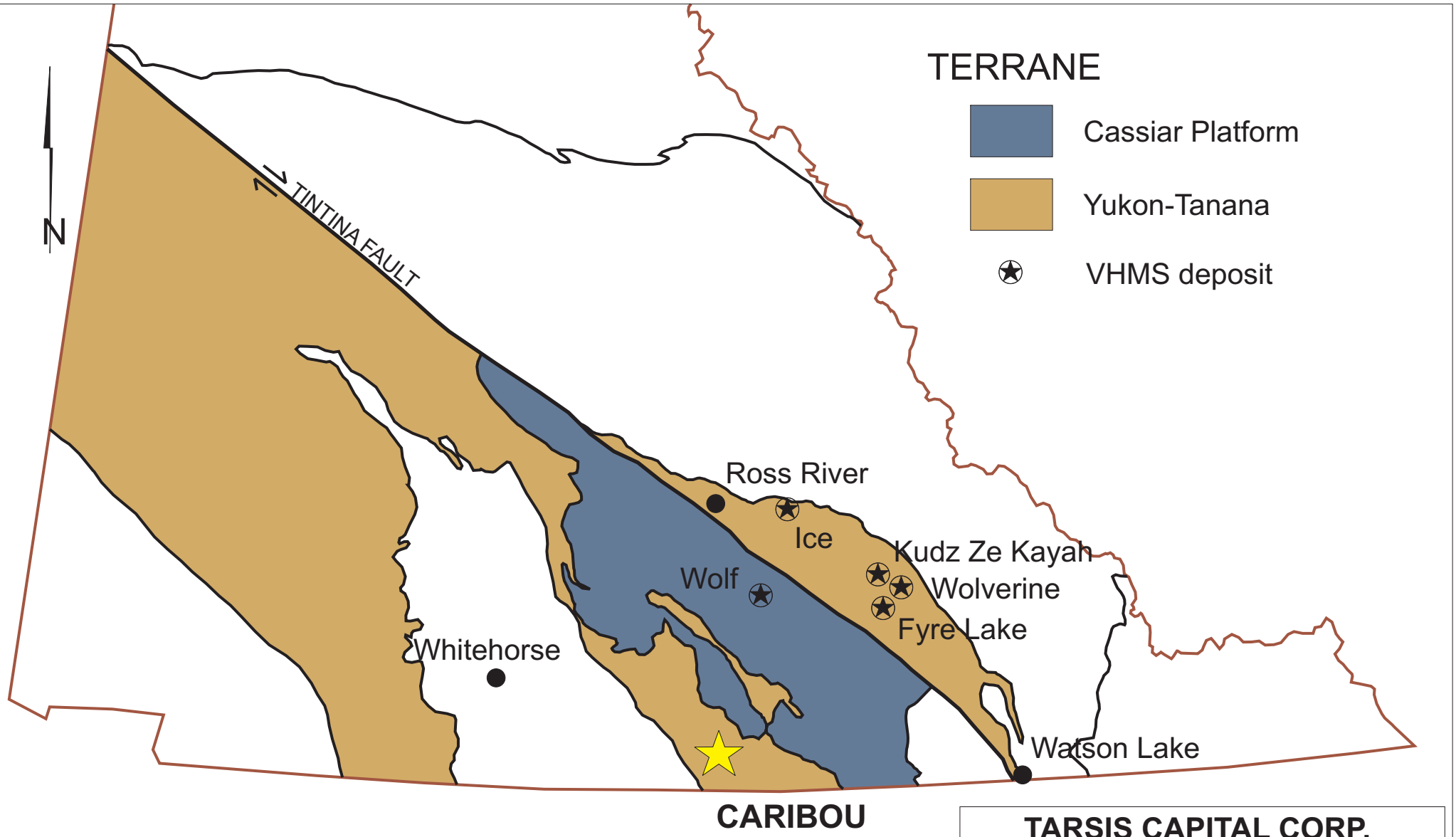
Regional Geology

The property lies within a belt of Yukon-Tanana Terrane rocks on the southwest side of the Tintina Fault Zone (Figure 3). Yukon-Tanana Terrane rocks underlie much of west-central Yukon, including a displaced block immediately northeast of the Tintina Fault Zone referred to as the Finlayson Lake District, which hosts a number of VHMS deposits and prospects.

The most recent classification of the package of rocks southwest of the Tintina Fault Zone was addressed in a special paper published by the Geological Association of Canada, 2006. This portion of the cordillera was segregated by Roots et al., 2006 into the Eastern, Central and Western belts. The latter belt hosts the Caribou Creek property and is bound by the strike-slip Teslin Fault to the west and an unnamed fault to the northeast (Figure 4).

Stratigraphic units of the western belt belong mostly to the Big Salmon Complex and comprise bimodal arc-volcanic rocks, phyllite, siliceous metasedimentary rocks and minor carbonate units. Coeval orthogneiss is common throughout the sequence and ranges in age from late Devonian to Jurassic. The upper portion of the volcanic sequence of the Big Salmon Complex is marked by a rose coloured manganiferous metachert believed to represent an exhalative volcanic pulse (Mihalynuk et al, 2006). The metavolcanic rocks of the Big Salmon Complex are considered age equivalent to the fertile Finlayson Assemblage northeast of the Tintina Fault Zone (Colpron et al, 2006).

The Klinkit Group unconformably overlies stratigraphy of the Big Salmon Complex. It consists of pale coloured marble and intermediate to mafic tuffs plus volcanic-derived metasedimentary rocks, with lesser volcanic flows, quartz sandstone and interlayered dark siltstone. Volcanic rocks are more abundant near the base of the succession. These sequences were deposited between Middle Mississippian to Permian.



TARSIS CAPITAL CORP.

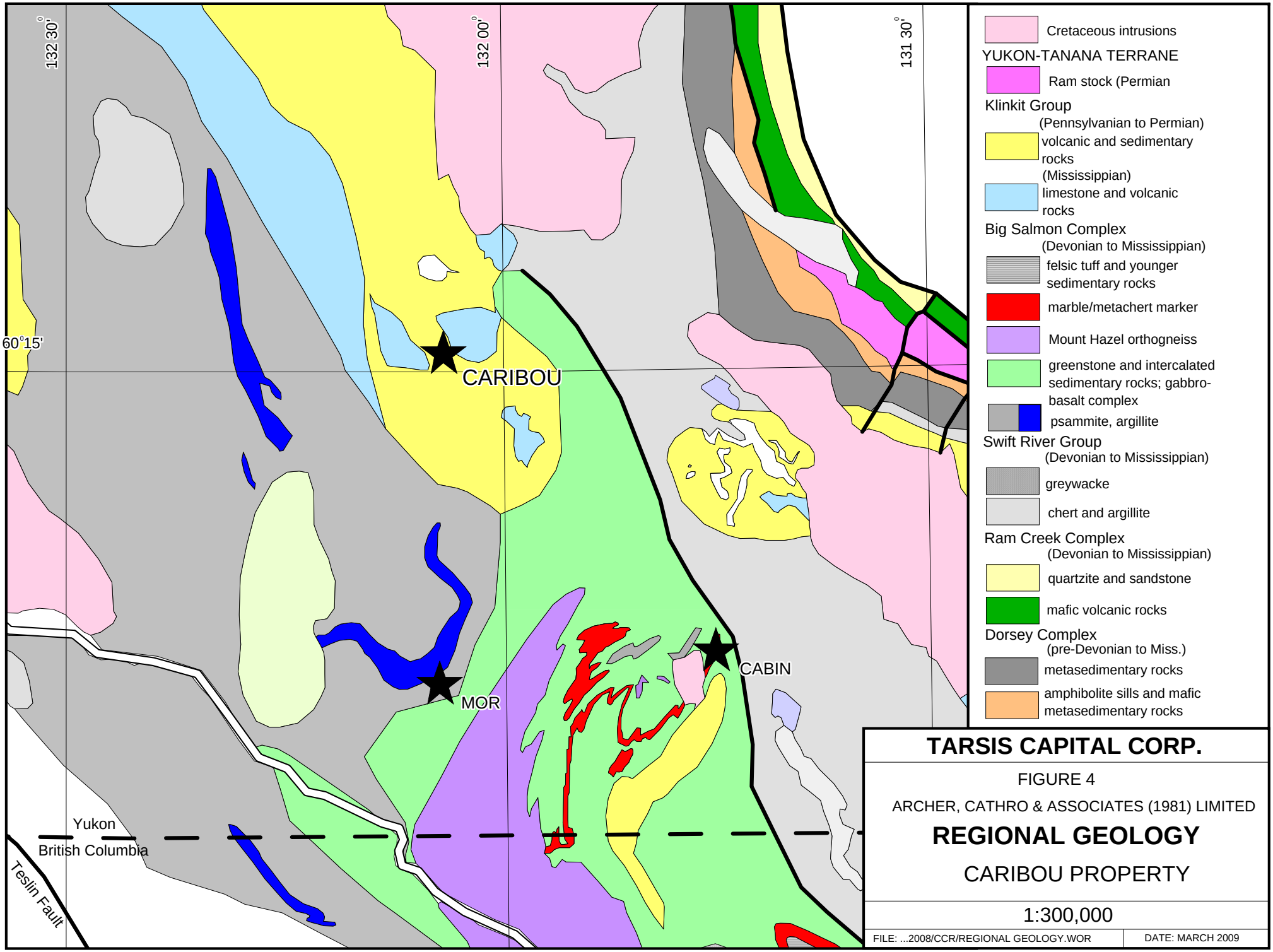
ARCHER, CATHRO & ASSOCIATES (1981) LIMITED

FIGURE 3

TECTONIC SETTING

CARIBOU CREEK PROPERTY

..FILE\: ...2008/CARIBOU/F_3-TEC.CDR DECEMBER 2008



TARSIS CAPITAL CORP.

FIGURE 4

ARCHER, CATHRO & ASSOCIATES (1981) LIMITED

REGIONAL GEOLOGY

CARIBOU PROPERTY

1:300,000

FILE: ...2008/CCR/REGIONAL GEOLOGY.WOR | DATE: MARCH 2009

The main lithologies in the vicinity of the Caribou Creek property are summarized on the following table:

Table I - Main Lithological Units

Quarternary Overburden	Glacial till, lateral and terminal moraines and glaciofluvial outwash
Mid-Cretaceous or Early Tertiary Cassiar Suite	Granodiorite and biotite-quartz monzonite porphyry
Pennsylvanian to Permian Klinkit Group	Volcaniclastic and sedimentary rocks
Mississippian Klinkit Group	Limestone and volcanic rocks
Devonian to Mississippian Big Salmon Complex	Greenstone and intercalated sedimentary rocks

(Roots et al, 2006)

Property Geology

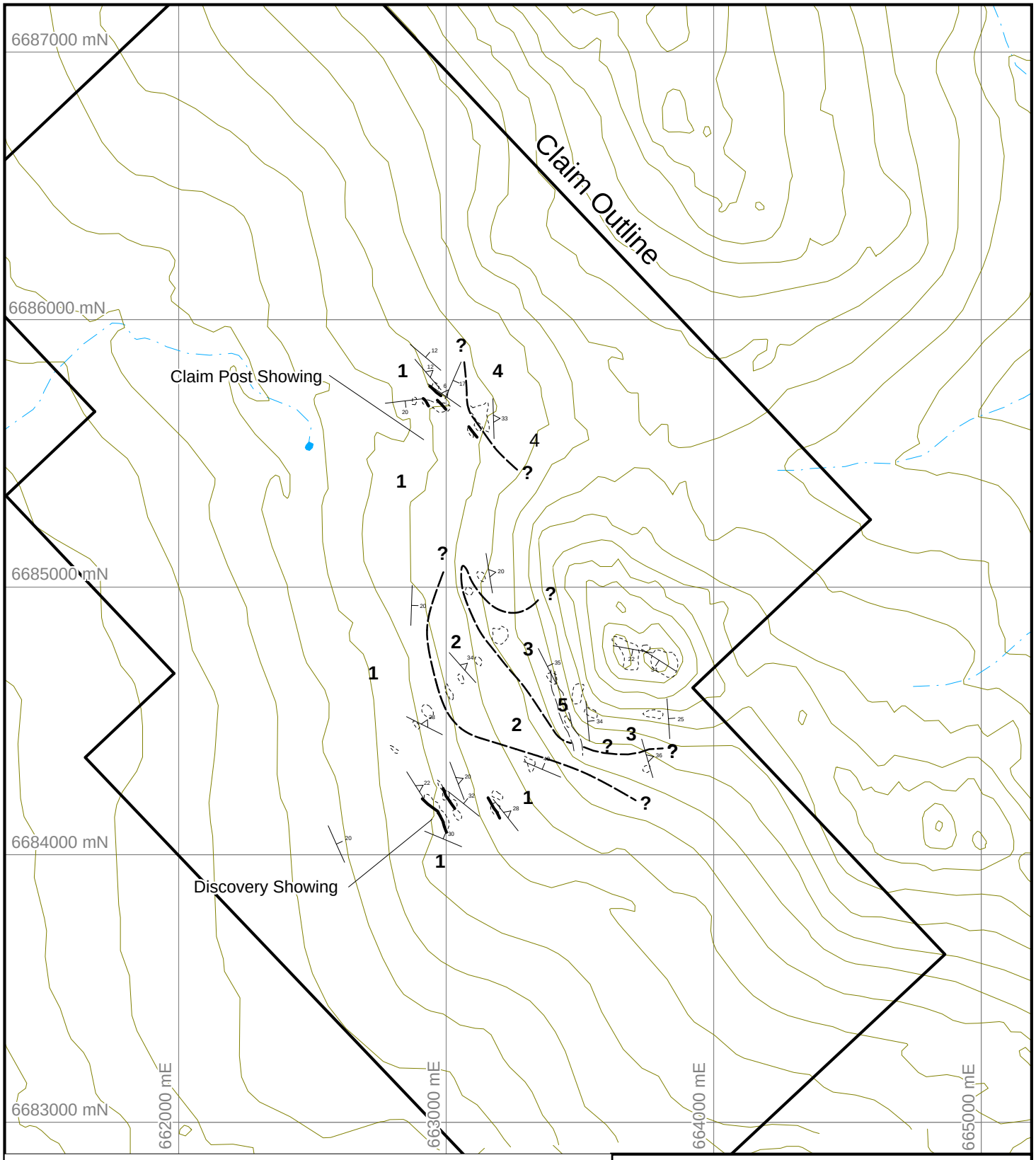
The Caribou Creek property is largely underlain by undifferentiated metavolcaniclastic schist, meta chert, and marble of the Klinkit Group (Figure 5). These rocks strike northwest and dip gently to the northeast. As noted by Bradshaw, 1999, the most widespread and likely the oldest rocks exposed on the property are green, banded, fine grained, well foliated, quartz chlorite schist believed to have been derived from mafic to intermediate volcanic rocks. This unit locally has foliation parallel and cross cutting calcite stringers and sparsely disseminated magnetite. Near the upper contact it contains slightly elongated quartz eyes up to seven millimeters in diameter. Other, less widespread, bands contain abundant fine grained sericite and varying coarse grained pyrite. These rocks are overlain by Mississippian aged fossiliferous marble (Ritcey, 1998). The marble is white to buff and is well exposed on the ridge on the eastern side of the property. Irregular networks of quartz veins are common in the limestone. No sampling of these veins has been reported.

A series of diorite dykes and small plugs of unknown affinity are observed to cut both of the main stratigraphies on and to the south of the property. The most abundant intrusive unit found on the property is variably chloritized, medium grained diorite dykes. The dykes cut both stratigraphic units but do not appear to have significant alteration associated with them. Minor amounts of andesite and hornblende-rich mafic porphyry talus is documented on the property.

MINERALIZATION AND GEOCHEMISTRY

During 1997 and 1998 Fairfield collected a total of 1730 soil samples over a roughly 6 km^2 grid (Figures 6 to 10).

This sampling identified intermittent clusters of anomalous Cu-Pb-Zn-Ag-Au values trending approximately northwest across the central part of the property parallel to the trend of local stratigraphy. The strongest and most cohesive Cu-Pb-Zn response is located in the southwest



T.N.

2°39'

23°13'

Grid north

Magnetic north

Annual change decreasing 23'

1 Green banded fine grained quartz chlorite schist / mafic intermediate tuff

2 Light green-grey siliceous quartz-chlorite schist / mt-felsic crystal tuff

3 Dark grey-white thinly bedded limestone

4 Greenish Grey aphanitic meta-chert

5 Dark green mafic dyke

Pyritic quartz sericite schist horizon

Geological contact

Outcrop boundary

Strike and dip of bedding, foliation

Mineralized showing (labelled with showings name)

TARSIS CAPITAL CORP.

FIGURE 5

ARCHER, CATHRO & ASOCIATES (1981) LIMITED

PROPERTY GEOLOGY

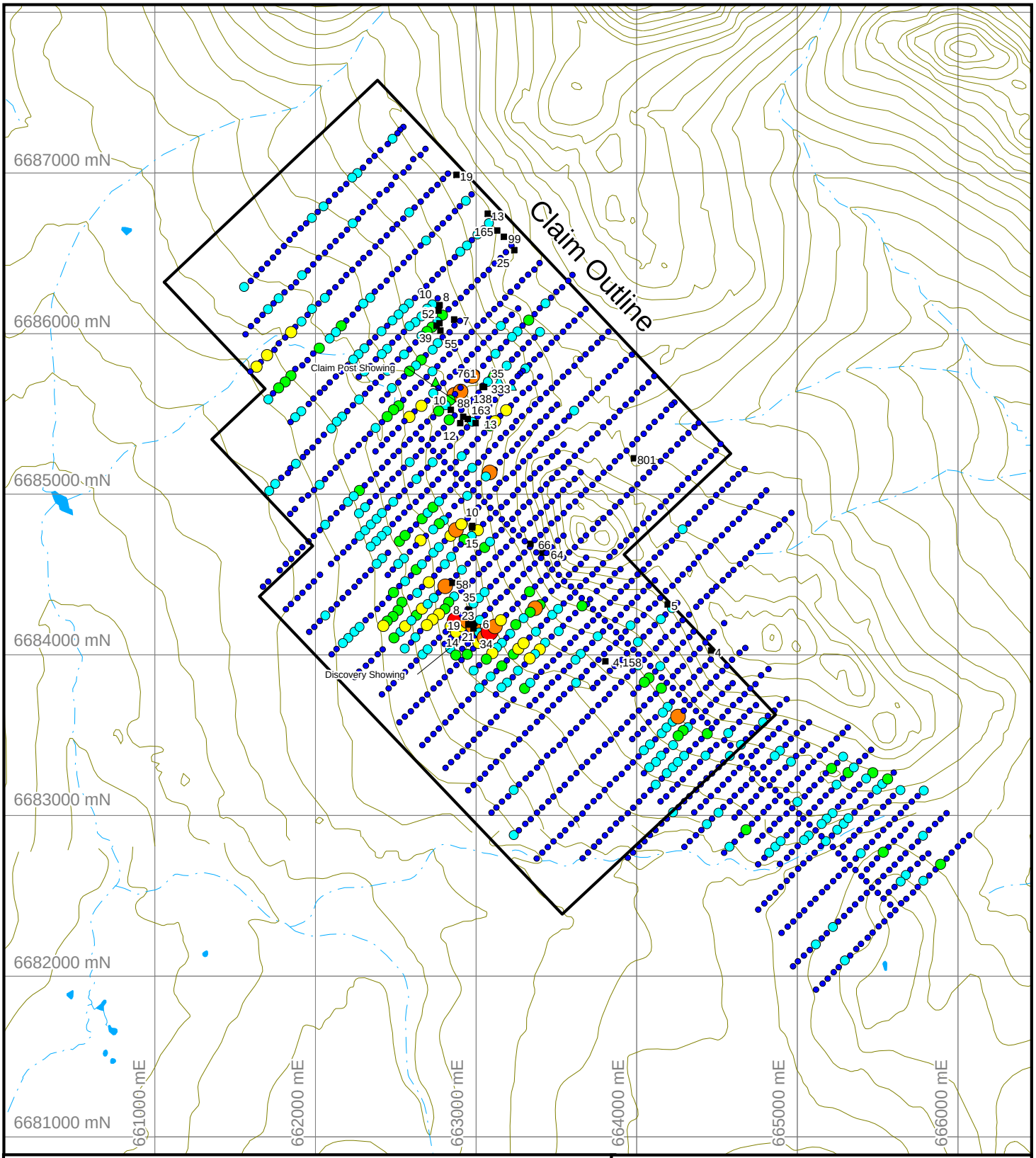
CARIBOU PROPERTY

0 0.25 0.5 0.75 1 km

UTM ZONE 8W, NAD 83, 105 C/8 & 105 C/1

...2008/CARIBOU/FIGURES/CARIBOU_geo.WOR

DATE: MARCH 2008



T.N.

2°39'

23°13'

Grid north

Magnetic north

Annual change decreasing 23'

Copper (ppm)

silt	soil	
▲	●	≥1,000
▲	●	≥500 < 1000
▲	●	≥200 < 500
▲	●	≥100 < 200
▲	●	≥50 < 100
▲	●	0 < 50

■ 8 Rock sample (ppm Cu)

TARSIS CAPITAL CORP.

FIGURE 6

ARCHER, CATHRO & ASOCIATES (1981) LIMITED

COPPER GEOCHEMISTRY

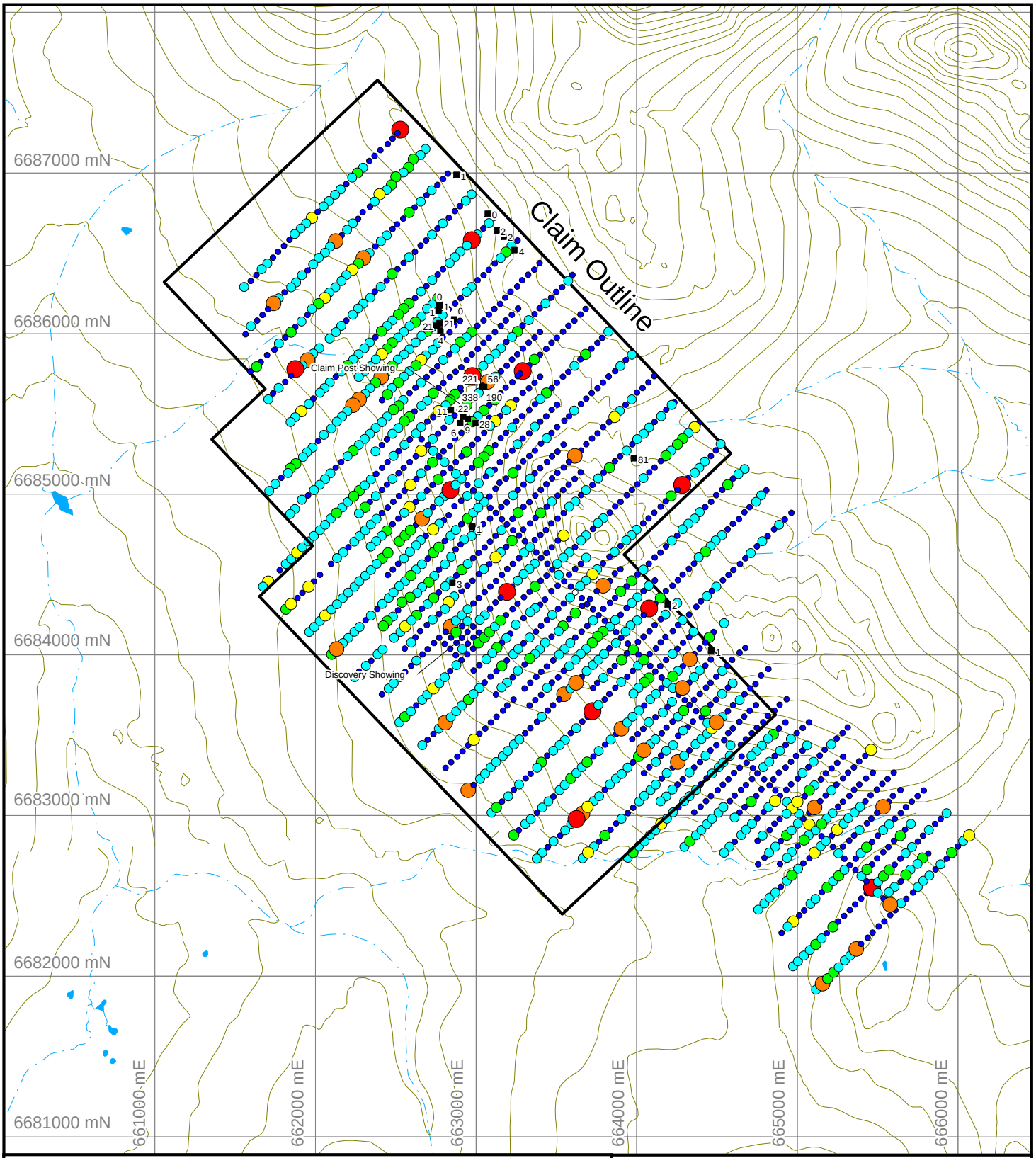
CARIBOU PROPERTY

0 0.5 1.0 1 km

UTM ZONE 8W, NAD 83, 105 C/8 & 105 C/1

...2008/CARIBOU/FIGURES/CARIBOU_Cu.WOR

DATE: MARCH 2008



T.N.

2°39'

23°13'

Grid north

Magnetic north

Annual change decreasing 23'

Gold (ppb)

soil

≥100	<	2500	
≥20	<	100	
≥10	<	20	
≥5	<	10	
≥2	<	5	
0	<	2	

■ 8 Rock sample (ppb Au)

TARSIS CAPITAL CORP.

FIGURE 7

ARCHER, CATHRO & ASOCIATES (1981) LIMITED

GOLD GEOCHEMISTRY

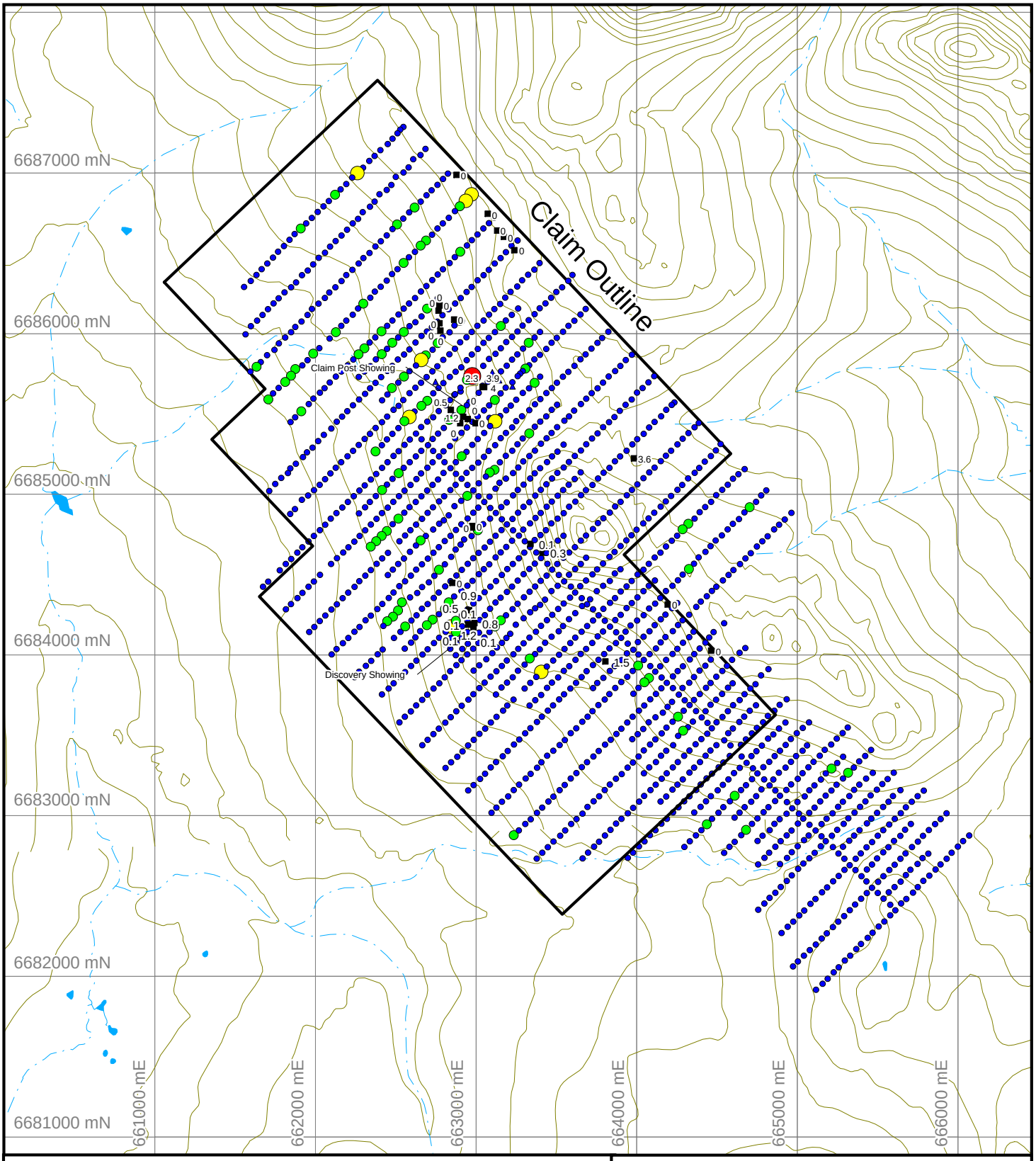
CARIBOU PROPERTY

0 0.5 1.0 1 km

UTM ZONE 8W, NAD 83, 105 C/8 & 105 C/1

...2008/CARIBOU/FIGURES/CARIBOU_Au.WOR

DATE: MARCH 2008



T.N.

2°39'

23°13'

Grid north

Magnetic north

Annual change decreasing 23'

Silver (ppm)

silt	soil	
▲	●	≥2.5 < 8.5
▲	●	≥1.0 < 2.5
▲	●	≥0.5 < 1.0
▲	●	0 < 0.5

■ 8 Rock sample (ppm Ag)

TARSIS CAPITAL CORP.

FIGURE 8

ARCHER, CATHRO & ASOCIATES (1981) LIMITED

SILVER GEOCHEMISTRY

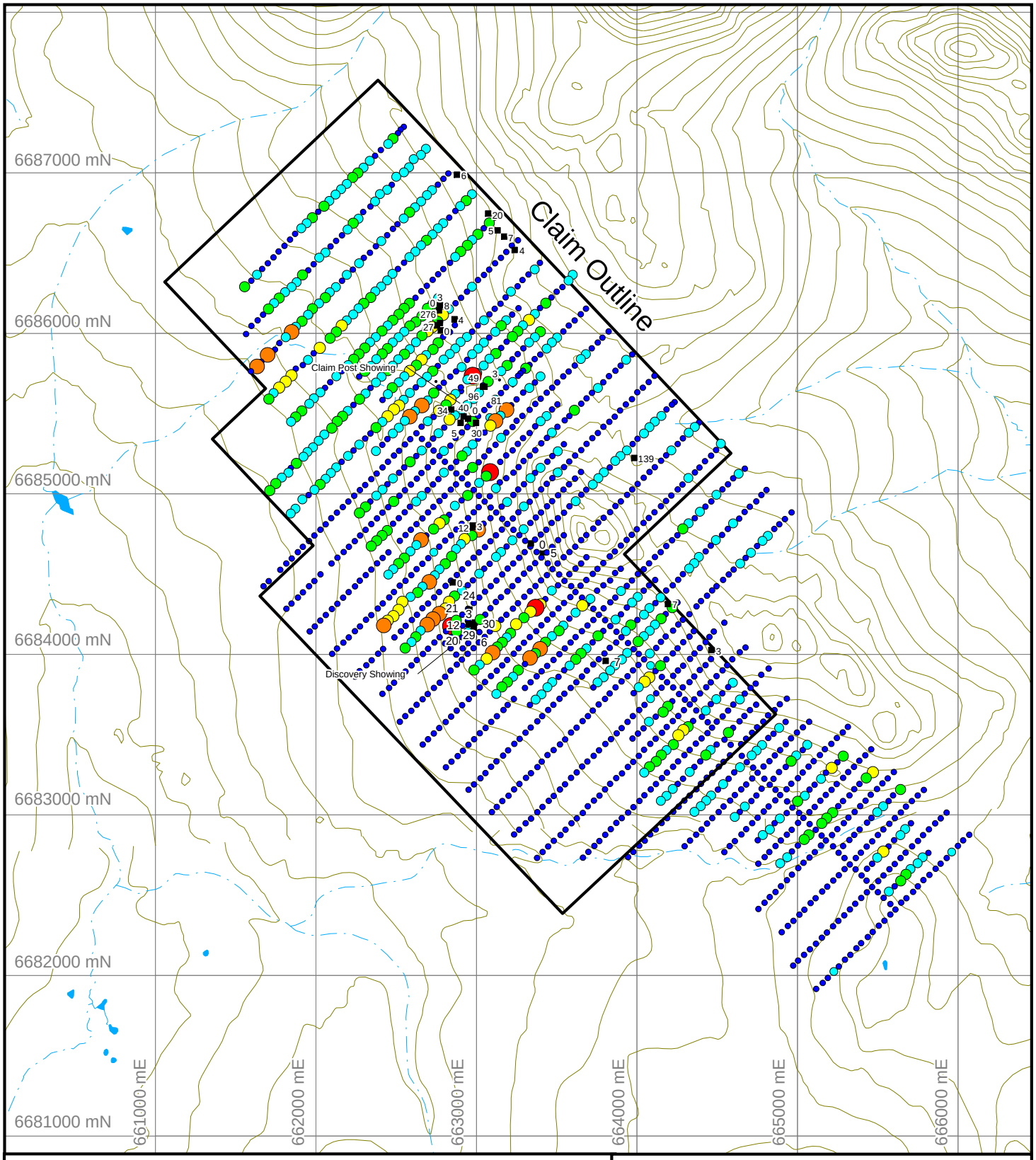
CARIBOU PROPERTY

0 0.5 1.0 1 km

UTM ZONE 8W, NAD 83, 105 C/8 & 105 C/1

...2008/CARIBOU/FIGURES/CARIBOU_Ag.WOR

DATE: MARCH 2008



T.N.

2°39'

23°13'

Grid north

Magnetic north

Annual change decreasing 23'

Lead (ppm)

silt	soil	
▲	●	≥500
▲	●	≥200 < 500
▲	●	≥100 < 200
▲	●	≥50 < 100
▲	●	≥25 < 50
▲	●	0 < 25

■ 8 Rock sample (ppm Pb)

TARSIS CAPITAL CORP.

FIGURE 9

ARCHER, CATHRO & ASOCIATES (1981) LIMITED

LEAD GEOCHEMISTRY

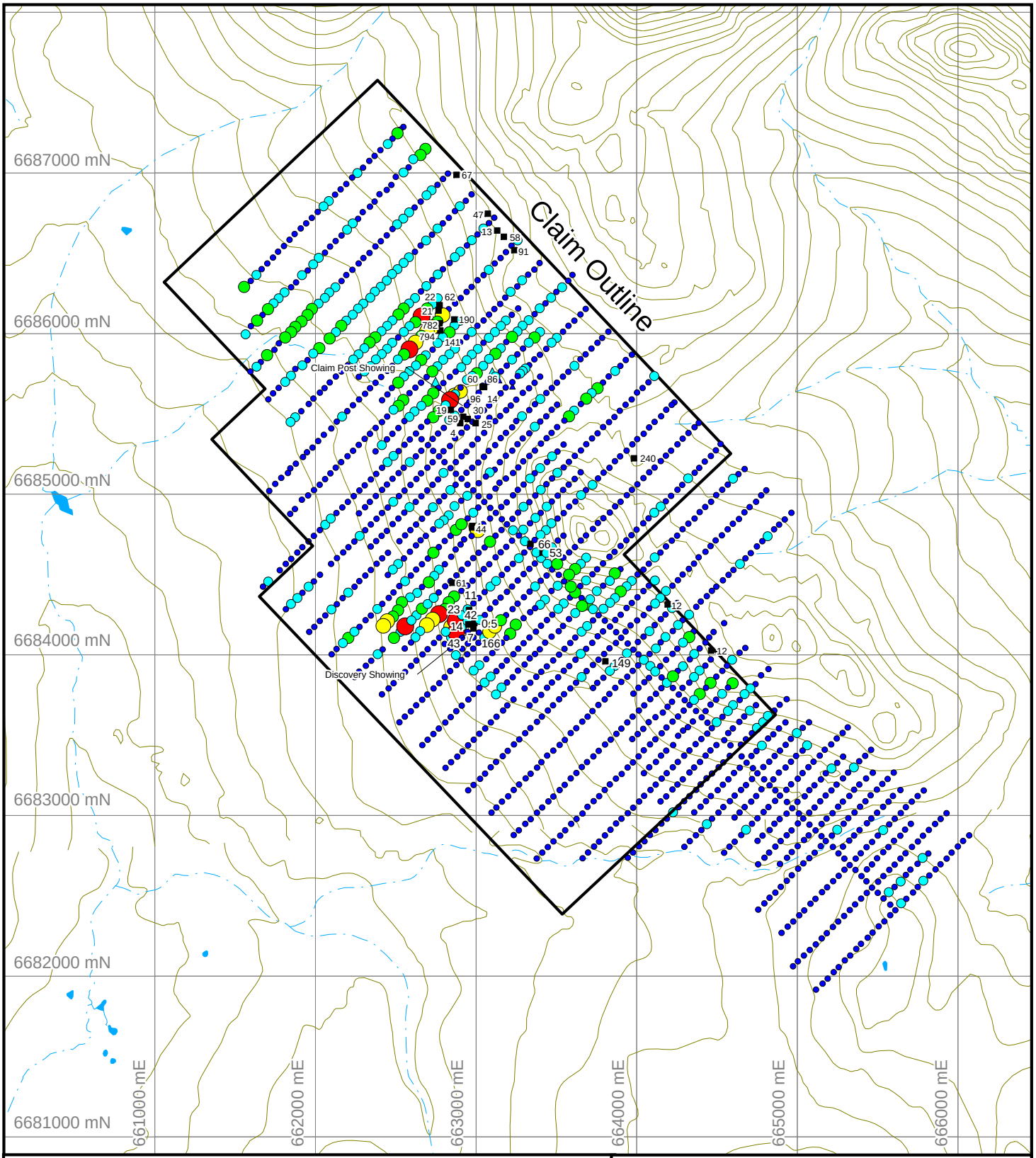
CARIBOU PROPERTY

0 0.5 1.0 1 km

UTM ZONE 8W, NAD 83, 105 C/8 & 105 C/1

...2008/CARIBOU/FIGURES/CARIBOU_Pb.WOR

DATE: MARCH 2008



T.N.

2°39'

23°13'

Grid north

Magnetic north

Annual change decreasing 23'

Zinc (ppm)

silt	soil	
		≥1,000
		≥500 < 1,000
		≥200 < 500
		≥100 < 200
		0 < 100

■ 8 Rock sample (ppm Zn)

TARSIS CAPITAL CORP.

FIGURE 10

ARCHER, CATHRO & ASOCIATES (1981) LIMITED

ZINC GEOCHEMISTRY

CARIBOU PROPERTY

0 0.5 1.0 1 km

UTM ZONE 8W, NAD 83, 105 C/8 & 105 C/1

...2008/CARIBOU/FIGURES/CARIBOU_Zn.WOR

DATE: MARCH 2008

central part of the grid and is roughly centred on the Discovery Showing. Values up to 2675 ppm Cu, 2047 Pb and 1346 ppm Zn define the core of a larger area approximately 900 by 200 m exhibiting weakly and moderately anomalous values. Numerous point anomalies for all elements mentioned are scattered elsewhere across the grid, the most notable of which coincides with the Claimpost Showing in the northwestern part of the claim block. It is geochemically defined by a point source anomaly which yielded 2320 ppb Au, 8.5 ppm Ag, 884 ppm Cu, 126 ppm Pb and 138 ppm Zn. Seven additional gold anomalies are documented across the grid with values ranging from 179 to 880 ppb.

The Discovery Showing consists of at least two gossanous pyritic felsic volcanic horizons individually exceeding 5 m thickness. Samples collected across the horizons exposed in a blast trench yielded low values for all VMS indicator elements. A cobble of semi-massive pyrrhotite collected at the eastern end of the soil geochemical anomaly defining the Discovery Showing returned 0.42% Cu with low values for all other elements. The source of the cobble was not identified.

The Claimpost Showing consists of three similar pyritic felsic volcanic horizons also exposed in blast trenches. Samples collected across mineralized exposures yielded up to 338 ppb Au, 4 ppm Ag, 761 ppm Cu, 96 ppm Pb and 96 ppm Zn (Bradshaw, 1999).

GEOPHYSICAL SURVEYS

Geophysical surveys completed over the Caribou Creek property include airborne electromagnetic and induced polarization (IP) surveys completed in 1997 and an airborne versatile time domain electromagnetic survey (VTEM) conducted in 2008. Survey specifics and the 2008 report prepared by Geotech Ltd. of Ontario are contained in Appendix III.

1997 Airborne Electromagnetic Survey

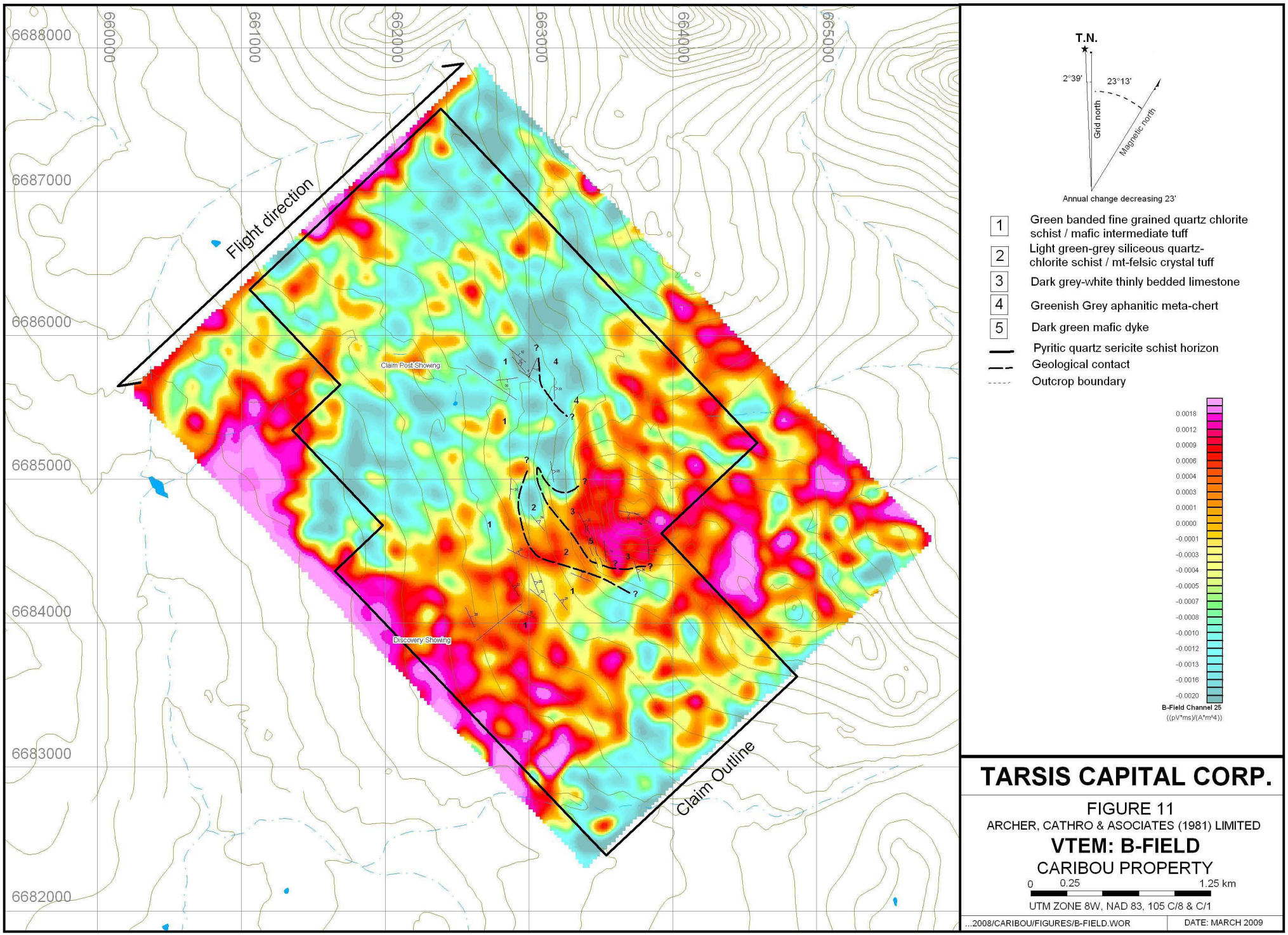
In 1997 an airborne electromagnetic survey was flown over the Caribou Creek claims by Aerodat Inc. on behalf of Fairfield. Minor magnetic highs were documented and attributed to intrusive dykes and/or felsic volcanics. Only minor conductive zones were identified and were attributed to surficial material associated with drainages and conductive alluvial.

1997 IP Survey

In 1997 an IP survey was conducted on three 1 km long lines spaced 200 m apart, over the gossan in the central part of the property. Two chargeability anomalies coincident with copper-in-soil anomalies were observed on the centre line near the Discovery Showing. Neither of the adjacent lines yielded significant chargeability response.

2008 VTEM Survey

In 2008 a 156 line km VTEM survey was conducted over the Caribou Creek claims and the immediately surrounding area. Preliminary β-field and total magnetic results (Figure 11 and 12) appear subdued in the vicinity of the two showings but the total magnetic field highlights a moderate positive anomaly over the Discovery Showing. Additional modeling was conducted by Condor Consulting Inc. of Lakewood, Colorado. This report appears in Appendix IV. Only one EM pick was selected in the northern part of the survey block following the data reduction



TARSIS CAPITAL CORP.

FIGURE 11

ARCHER, CATHRO & ASOCIATES (1981) LIMITED

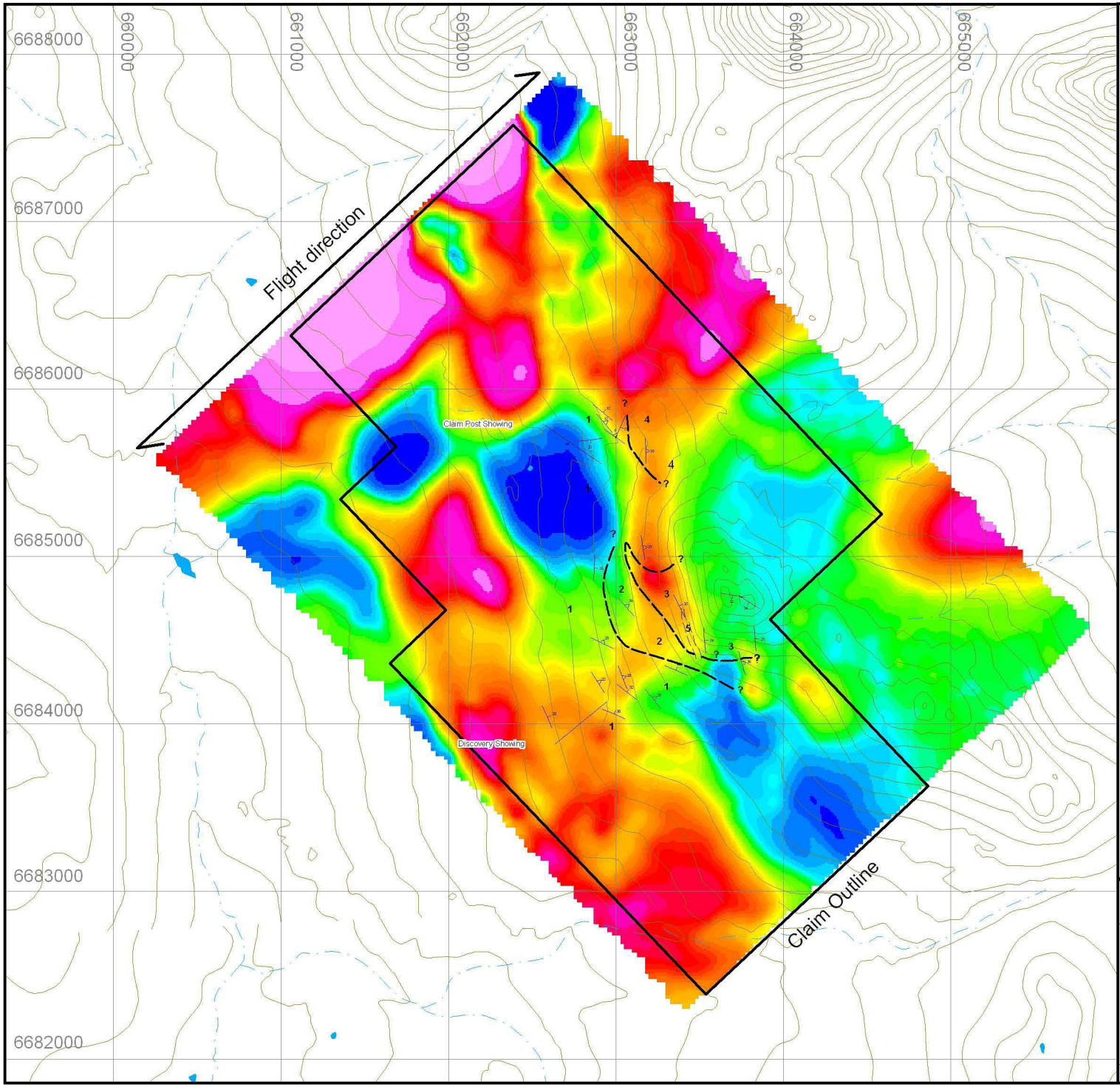
VTEM: B-FIELD

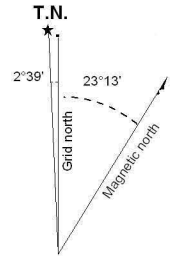
CARIBOU PROPERTY

0 0.25 1.25 km

UTM ZONE 8W, NAD 83, 105 C/8 & C/1

...2008/CARIBOU/FIGURES/B-FIELD.WOR | DATE: MARCH 2009





1 Green banded fine grained quartz chlorite schist / mafic intermediate tuff

2 Light green-grey siliceous quartz-chlorite schist / mt-felsic crystal tuff

3 Dark grey-white thinly bedded limestone

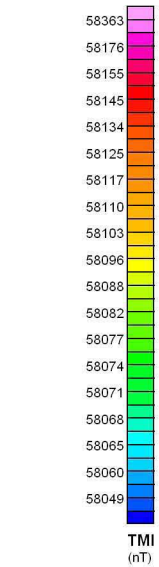
4 Greenish Grey aphanitic meta-chert

5 Dark green mafic dyke

Pyritic quartz sericite schist horizon

Geological contact

Outcrop boundary



TARSIS CAPITAL CORP.

FIGURE 12

ARCHER, CATHRO & ASOCIATES (1981) LIMITED

VTEM: TOTAL MAGNETIC INTENSITY

CARIBOU PROPERTY

0 0.25 1.25 km

UTM ZONE 8W, NAD 83, 105 C/8 & C/1

...2008/CARIBOU/FIGURES/TIM.WOR | DATE: March 2008

process. The pick coincides with a strong total magnetic field anomaly but appears to have very limited extent.

DISCUSSION AND CONCLUSIONS

The strongest soil geochemical anomalies identified on the Caribou Creek property occur in the vicinity of a gossanous felsic metavolcanic package of rocks exposed in the north and south central parts of the claim block. The elemental signatures of the soil geochemical anomalies are supportive of a VMS setting, but most samples collected from exposed mineralized volcaniclastic horizons returned low values for most VMS indicator elements. The source of a sub-rounded cobble of semi-massive pyrrhotite east of the Discovery Showing remains unexplained.

The nature of the volcanic rocks is unclear. If they are of the younger variety of arc volcanism deposited during the Pennsylvanian-Permian (Klinkit cycle), they are of differing affinity than the magmatic cycles associated with the Finlayson Assemblage equivalent rocks. This, coupled with the absence of significant geophysical conductors and supportive rock geochemistry downgrade the prospect considerably.

Additional work should be done at the Caribou property on a low priority basis in conjunction with exploration on more promising targets in the district. Obtaining zircon dates from the quartz phyric volcaniclastic units would provide confirmation of the district wide, magmatic cycle; the Klinkit cycle being less favourable than the Little Salmon or Wolverine cycle as described by Piercey et al., 2006 and Nelson et al., 2006. The existing gold anomalies identified from the historical sampling remain largely unexplained. These locations should be ground checked and the anomalies sourced by auger sampling or hand pitting.

Respectfully Submitted

Archer, Cathro & Associates (1981) Limited

William A. Wengzynowski, P.Eng.

REFERENCES

Bradshaw G.D.
1999 Report on Geological and Geochemical Surveys on the Caribou Creek Property, Yukon Territory: August 24, 1999.

Colpron M., Nelson, J. L., Murphy, D.C.
2006 A tectonostratigraphic framework for the pericroatonic terranes of the northern Cordillera, in Colpron, M. and Nelson, J.L., eds. Paleozoic Evolution and Metallogeny of Pericratonic Terranes at the Ancient Pacific Margins of North America, Canadian and Alaskan Cordillera: Geological Association of Canada, Special Paper 45, p. 1-23.

Mihalynuk, M.G., Friedman, R.M., Devine, F. and Heaman, L.M.,
2006 Protolith age and deformation history of the Big Salmon Complex, relicts of a Paleozoic continental arc in northern British Columbia, in Colpron, M. and Nelson, J.L., eds., Paleozoic Evolution and Metallogeny of Pericratonic Terranes at the Ancient Pacific Margins of North America, Canadian and Alaskan Cordillera: Geological Association of Canada, Special Paper 45, p. 179-200.

Mihalynuk M.G., Nelson J. and Friedman R.M.
1998 Regional geology and mineralization of the Big Salmon Complex (104 N NE and 104 O NW). *In*: Geological Fieldwork 1997, British Columbia Survey Branch, Paper 1998-1, p. 6-1 to 6-20.

Nelson, J.L., Colpron, M. Piercey, S.J., Dusel-Bacon, C., Murphy, D.C. and Roots, C.F.
2006 Paleozoic tectonic and metallogenic evolution of the pericratonic terranes in Yukon, northern British Columbia and eastern Alaska, in Colpron, M. and Nelson, J.L., eds., Paleozoic Evolution and Metallogeny of Pericratonic Terranes at the Ancient Pacific margin of North America, Canadian and Alaskan Cordillera: Geological Association of Canada, Special Paper 45, p. 323-360.

Piercey, S.J., Nelson, J.L., Colpron, M., Dusel-Bacon, C. Simard, R.-L. and Roots, C.F.
2006 Paeozoic magmatism and crustal recycling along the ancient Pacific margin of North America, northern Cordillera, in Colpron, M. and Nelson, J.L., eds., Paleozoic Evolution and Metallogeny of Pericratonic Terranes at the Ancient Pacific Margins of North America, Canadian and Alaskan Cordillera: Geological Association of Canada, Special Paper 45, p. 281-322.

Ritcey, D.H. and Balon, E.A
1998 1997 Geological, Geochemical and Geophysical Report on the Cabin Lake Property (CC 1-44 Claims) May, 1998

Roots, C.F., Nelson, J.L., Simard, R.-L. and Harms, T.A., 2006, Continental fragments, mid Paleozoic arcs and overlapping later Paleozoic arc and Triassic sedimentary strata is the Yukon-Tanana terrane of northern British Columbia and southern Yukon, in Colpron, M and Nelson, J.L., eds., Paleozoic Evolution and Metallogeny of Pericratonic Terranes at the Ancient Pacific Margin of North America, Canadian and Alaskan Cordillera: Geological Association of Canada, Special Paper 45, p.154-177.

APPENDIX I

STATEMENTS OF QUALIFICATIONS

STATEMENT OF QUALIFICATIONS

I, William A. Wengzynowski, geological engineer, with business addresses in Vancouver, British Columbia and Whitehorse, Yukon Territory and residential address at 301 Fairway Drive, North Vancouver, British Columbia, V7G 1L4 do hereby certify that:

1. I am President of Archer, Cathro & Associates (1981) Limited.

2. I graduated from the University of British Columbia in 1993 with a B.A.Sc in Geological Engineering, Option l, mineral and fuel exploration.

3. I registered as a Professional Engineer in the Province of British Columbia on December 12, 1998 (Licence Number 24119).

4. From 1983 to present, I have been actively engaged in mineral exploration in the Yukon Territory, Northwest Territories, northern British Columbia and Mexico.

5. I have personally participated in and supervised the fieldwork reported herein.

William A. Wengzynowski, P. Eng.

APPENDIX II

GEOPHYSICAL REPORT BY GEOTECH LTD.

REPORT ON A HELICOPTER-BORNE VERSATILE TIME DOMAIN ELECTROMAGNETIC (VTEM) GEOPHYSICAL SURVEY



CARIBOU Project

Yukon, Canada

For:

ARCHER CATHRO & ASSOCIATES LTD.

By

Geotech Ltd.

245 Industrial Parkway North

Aurora, Ont., CANADA, L4G 4C4

Tel: 1.905.841.5004

Fax: 1.905.841.0611

www.geotech.ca

Email: info@geotech.ca

Survey flown during July, 2008

Project 8077

November, 2008

TABLE OF CONTENTS

Executive Summary **3**
1. INTRODUCTION **4**
1.1 General Considerations 4
1.2 Survey Location and Specifications 5
1.3 Topographic Relief and Cultural Features 5
2. DATA ACQUISITION **7**
2.1 Survey Area 7
2.2 Survey Operations 7
2.3 Flight Specifications 8
2.4 Aircraft and Equipment 8
2.4.1 Survey Aircraft 8
2.4.2 Electromagnetic System 8
2.4.3 Airborne magnetometer 12
2.4.4 Radar Altimeter 12
2.4.5 GPS Navigation System 12
2.4.6 Digital Acquisition System 12
2.4.7 Base Station 13
3. PERSONNEL **14**
4. DATA PROCESSING AND PRESENTATION **15**
4.1 Flight Path 15
4.2 Electromagnetic Data 15
4.3 Magnetic Data 16
5. DELIVERABLES **17**
5.1 Survey Report 17
5.2 Maps 17
5.3 Digital Data 17
6. CONCLUSIONS AND RECOMMENDATIONS **21**
6.1 Conclusions 21
6.2 Recommendations 21

LIST OF FIGURES

Figure 1 - Property Location 4
Figure 2 - Google Earth Image with Flight Paths 6
Figure 3 - VTEM Configuration 9
Figure 4 - VTEM Waveform & Sample Times 9
Figure 5 - VTEM system configuration 11

LIST OF TABLES

Table 1 - Survey blocks 7
Table 2 - Survey schedule 7
Table 3 – Decay Sampling Scheme 10
Table 4 – Acquisition Sampling Rates 12
Table 5 – Geosoft GDB Data Format. 18

APPENDICES

A. Survey location maps 22
B. Survey Block Coordinates 25
C. VTEM Waveform 26
D. Geophysical Maps 27
E. Modelling VTEM Data 31

REPORT ON A HELICOPTER-BORNE VERSATILE TIME DOMAIN ELECTROMAGNETIC SURVEY

CARIBOU Project
Yukon, Canada

Executive Summary

During July 30th, 2008 Geotech Ltd. carried out a helicopter-borne geophysical survey for Archer Cathro & Associates Ltd. over one (1) block of the Caribou Project situated in the Yukon, Canada.

Principal geophysical sensors included a versatile time domain electromagnetic (VTEM) system, and a caesium magnetometer. Ancillary equipment included a GPS navigation system and a radar altimeter. A total of 156 line-kilometres were flown.

The survey operations were based out of Ross River, Yukon. In-field data quality assurance and preliminary processing were carried out on a daily basis during the acquisition phase. Preliminary and final data processing, including generation of final digital data and map products were undertaken from the office of Geotech Ltd. in Aurora, Ontario.

The processed survey results are presented as electromagnetic stacked profiles, and as a colour grid of the B-field EM late time channels and total magnetic intensity.

Digital data includes all electromagnetic and magnetic products, plus ancillary data including the waveform.

The survey report describes the procedures for data acquisition, processing, final image presentation and the specifications for the digital data set. No formal interpretation is included.

1. INTRODUCTION

1.1 General Considerations

These services are the result of the Agreement made between Geotech Ltd. and Archer Cathro & Associates Ltd. to perform a helicopter-borne geophysical survey one (1) block on the Caribou property located near Ross River, Yukon, Canada (Figure 1).

Matthew Dumala acted on behalf of Archer Cathro & Associates Ltd. during the data acquisition and data processing phases of this project.

The geophysical surveys consisted of helicopter borne EM using the versatile time-domain electromagnetic (VTEM) system and aeromagnetics using a caesium magnetometer. A total of 156 line-km of geophysical data were acquired during the survey. The survey area is shown in Figure 2.

The crew was based out of Ross River, Yukon for the acquisition phase of the survey. Survey flying started and was completed on July 30th, 2008

Data quality control and quality assurance, and preliminary data processing were carried out on a daily basis during the acquisition phase of the project. Final data processing followed immediately after the end of the survey. Final reporting, data presentation and archiving were completed from the Aurora office of Geotech Ltd. in November, 2008.



Figure 1 - Property Location

1.2 Survey Location and Specifications

The Caribou block (60°15'56.45"N, 132° 3'4.30"W) is located approximately 192 kilometres south of Ross River, Yukon, the base of operations for the survey.

The survey blocks were flown in a north-eastern (N 47° E) direction with a traverse line spacing of 100 metres, as depicted in Figure 2. Tie lines were flown perpendicular to the traverse lines at a spacing of 950 metres in the direction of N 137° E. For more detailed information on the flight spacing and direction see Table 1.

1.3 Topographic Relief and Cultural Features

Topographically, the property exhibits moderate relief, with elevations ranging from 1088 to 1450 metres above sea level (see Figure 2). There are a number of small rivers and streams that run throughout the block, as well as a small area of wetland. There are no roads leading to the block, making it accessible only by air. The survey block is covered by NTS (National Topographic Survey) of Canada sheets 105C01, 105C08, 105B04, 105B05.



Figure 2 - Google Earth Image with Flight Paths

2. DATA ACQUISITION

2.1 Survey Area

The survey blocks (see Location map, Figure 2) and general flight specifications are as follows:

Table 1 - Survey blocks

Survey block	Line spacing (m)	Area (Km^2)	Planned Line-km	Actual Line-km[1]	Flight direction	Line number
Caribou	Traverse: 100	15	138	151	N 47°E	L14000 - 14450
	Tie: 950		18	19	N 137°E	T14500 - 14530
TOTAL		15	156	170		

Survey block boundaries co-ordinates are provided in Appendix B.

2.2 Survey Operations

Survey operations were based out of Ross River Yukon on July 30th, 2008. The following table shows the timing of the flying.

Table 2 - Survey schedule

Date	Flight #	Flown km	Block	Crew location	Comments
30-July-08	65 - 68	292	MOR and CAR	Ross River, Yukon	Production

[1]NOTE: Actual line-km represents the total line-km contained in the final databases. These line-km normally exceed the Planned line-km, as indicated in the survey NAV files.

2.3 Flight Specifications

The helicopter was maintained at a mean height of 72 metres above the ground with a nominal survey speed of 80 km/hour. This allowed for a nominal EM sensor terrain clearance of 36 metres and a magnetic sensor clearance of 59 metres. The data recording rates of the data acquisition was 0.1 second for electromagnetics, magnetometer and 0.2 second for altimeter and GPS. This translates to a geophysical reading about every 2 metres along flight track. Navigation was assisted by a CDGPS receiver and data acquisition system, which reports GPS co-ordinates as latitude/longitude and directs the pilot over a pre-programmed survey grid.

The operator was responsible for monitoring of the system integrity. He also maintained a detailed flight log during the survey, tracking the times of the flight as well as any unusual geophysical or topographic feature.

On return of the aircrew to the base camp the survey data was transferred from a compact flash card (PCMCIA) to the data processing computer. The data were then uploaded via ftp to the Geotech office in Aurora for daily quality assurance and quality control by qualified personnel, operating remotely.

2.4 Aircraft and Equipment

2.4.1 Survey Aircraft

The survey was flown using a Eurocopter Aerospatiale (Astar) 350 B3 helicopter, registration C-GTRK. The helicopter was operated by TRK Helicopters Ltd. Installation of the geophysical and ancillary equipment was carried out by Geotech Ltd.

2.4.2 Electromagnetic System

The electromagnetic system was a Geotech Time Domain EM (VTEM) system. The configuration is as indicated in Figure 3 below.

Receiver and transmitter coils are concentric and Z-direction oriented. The coils were towed at a mean distance of 35 metres below the aircraft as shown in Figure 5. The receiver decay recording scheme is shown diagrammatically in Figure 4.

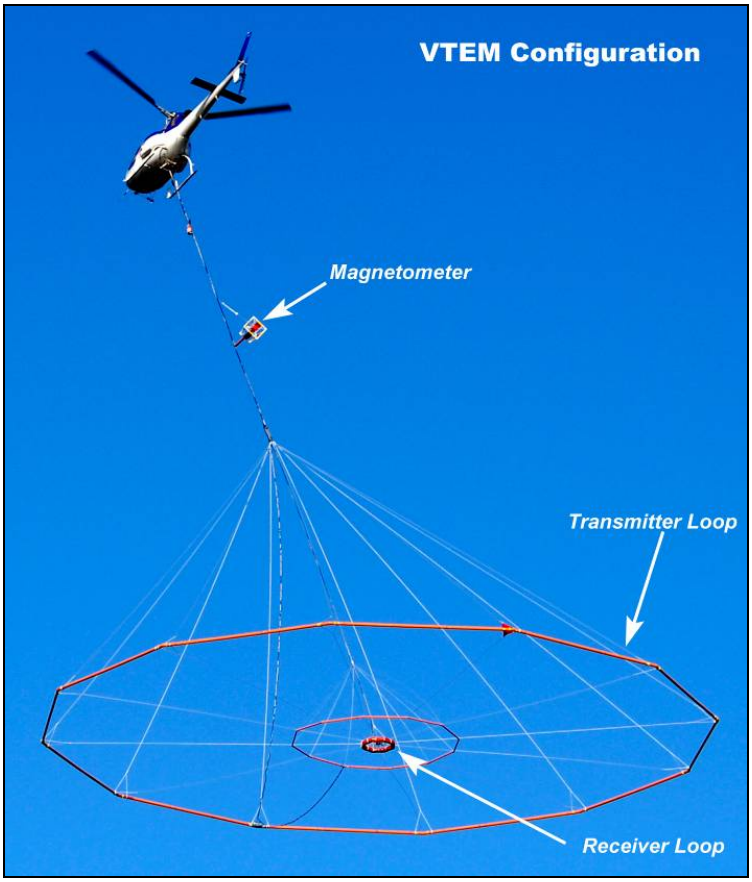


Figure 3 - VTEM Configuration

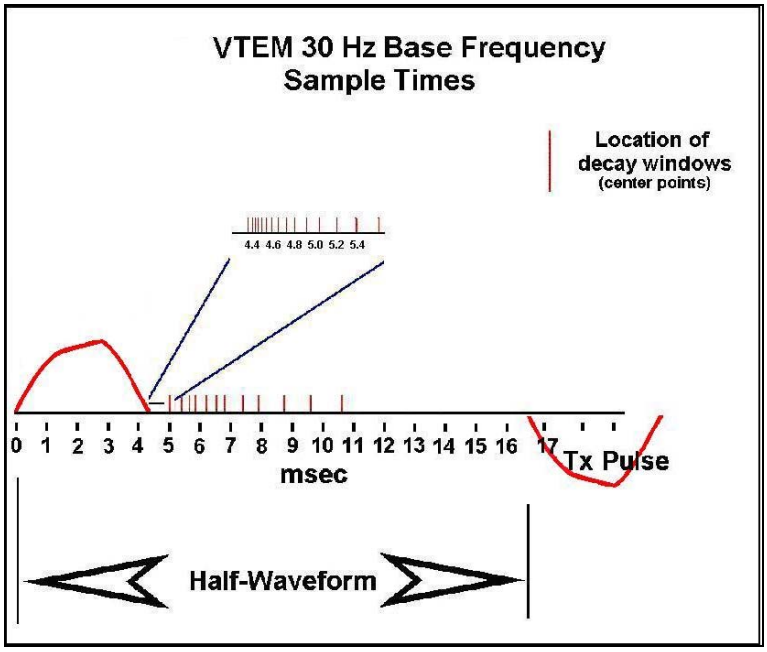


Figure 4 – VTEM Short Pulse Waveform & Sample Times

The VTEM decay sampling scheme is shown in Table 3 below. Twenty six measurement gates (ch 10-35) were used for the final data processing in the range from 120 ms to 9245ms, as shown in Table 5.

Table 3 – Decay Sampling Scheme

VTEM Decay Sampling scheme				
Array Index	(Microseconds)			
	Time Gate	Start	End	Width
0	0			
1	10	10	21	11
2	21	16	26	11
3	31	26	37	11
4	42	37	47	11
5	52	47	57	10
6	62	57	68	11
7	73	68	78	11
8	83	78	91	13
9	99	91	110	19
10	120	110	131	21
11	141	131	154	24
12	167	154	183	29
13	198	183	216	34
14	234	216	258	42
15	281	258	310	53
16	339	310	373	63
17	406	373	445	73
18	484	445	529	84
19	573	529	628	99
20	682	628	750	123
21	818	750	896	146
22	974	896	1063	167
23	1151	1063	1261	198
24	1370	1261	1506	245
25	1641	1506	1797	292
26	1953	1797	2130	333
27	2307	2130	2526	396
28	2745	2526	3016	490
29	3286	3016	3599	583
30	3911	3599	4266	667
31	4620	4266	5058	792
32	5495	5058	6037	979
33	6578	6037	7203	1167
34	7828	7203	8537	1334
35	9245	8537	10120	1584

VTEM system parameters:

Transmitter Section
- Transmitter coil diameter: 26 m
- Number of turns: 4
- Transmitter base frequency: 30 Hz
- Peak current: 179 A
- Pulse width: 4.2 ms
- Pulse width: Duty cycle: 44%
- Peak dipole moment: 556,400 nIA
- Nominal terrain clearance: 36 m

Receiver Section
- Receiver coil diameter: 1.2 m
- Number of turns: 100.
- Effective coil area: 113.1 m^2
- Wave form shape: trapezoid
- Power Line Monitor: 60 Hz

Magnetometer
- Nominal terrain clearance: 59 m

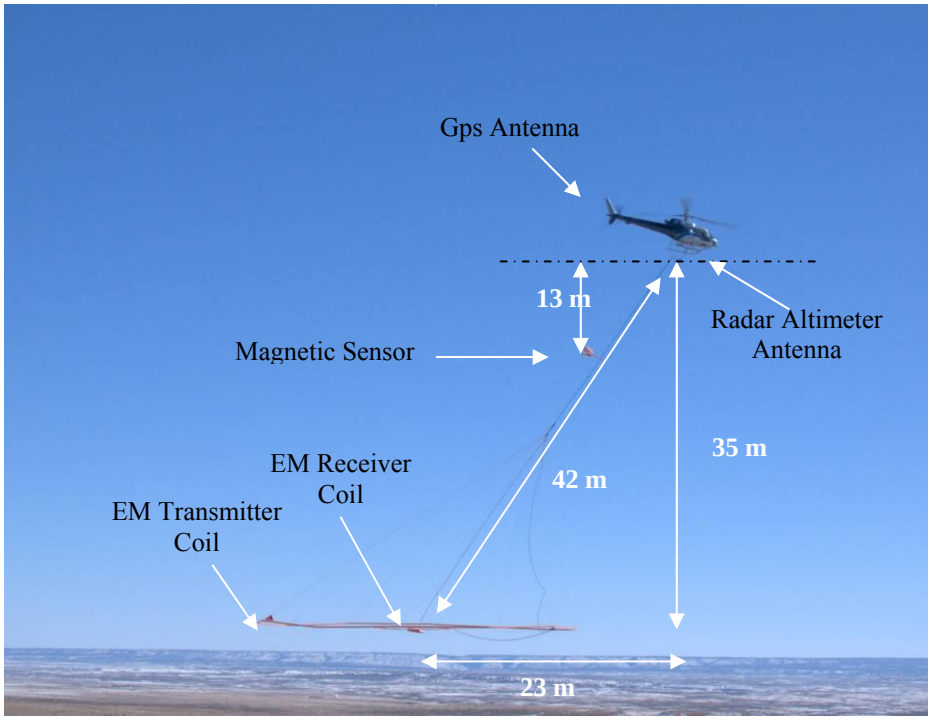


Figure 5 - VTEM system configuration

2.4.3 Airborne magnetometer

The magnetic sensor utilized for the survey was a Geometrics optically pumped caesium vapour magnetic field sensor, mounted in a separate bird, 13 metres below the helicopter, as shown in Figure 5. The sensitivity of the magnetic sensor is 0.02 nanoTesla (nT) at a sampling interval of 0.1 seconds. The magnetometer sends the measured magnetic field strength as nanoTesla to the data acquisition system via the RS-232 port.

2.4.4 Radar Altimeter

A Terra TRA 3000/TRI 40 radar altimeter was used to record terrain clearance. The antenna was mounted beneath the bubble of the helicopter cockpit (Figure 5).

2.4.5 GPS Navigation System

The navigation system used was a Geotech PC104 based navigation system utilizing a NovAtel's CDGPS (Canada-Wide Differential Global Positioning System Correction Service) enable OEM4-G2-3151W GPS receiver, Geotech navigate software, a full screen display with controls in front of the pilot to direct the flight and an NovAtel GPS antenna mounted on the helicopter tail (Figure 5). As many as 11 GPS and two CDGPS satellites may be monitored at any one time. The positional accuracy or circular error probability (CEP) is 1.8 m, with CDGPS active, it is 1.0 m. The co-ordinates of the block were set-up prior to the survey and the information was fed into the airborne navigation system.

2.4.6 Digital Acquisition System

A Geotech data acquisition system recorded the digital survey data on an internal compact flash card. Data is displayed on an LCD screen as traces to allow the operator to monitor the integrity of the system. The data type and sampling interval as provided in Table 4.

Table 4 – Acquisition Sampling Rates

DATA TYPE	SAMPLING
TDEM	0.1 sec
Magnetometer	0.1 sec
GPS Position	0.2 sec
Radar Altimeter	0.2 sec

2.4.7 Base Station

A combined magnetometer/GPS base station was utilized on this project. A Geometrics Caesium vapour magnetometer was used as a magnetic sensor with a sensitivity of 0.001 nT. The base station was recording the magnetic field together with the GPS time at 1 Hz on a base station computer.

The base station magnetometer sensor was installed south of the apron on a support at the airport in Ross River, Yukon (60°10'25.5"N, 132°43'68.5"W), away from electric transmission lines and moving ferrous objects such as motor vehicles. The base station data were backed-up to the data processing computer at the end of each survey day.

3. PERSONNEL

The following Geotech Ltd. personnel were involved in the project.

Field:

Project Manager:	Les Moschuk (office)
Data QC/QA:	Nick Venter (office)
Crew chief:	Ryan MacIver
System Operator:	Jason McKinnon

The survey pilot and the mechanical engineer were employed directly by the helicopter operator – TRK Helicopters Ltd.

Pilot:	Randy Marks
Mechanical Engineer:	Chris Ward

Office:

Preliminary Data Processing:	Nick Venter
Final Data Processing:	Neil Fiset
Mapping/Reporting:	Kyle Orlowski

Data acquisition phase was carried out under the supervision of Andrei Bagrianski, P. Geo, Surveys Manager. Processing phase was carried out under the supervision of Jean Legault, P. Geo, Manager of Processing and Interpretation. The overall contract management and customer relations were by Paolo Berardelli.

4. DATA PROCESSING AND PRESENTATION

Data compilation and processing were carried out by the application of Geosoft OASIS Montaj and programs proprietary to Geotech Ltd.

4.1 Flight Path

The flight path, recorded by the acquisition program as WGS 84 latitude/longitude, was converted into the NAD83 Datum, UTM Zone 8 North coordinate system in Oasis Montaj.

The flight path was drawn using linear interpolation between x, y positions from the navigation system. Positions are updated every second and expressed as UTM easting's (x) and UTM northing's (y).

4.2 Electromagnetic Data

A three stage digital filtering process was used to reject major sferic events and to reduce system noise. Local sferic activity can produce sharp, large amplitude events that cannot be removed by conventional filtering procedures. Smoothing or stacking will reduce their amplitude but leave a broader residual response that can be confused with geological phenomena. To avoid this possibility, a computer algorithm searches out and rejects the major sferic events. The filter used was a 16 point non-linear filter.

The signal to noise ratio was further improved by the application of a low pass linear digital filter. This filter has zero phase shift which prevents any lag or peak displacement from occurring, and it suppresses only variations with a wavelength less than about 1 second or 15 metres. This filter is a symmetrical 1 sec linear filter.

The results are presented as stacked profiles of EM voltages for the time gates, in linear - logarithmic scale for both B-field and dB/dt response. B-field time channel recorded at 1.641 milliseconds after the termination of the impulse is also presented as contour colour image.

Graphical representations of the VTEM transmitter current waveform output voltage of the receiver coil are shown in Appendix C.

Generalized modeling results of VTEM data, written by consultant Roger Barlow and Nasreddine Bournas, P. Geo., are shown in Appendix E.

4.3 Magnetic Data

The processing of the magnetic data involved the correction for diurnal variations by using the digitally recorded ground base station magnetic values. The base station magnetometer data was edited and merged into the Geosoft GDB database on a daily basis. The aeromagnetic data was corrected for diurnal variations by subtracting the observed magnetic base station deviations.

Tie line levelling was carried out by adjusting intersection points along traverse lines. A micro-levelling procedure was applied to remove persistent low-amplitude components of flight-line noise remaining in the data.

The corrected magnetic data was interpolated between survey lines using a random point gridding method to yield x-y grid values for a standard grid cell size of approximately 0.2 cm at the mapping scale. The Minimum Curvature algorithm was used to interpolate values onto a rectangular regular spaced grid.

5. DELIVERABLES

5.1 Survey Report

The survey report describes the data acquisition, processing, and final presentation of the survey results.

The survey report is provided in two paper copies and digitally in PDF format.

5.2 Maps

Final maps were produced at scale of 1:10,000. The coordinate/projection system used was NAD 83, UTM Zone 8 North. All maps show the flight path trace and topographic data; latitude and longitude are also noted on maps.

The preliminary and final results of the survey are presented as EM profiles, a late-time gate gridded EM channel, and color magnetic TMI contour maps. The following maps are presented on paper;

- VTEM B-field profiles, Time Gates 0.234 – 9.245 ms in linear - logarithmic scale over total magnetic intensity colour grid and.
- VTEM dB/dt profiles, Time Gates 0.234 – 9.245 ms in linear – logarithmic scale.
- VTEM B-field late time, Time Gate 1.641 ms colour image.
- Total magnetic intensity (TMI) colour image and contours.

.

5.3 Digital Data

- Two copies of the data and maps on DVD were prepared to accompany the report. Each DVD contains a digital file of the line data in GDB Geosoft Montaj format as well as the maps in Geosoft Montaj Map and PDF format.

- DVD structure.

  There are two (2) main directories;

  Data contains databases, grids and maps, as described below.
  Report contains a copy of the report and appendices in PDF format.

  Databases in Geosoft GDB format, containing the channels listed in Table 5.

Table 5 – Geosoft GDB Data Format.

Channel Name	Description
X:	X positional data (metres – NAD83, UTM zone 8 north)
Y:	Y positional data (metres – NAD83, UTM zone 8 north)
Z:	GPS antenna elevation (metres - ASL)
Lon:	Longitude data (degree – WGS84)
Lat:	Latitude data (degree – WGS84)
Date:	Flight Date (DD/MM/YYYY)
FltNo	Flight Number
Radar:	Helicopter terrain clearance from radar altimeter (metres - AGL)
RadarB:	EM Bird terrain clearance from radar altimeter (metres - AGL)
DEM:	Digital elevation model (metres)
Gtime:	GPS time (seconds of the day)
Mag1:	Raw Total Magnetic field data (nT)
Basemag:	Magnetic diurnal variation data (nT)
Mag2	Total Magnetic field diurnal variation corrected data (nT)
Mag3	Total Magnetic field final microlevelled data (nT)
SF[10]:	dB/dt 120 microsecond time channel pV/(A*m^4)
SF[11]:	dB/dt 141 microsecond time channel pV/(A*m^4)
SF[12]:	dB/dt 167 microsecond time channel pV/(A*m^4)
SF[13]:	dB/dt 198 microsecond time channel pV/(A*m^4)
SF[14]:	dB/dt 234 microsecond time channel pV/(A*m^4)
SF[15]:	dB/dt 281 microsecond time channel pV/(A*m^4)
SF[16]:	dB/dt 339 microsecond time channel pV/(A*m^4)
SF[17]:	dB/dt 406 microsecond time channel pV/(A*m^4)
SF[18]:	dB/dt 484 microsecond time channel pV/(A*m^4)
SF[19]:	dB/dt 573 microsecond time channel pV/(A*m^4)
SF[20]:	dB/dt 682 microsecond time channel pV/(A*m^4)
SF[21]:	dB/dt 818 microsecond time channel pV/(A*m^4)
SF[22]:	dB/dt 974 microsecond time channel pV/(A*m^4)
SF[23]:	dB/dt 1151 microsecond time channel pV/(A*m^4)
SF[24]:	dB/dt 1370 microsecond time channel pV/(A*m^4)
SF[25]:	dB/dt 1641 microsecond time channel pV/(A*m^4)
SF[26]:	dB/dt 1953 microsecond time channel pV/(A*m^4)
SF[27]:	dB/dt 2307 microsecond time channel pV/(A*m^4)
SF[28]:	dB/dt 2745 microsecond time channel pV/(A*m^4)
SF[29]:	dB/dt 3286 microsecond time channel pV/(A*m^4)
SF[30]:	dB/dt 3911 microsecond time channel pV/(A*m^4)
SF[31]:	dB/dt 4620 microsecond time channel pV/(A*m^4)

Channel Name	Description
SF[32]:	dB/dt 5495 microsecond time channel pV/(A*m^4)
SF[33]:	dB/dt 6578 microsecond time channel pV/(A*m^4)
SF[34]:	dB/dt 7828 microsecond time channel pV/(A*m^4)
SF[35]:	dB/dt 9245 microsecond time channel pV/(A*m^4)
BF[10]:	B-field 120 microsecond time channel (pV*ms)/(A*m^4)
BF[11]:	B-field 141 microsecond time channel (pV*ms)/(A*m^4)
BF[12]:	B-field 167 microsecond time channel (pV*ms)/(A*m^4)
BF[13]:	B-field 198 microsecond time channel (pV*ms)/(A*m^4)
BF[14]:	B-field 234 microsecond time channel (pV*ms)/(A*m^4)
BF[15]:	B-field 281 microsecond time channel (pV*ms)/(A*m^4)
BF[16]:	B-field 339 microsecond time channel (pV*ms)/(A*m^4)
BF[17]:	B-field 406 microsecond time channel (pV*ms)/(A*m^4)
BF[18]:	B-field 484 microsecond time channel (pV*ms)/(A*m^4)
BF[19]:	B-field 573 microsecond time channel (pV*ms)/(A*m^4)
BF[20]:	B-field 682 microsecond time channel (pV*ms)/(A*m^4)
BF[21]:	B-field 818 microsecond time channel (pV*ms)/(A*m^4)
BF[22]:	B-field 974 microsecond time channel (pV*ms)/(A*m^4)
BF[23]:	B-field 1151 microsecond time channel (pV*ms)/(A*m^4)
BF[24]:	B-field 1370 microsecond time channel (pV*ms)/(A*m^4)
BF[25]:	B-field 1641 microsecond time channel (pV*ms)/(A*m^4)
BF[26]:	B-field 1953 microsecond time channel (pV*ms)/(A*m^4)
BF[27]:	B-field 2307 microsecond time channel (pV*ms)/(A*m^4)
BF[28]:	B-field 2745 microsecond time channel (pV*ms)/(A*m^4)
BF[29]:	B-field 3286 microsecond time channel (pV*ms)/(A*m^4)
BF[30]:	B-field 3911 microsecond time channel (pV*ms)/(A*m^4)
BF[31]:	B-field 4620 microsecond time channel (pV*ms)/(A*m^4)
BF[32]:	B-field 5495 microsecond time channel (pV*ms)/(A*m^4)
BF[33]:	B-field 6578 microsecond time channel (pV*ms)/(A*m^4)
BF[34]:	B-field 7828 microsecond time channel (pV*ms)/(A*m^4)
BF[35]:	B-field 9245 microsecond time channel (pV*ms)/(A*m^4)
PLM:	Power Line monitor (60Hz)
Distance:	Distance between observations (metres)

Electromagnetic B-field and dB/dt data is found in array channel format between indexes 10 – 35, as described above.

- Database of the VTEM Waveform "VTEM_waveform.gdb" in Geosoft GDB format, containing the following channels:

  Time: Sampling rate interval, 10.416 microseconds
  Rx_Volt: Output voltage of the receiver coil (Volt)
  Tx_Curr: Output current of the transmitter (Amp)

- Grids in Geosoft GRD format, as follows:

  BF25_Car: B-Field Channel 25 (Time Gate 1.641 ms)
  Mag3_Car: Total magnetic intensity (nT)

  A Geosoft .GRD file has a .GI metadata file associated with it, containing grid projection information. A grid cell size of 25 metres was used.

- Maps at 1:10,000 in Geosoft MAP format, as follows:

  8077_Bfield_Car: B-field profiles, Time Gates 0.234 – 9.245 ms in linear logarithmic scale over TMI.
  8077_dBdt_Car: dB/dt profiles, Time Gates 0.234 – 9.245 ms in linear logarithmic scale.
  8077_BF_Car: B-field Time Gate 1.641 ms colour image.
  8077_TMI_Car: Total magnetic intensity colour image and contours.

  Maps are also presented in PDF and MapInfo format.

  1:50,000 topographic vectors were taken from the NRCAN Geogratis database at; http://geogratis.gc.ca/geogratis/en/index.html.

- Google Earth files *8077_Caribou_fltpath.kml* showing the flight path of each block. Free versions of Google Earth software from: http://earth.google.com/download-earth.html

6. CONCLUSIONS AND RECOMMENDATIONS

6.1 Conclusions

A helicopter-borne versatile time domain electromagnetic (VTEM) geophysical survey has been completed over the Caribou Project in the Yukon Territory, Canada.

The total area coverage is 15 km^2. Total survey line coverage is 156 line kilometres. The principal sensors included a Time Domain EM system and a magnetometer. Results have been presented as stacked profiles and contour colour images at a scale of 1:10,000. No formal interpretation is included in this report.

6.2 Recommendations

Based on the geophysical results obtained, a number of interesting EM and magnetic anomaly groupings were identified across the property. We therefore recommend a detailed interpretation of the EM and magnetic data, in conjunction with the known geology, including EM anomaly picking, as well as 3D inversion and modelling techniques to further characterize the observed anomalies and to more accurately determine their parameters (depth, conductance, dip, etc.) prior to ground follow up and drill testing.

Respectfully submitted[6],

Kyle Orlowski
Geotech Ltd.

Jean Legault, P. Geo, P. Eng
Geotech Ltd.

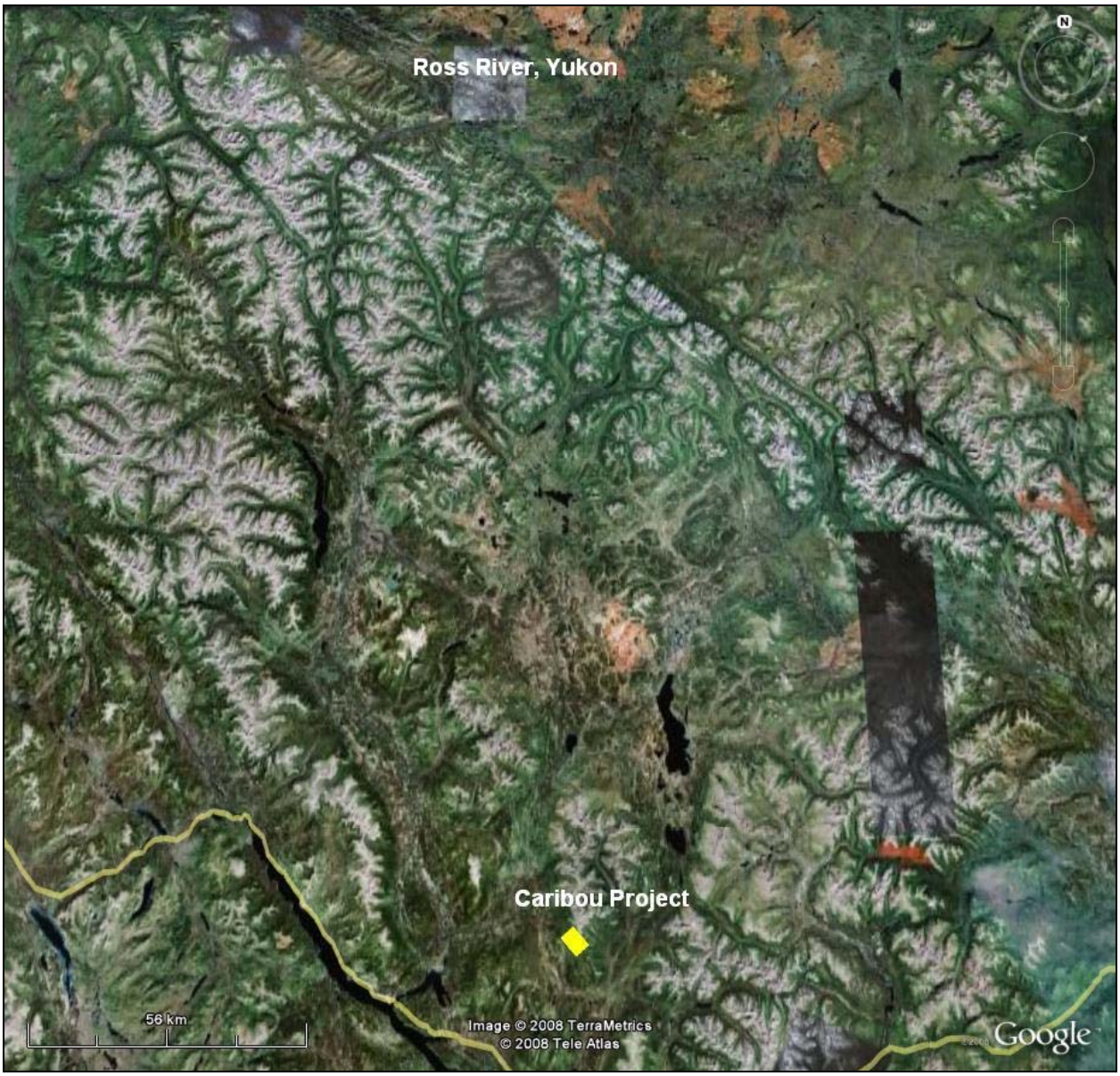
Neil Fiset
Geotech Ltd.

November 2008

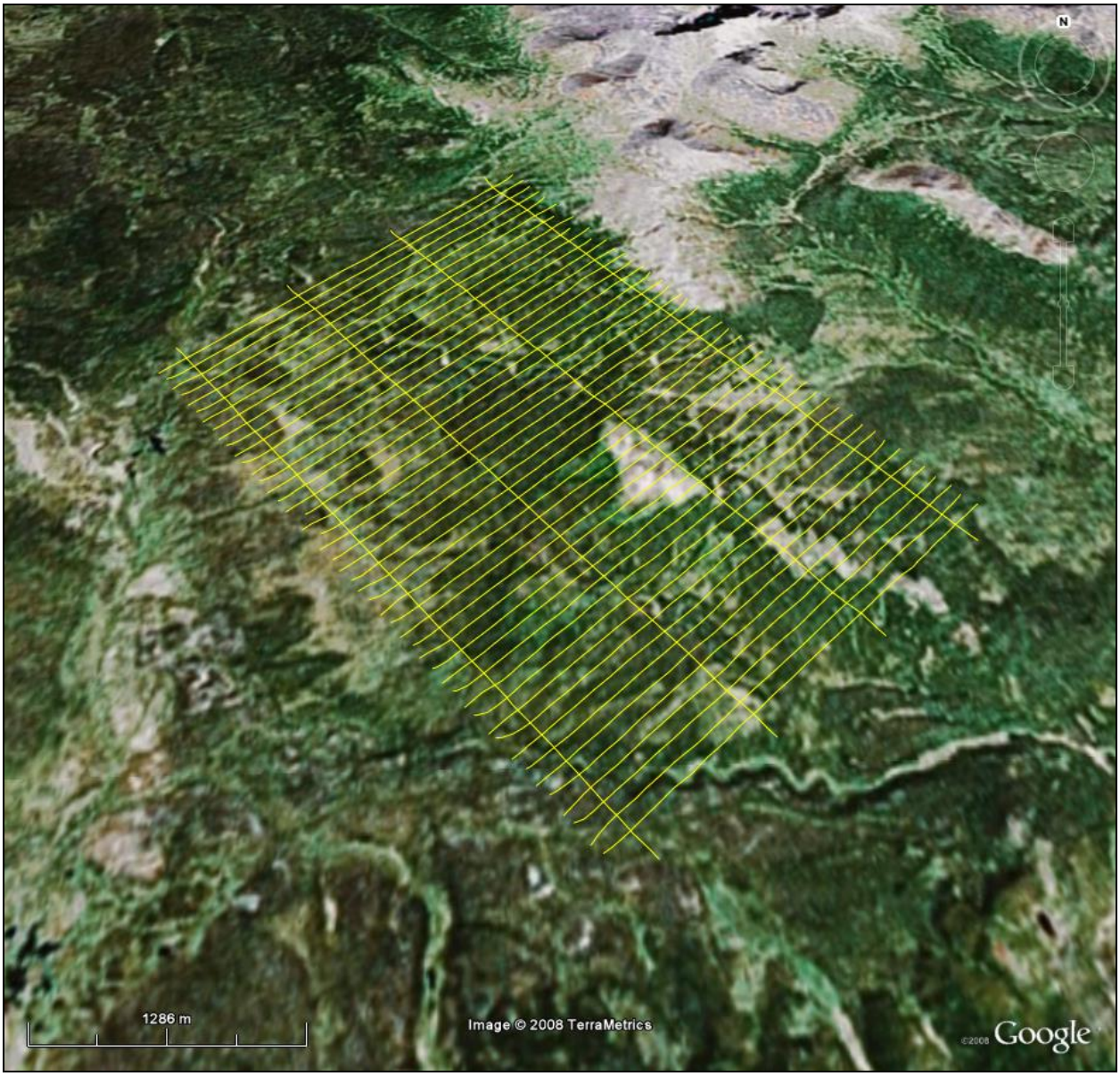
[6]Final data processing and interpretation of the EM and magnetic data were carried out by Neil Fiset, from the office of Geotech Ltd. in Aurora, Ontario, under the supervision of Jean Legault, P. Geo, Manager of Data Processing and Interpretation.

APPENDIX A

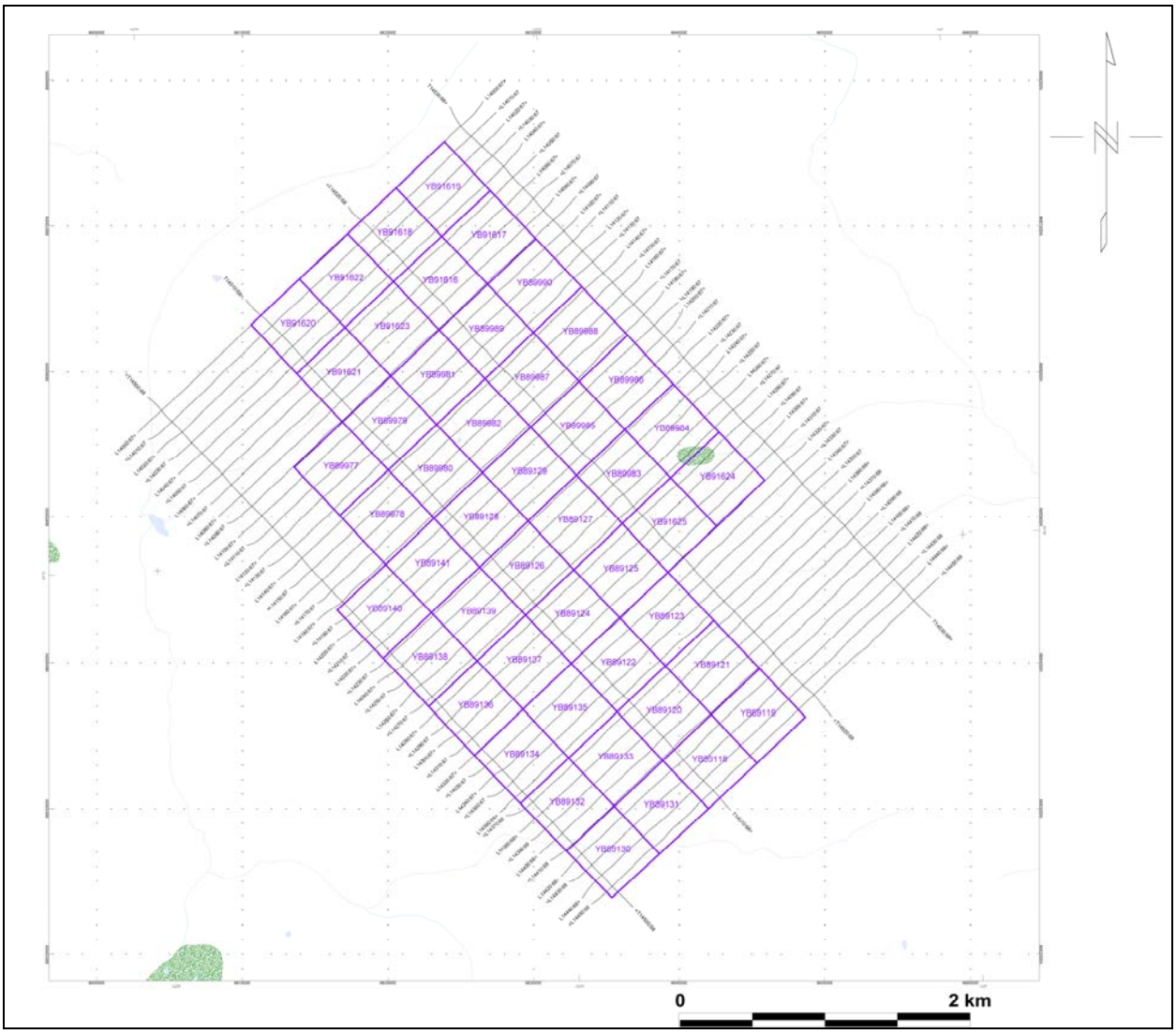
SURVEY BLOCK LOCATION MAPS



Google Earth Image: Caribou Project



Google Earth Image: Caribou Block



Mining Claims Map: Caribou Block

APPENDIX B

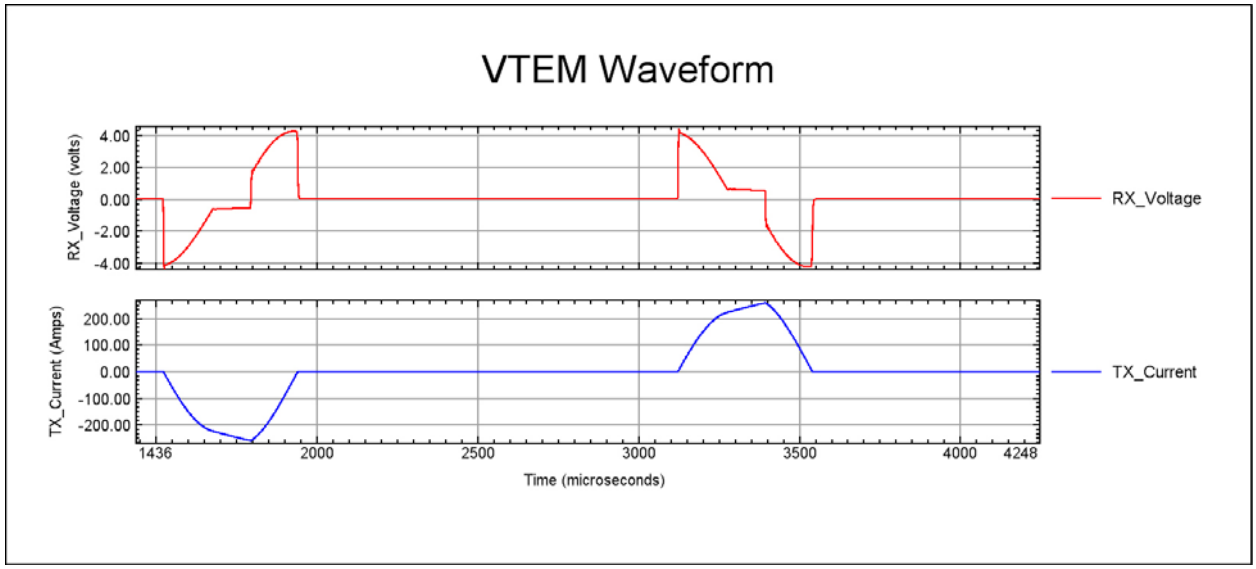
SURVEY BLOCK COORDINATES

(NAD83, UTM Zone 8 North)

Caribou	
X	Y
660389	6685687
662568	6687749
665700	6684464
663536	6682385

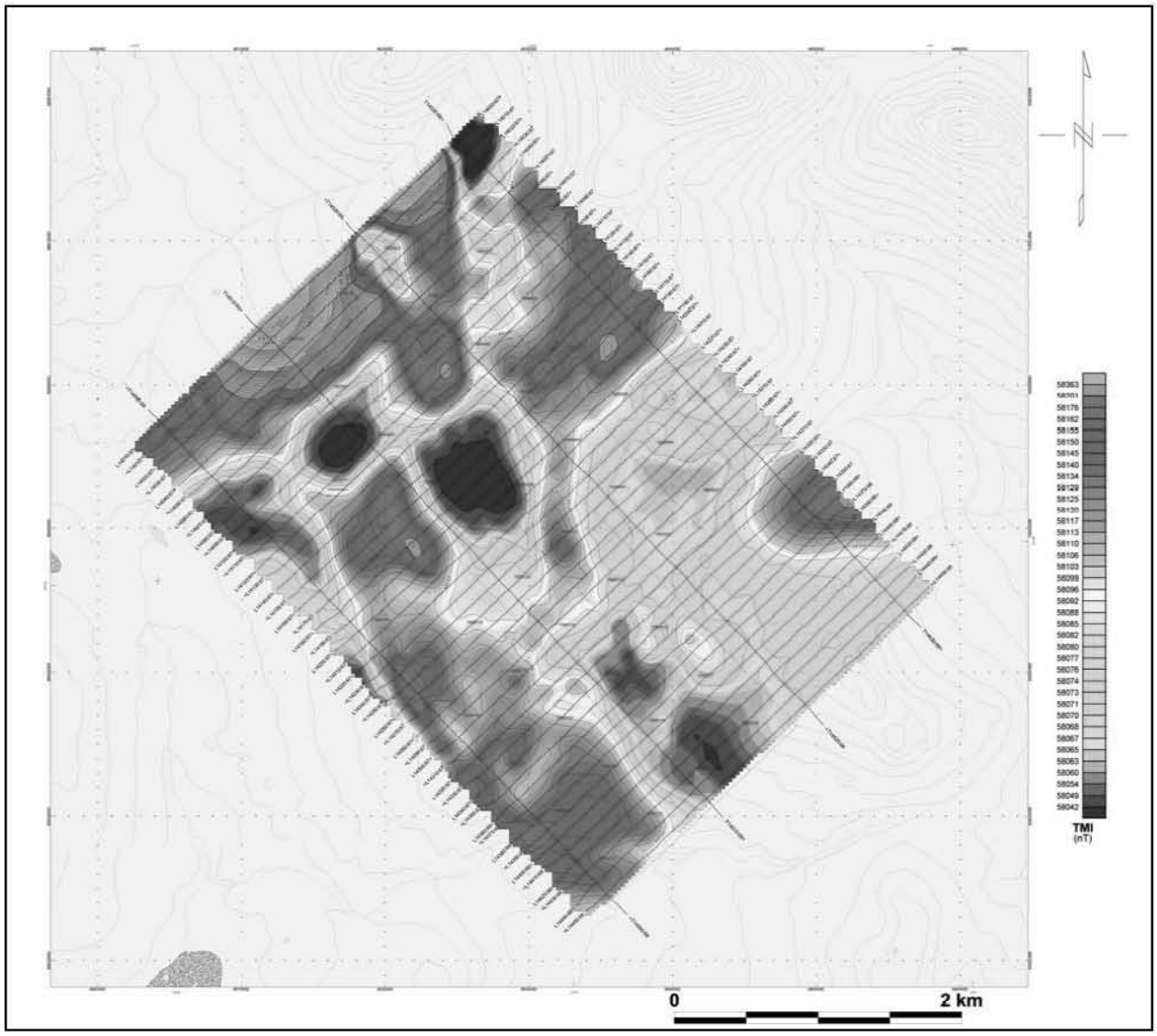
APPENDIX C

VTEM WAVEFORM



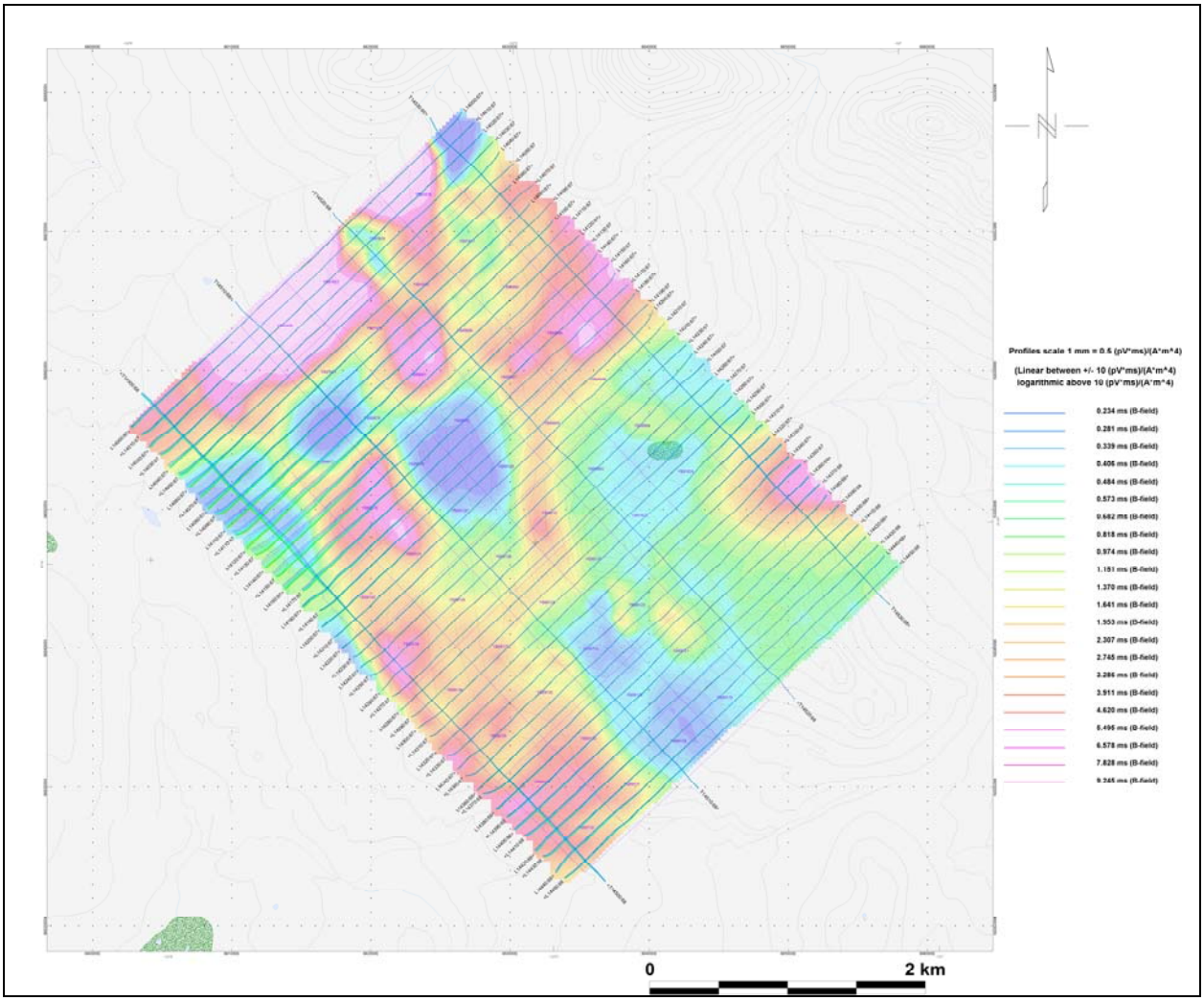
APPENDIX D

GEOPHYSICAL MAPS[1]

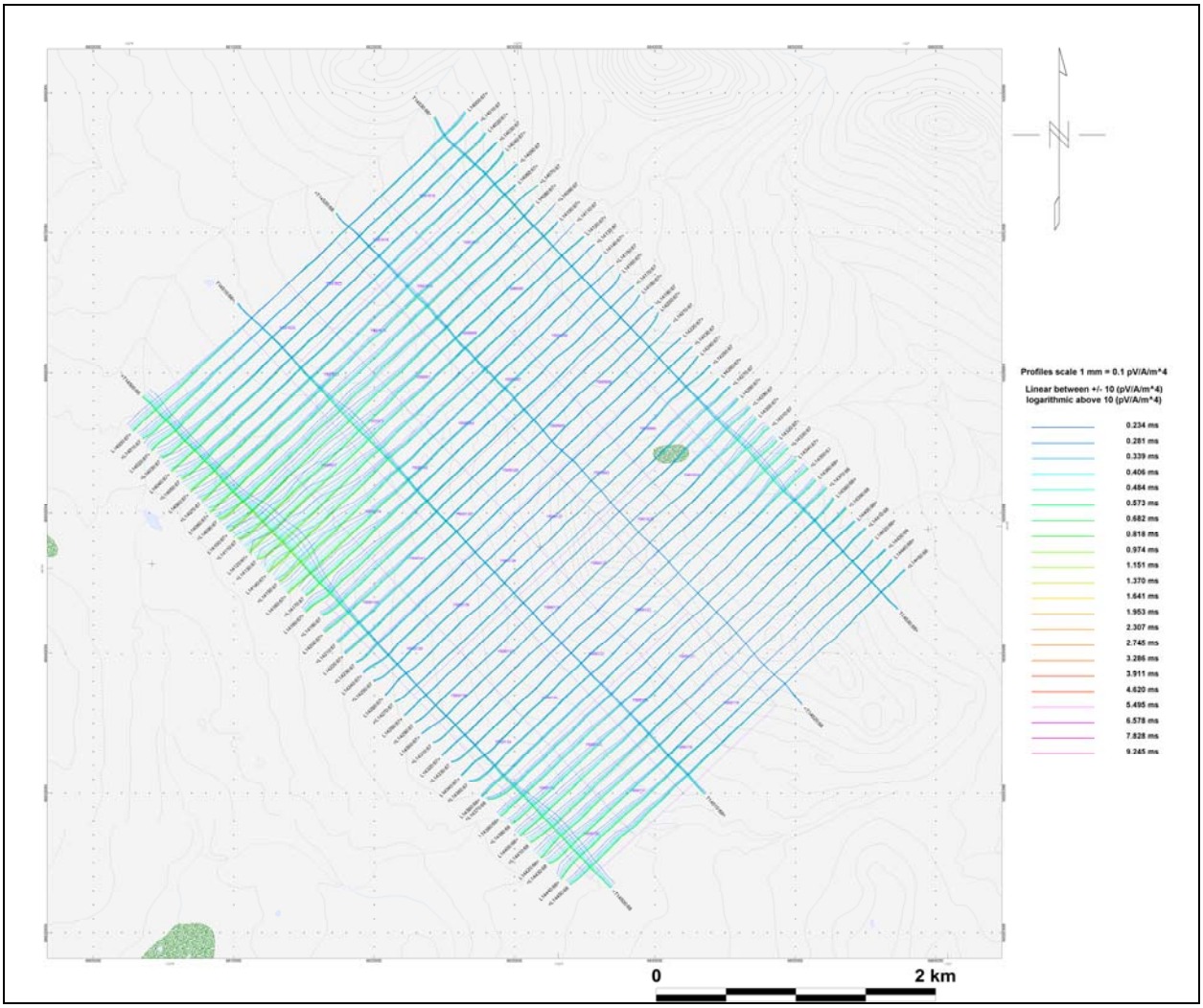


Caribou Property: Total Magnetic Intensity (TMI)

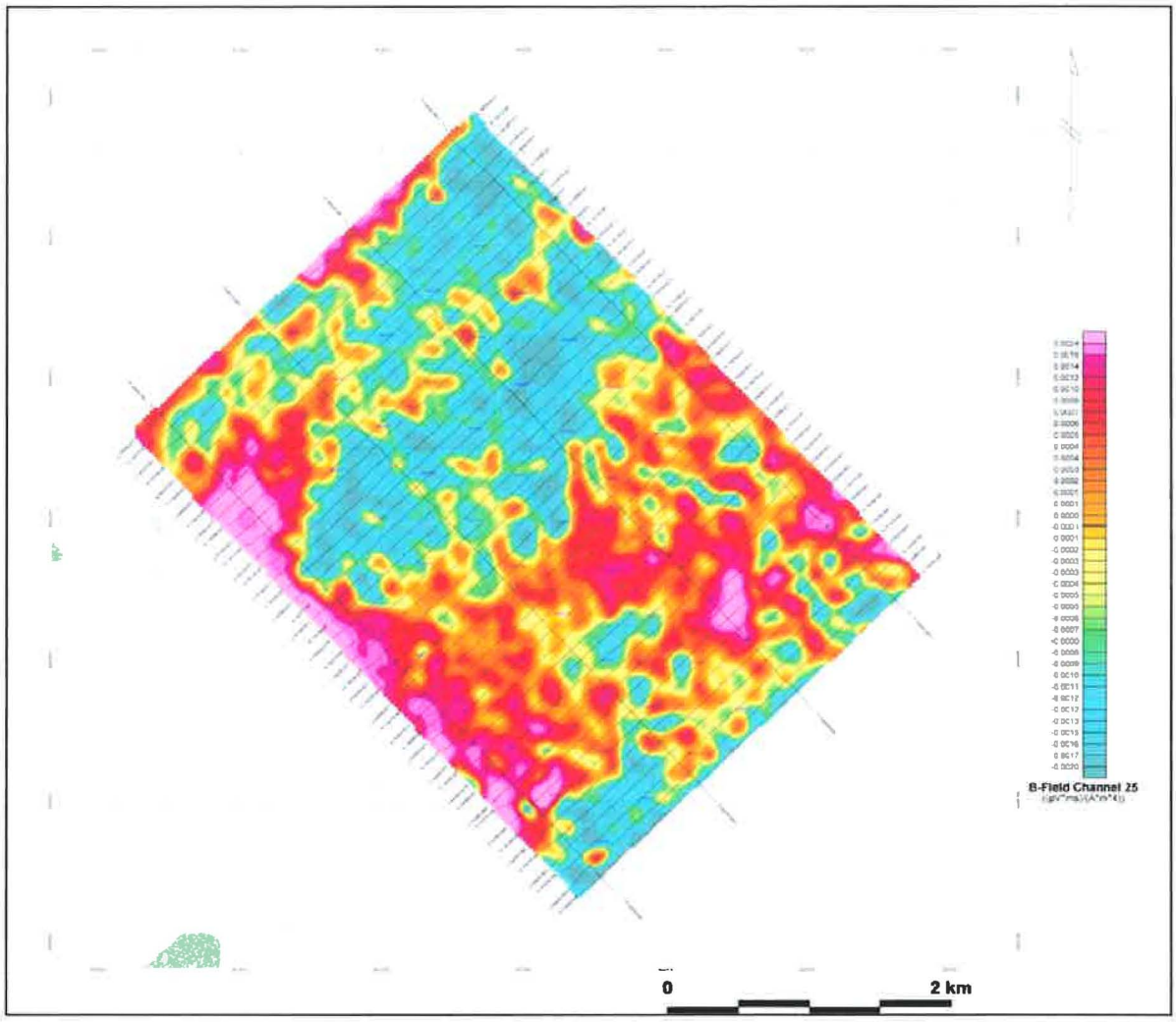
1 Note: Present maps are a selection of the final geophysical maps. Full size geophysical maps are also available in PDF format on the final DVD.



Caribou Property: VTEM B-Field Profiles – Time Gates 0.234 to 9.245 ms, over TMI



Caribou Property: VTEM dB/dt Profiles
- Time Gates 0.234 to 9.245 ms



Caribou Property: VTEM B-Field Contours
- Time Gate 1.641 ms

APPENDIX E

GENERALIZED MODELING RESULTS OF THE VTEM SYSTEM

Introduction

The VTEM system is based on a concentric or central loop design, whereby, the receiver is positioned at the centre of a 26.1 metres diameter transmitter loop that produces a dipole moment up to 384,000 nIA at peak current. The wave form is a bi-polar, modified square wave with a turn-on and turn-off at each end. With a base frequency of 30 Hz, the duration of each pulse is approximately 7.4 milliseconds followed by an off time where no primary field is present.

During turn-on and turn-off, a time varying field is produced (dB/dt) and an electro-motive force (emf) is created as a finite impulse response. A current ring around the transmitter loop moves outward and downward as time progresses. When conductive rocks and mineralization are encountered, a secondary field is created by mutual induction and measured by the receiver at the centre of the transmitter loop.

Measurements are made during the on and off-time, when only the secondary field (representing the conductive targets encountered in the ground) is present.

Efficient modeling of the results can be carried out on regularly shaped geometries, thus yielding close approximations to the parameters of the measured targets. The following is a description of a series of common models made for the purpose of promoting a general understanding of the measured results.

General Modeling Concepts

A set of models has been produced for the Geotech VTEM® system with explanation notes (see models C1 to C18). The reader is encouraged to review these models, so as to get a general understanding of the responses as they apply to survey results. While these models do not begin to cover all possibilities, they give a general perspective on the simple and most commonly encountered anomalies.

When producing these models, a few key points were observed and are worth noting as follows:

- For near vertical and vertical plate models, the top of the conductor is always located directly under the centre low point between the two shoulders in the classic **M** shaped response.

- As the plate is positioned at an increasing depth to the top, the shoulders of the **M** shaped response, have a greater separation distance.

- When faced with choosing between a flat lying plate and a prism model to represent the target (broad response) some ambiguity is present and caution should be exercised.

- With the concentric loop system and Z-component receiver coil, virtually all types of conductors and most geometries are most always well coupled and a response is generated (see model H). Only concentric loop systems can map this type of target.

The Maxwell ™ modeling program (Fullagar and Reid, 2001) used to generate the following responses assumes a resistive half-space.

Variation of Plate Depth

Geometries represented by plates of different strike length, depth extent, dip, plunge and depth below surface can be varied with characteristic parameters like conductance of the target, conductance of the host and conductivity/thickness and thickness of the overburden layer.

Diagrammatic models for a vertical plate are shown in Figures C-1 & C-2 and C-5 & C-6 at two different depths, all other parameters remaining constant. With this transmitter-receiver geometry, the classic **M** shaped response is generated. Figures C-1 and C-2 show a plate where the top is near surface. Here, amplitudes of the duel peaks are higher and symmetrical with the zero centre positioned directly above the plate. Most important is the separation distance of the peaks. This distance is small when the plate is near surface and widens with a linear relationship as the plate (depth to top) increases. Figures C-5 and C-6 show a much deeper plate where the separation distance of the peaks is much wider and the amplitudes of the channels have decreased.

Variation of Plate Dip

As the plate dips and departs from the vertical position, the peaks become asymmetrical. Figures C-3 & C-4 and C-7 and C-8 show a near surface plate dipping 80º at two different depths. Note that the direction of dip is toward the high shoulder of the response and the top of the plate remains under the centre minimum.

As the dip increases, the aspect ratio (Min/Max) decreases and this aspect ratio can be used as an empirical guide to dip angles from near 90º to about 30º. The method is not sensitive enough where dips are less than about 30º. For example, for a plate dipping 45º, the minimum shoulder

starts to vanish. In Figures C-9 & C-10 and C-11 & C-12, a flat lying plate is shown, relatively near surface. Note that the twin peak anomaly has been replaced by a symmetrical shape with large, bell shaped, channel amplitudes which decay relative to the conductance of the plate.

In the special case where two plates are positioned to represent a synclinal structure. Note that the main characteristic is that the centre amplitudes are higher (approximately double) compared to the high shoulder of a single plate. This model is very representative of tightly folded formations where the conductors where once flat lying.

Variation of Prism Dip

Finally, with thicker, prism models, another algorithm is required to represent current on the plate. A plate model is considered to be infinitely thin with respect to thickness and incapable of representing the current in the thickness dimension. A prism model is constructed to deal with this problem, thereby, representing the thickness of the body more accurately.

Figures C-13 & C-14 and C-15 & C-16 show the same prism at the same depths with variable dips. Aside from the expected differences asymmetry prism anomalies show a characteristic change from a double-peaked anomaly to single peak signatures.

I. THIN PLATE

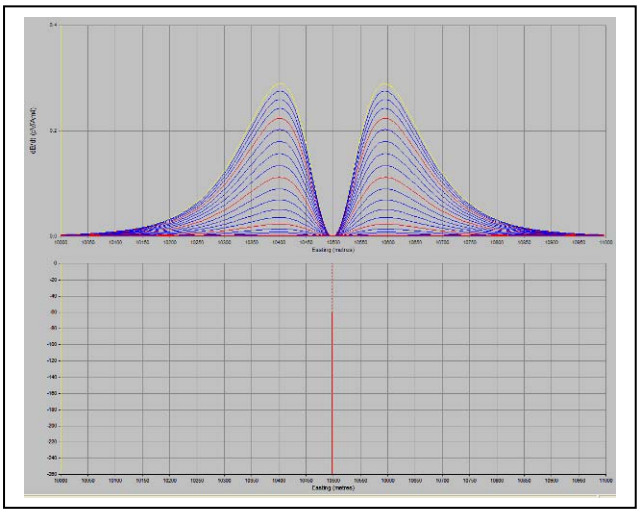


Figure C-1: dB/dt response of a shallow vertical thin plate. Depth=100 m, CT=20 S. The EM response is normalized by the dipole moment and the Rx area.

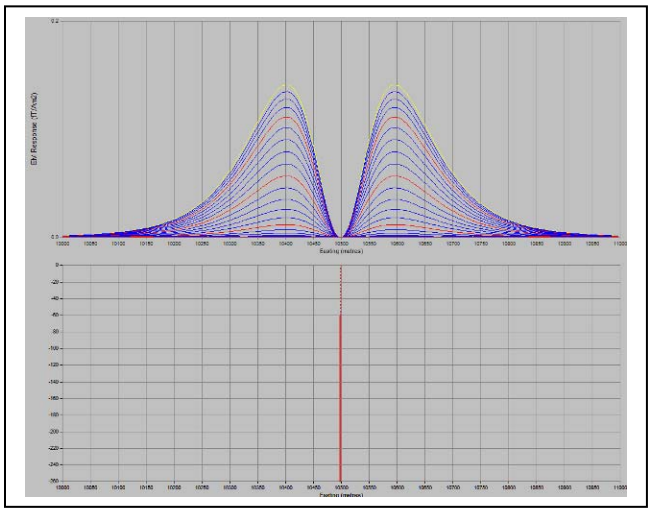


Figure C-2: B-field response of a shallow vertical thin plate. Depth=100 m, CT=20 S. The EM response is normalized by the dipole moment.

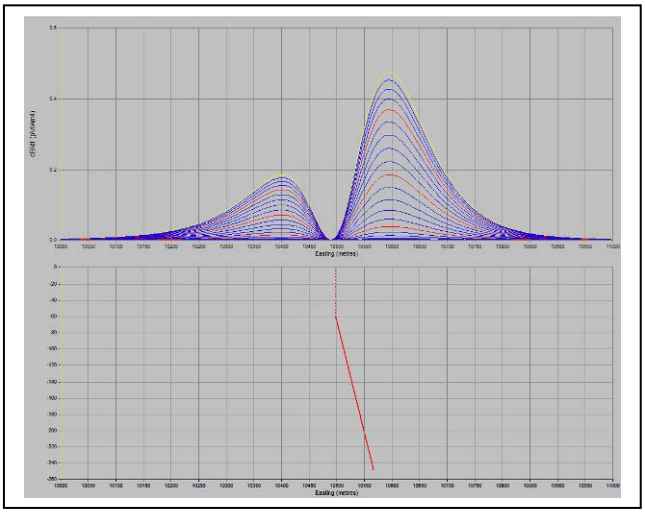


Figure C-3: dB/dt response of a shallow skewed thin plate. Depth=100 m, CT=20 S. The EM response is normalized by the dipole moment and the Rx area.

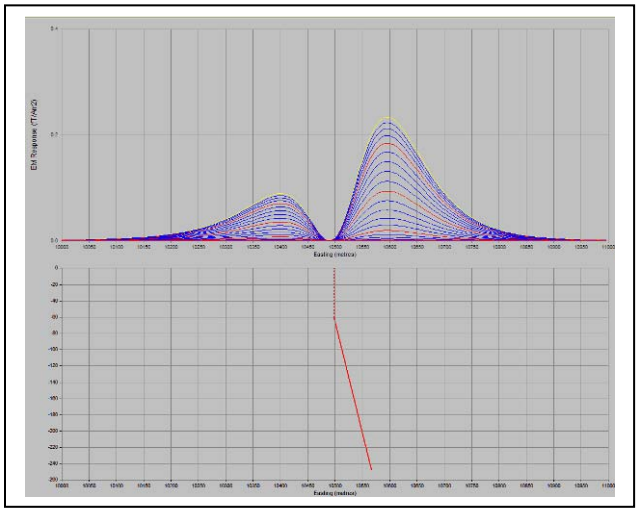


Figure C-4: B-field response of a shallow skewed thin plate. Depth=100 m, CT=20 S. The EM response is normalized by the dipole moment.

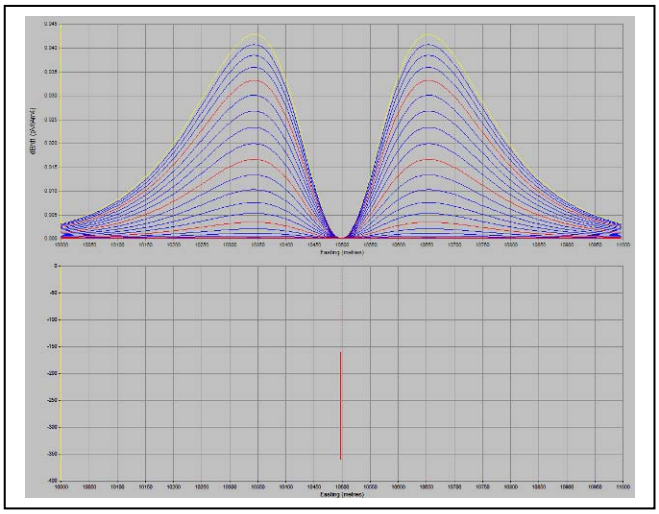


Figure C-5: dB/dt response of a deep vertical thin plate. Depth=200 m, CT=20 S. The EM response is normalized by the dipole moment and the Rx area.

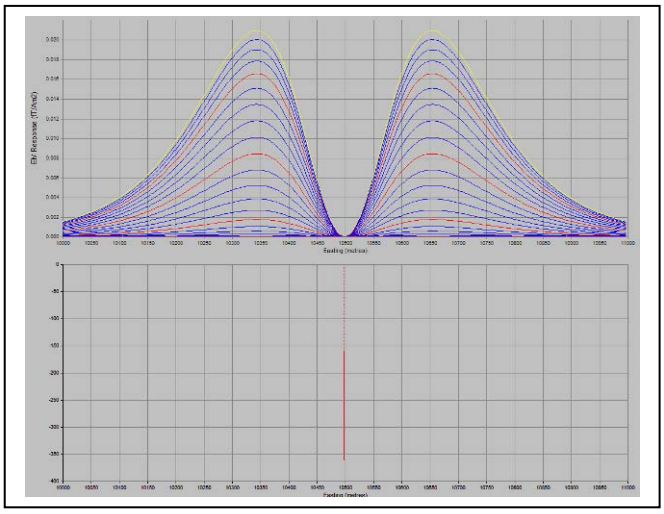


Figure C-6: B-Field response of a deep vertical thin plate. Depth=200 m, CT=20 S. The EM response is normalized by the dipole moment.

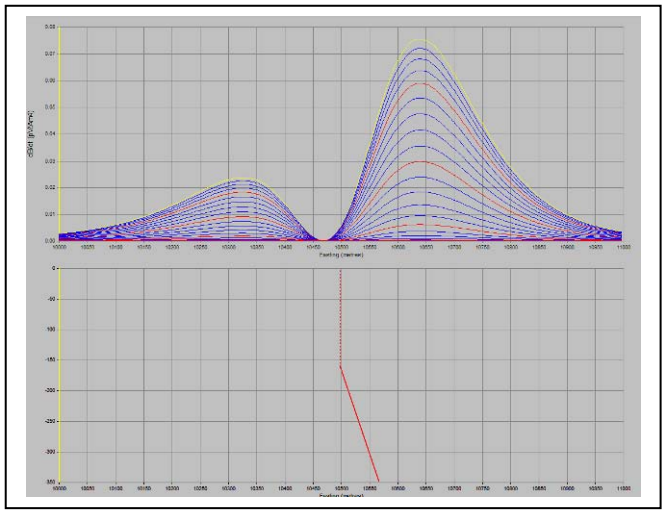


Figure C-7: dB/dt response of a deep skewed thin plate. Depth=200 m, CT=20 S. The EM response is normalized by the dipole moment and the Rx area.

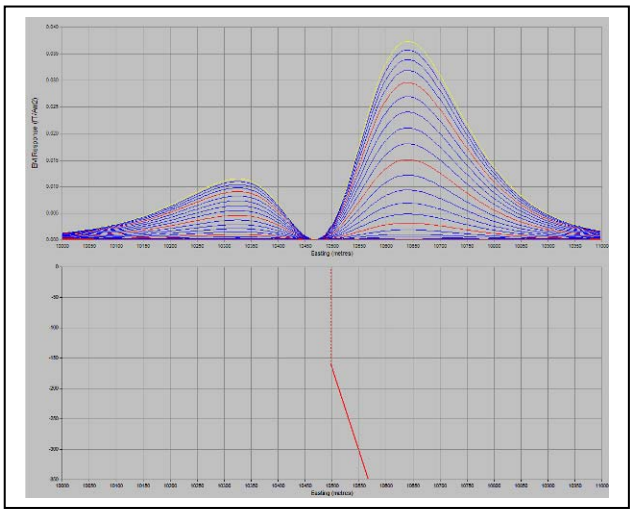


Figure C-8: B-field response of a deep skewed thin plate. Depth=200 m, CT=20 S. The EM response is normalized by the dipole moment.

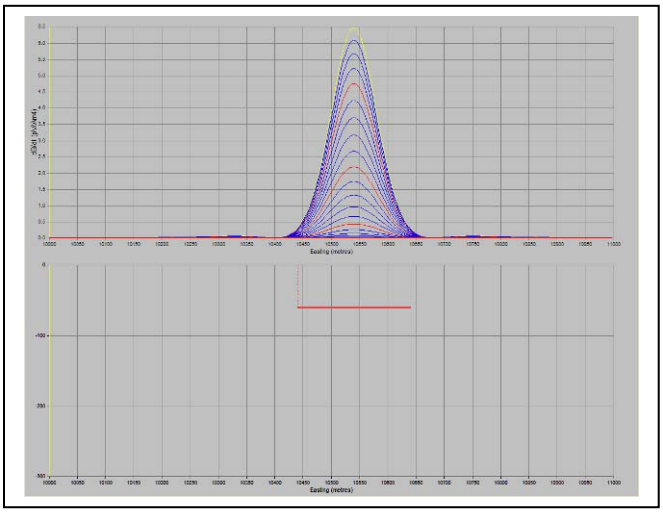


Figure C-9: dB/dt response of a shallow horizontal thin plate. Depth=100 m, CT=20 S. The EM response is normalized by the dipole moment and the Rx area.

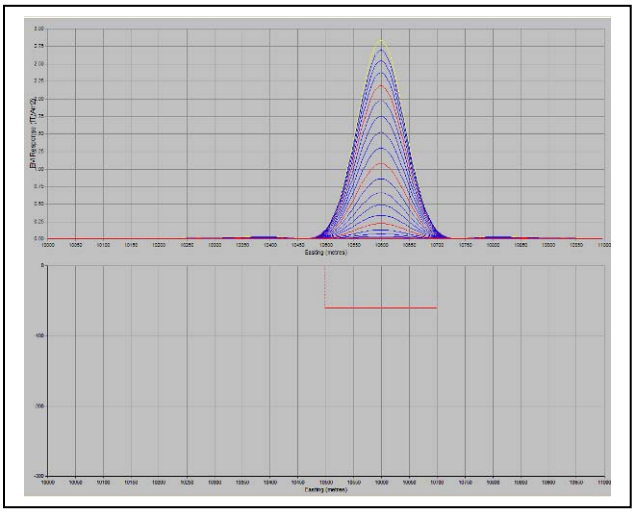


Figure C-10: B-Field response of a shallow horizontal thin plate. Depth=100 m, CT=20 S. The EM response is normalized by the dipole moment.

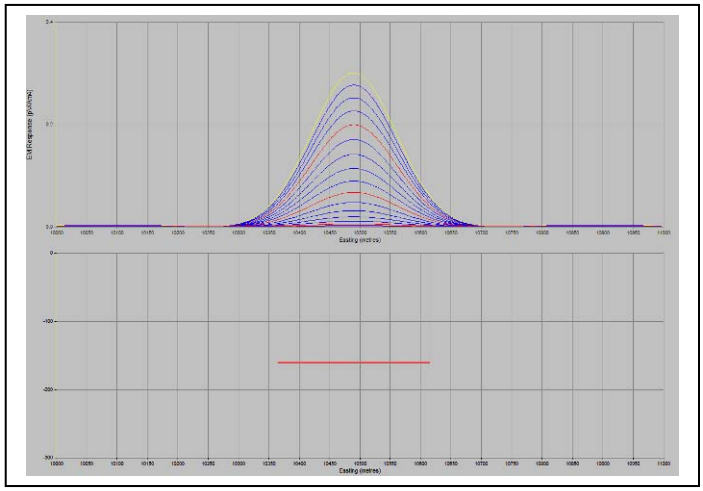


Figure C-11: dB/dt response of a deep horizontal thin plate. Depth=200 m, CT=20 S. The EM response is normalized by the dipole moment and the Rx area.

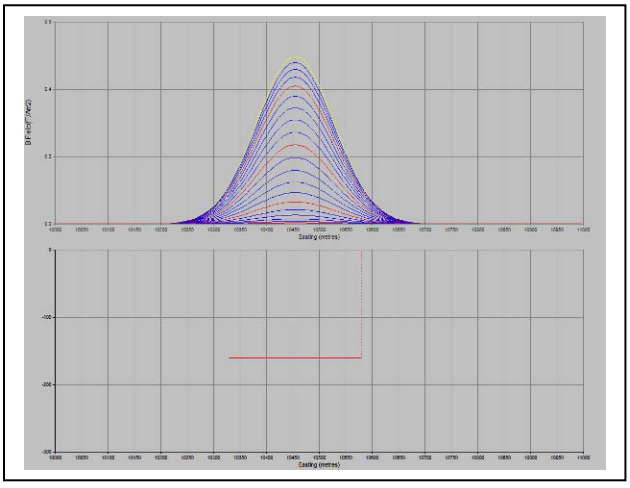


Figure C-12: B-Field response of a deep horizontal thin plate. Depth=200 m, CT=20 S. The EM response is normalized by the dipole moment.

II. THICK PLATE

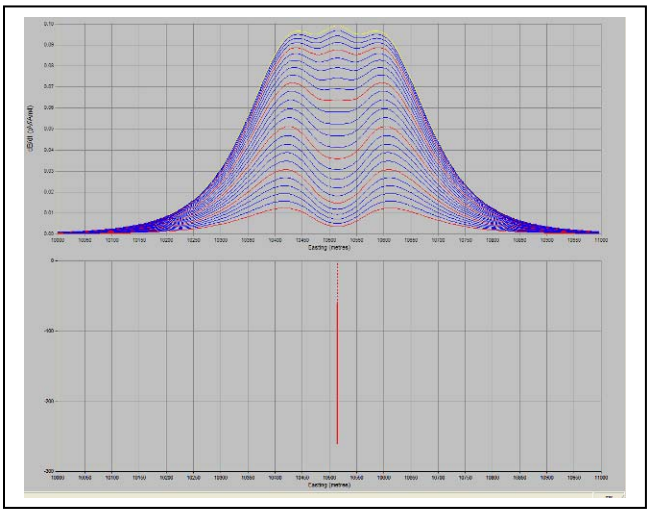


Figure C-13: dB/dt response of a shallow vertical thick plate. Depth=100 m, C=12 S/m, thickness=20 m. The EM response is normalized by the dipole moment and the Rx area.

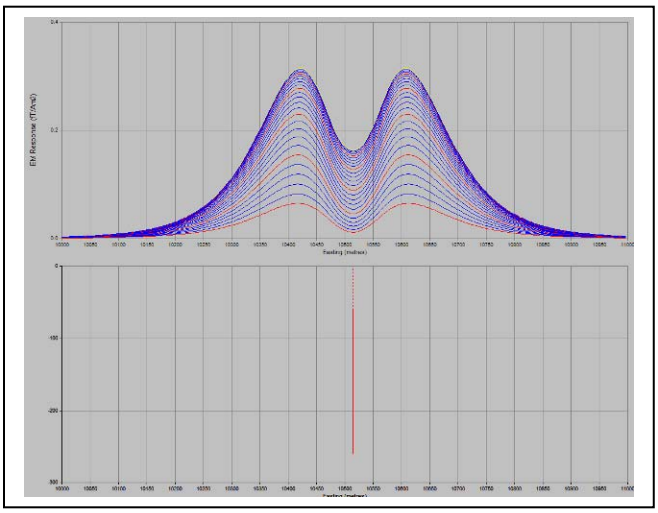


Figure C-14: B-Field response of a shallow vertical thick plate. Depth=100 m, C=12 S/m, thickness= 20 m. The EM response is normalized by the dipole moment.

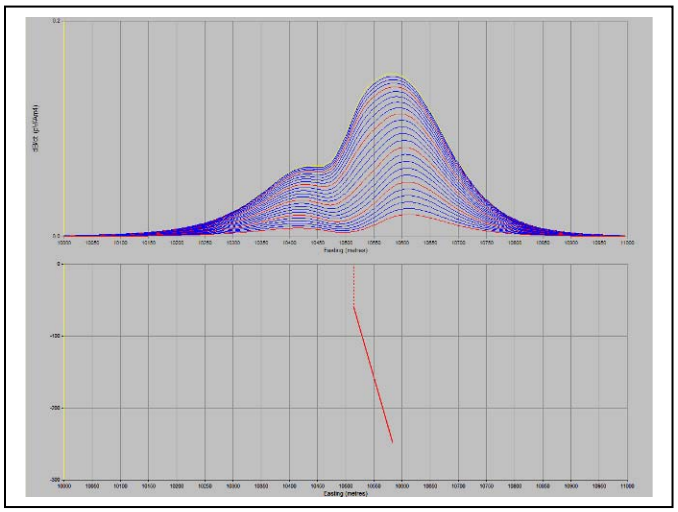


Figure C-15: dB/dt response of a shallow skewed thick plate. Depth=100 m, C=12 S/m, thickness=20 m. The EM response is normalized by the dipole moment and the Rx area.

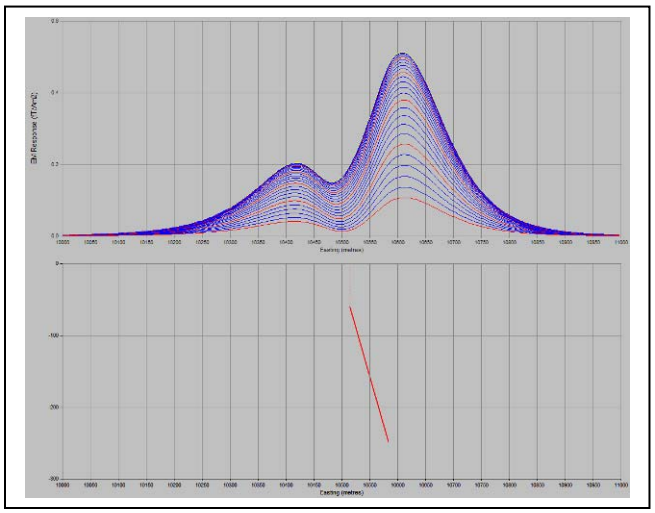


Figure C-16: B-Field response of a shallow skewed thick plate. Depth=100 m, C=12 S/m, thickness=20 m. The EM response is normalized by the dipole moment.

III. MULTIPLE THIN PLATES

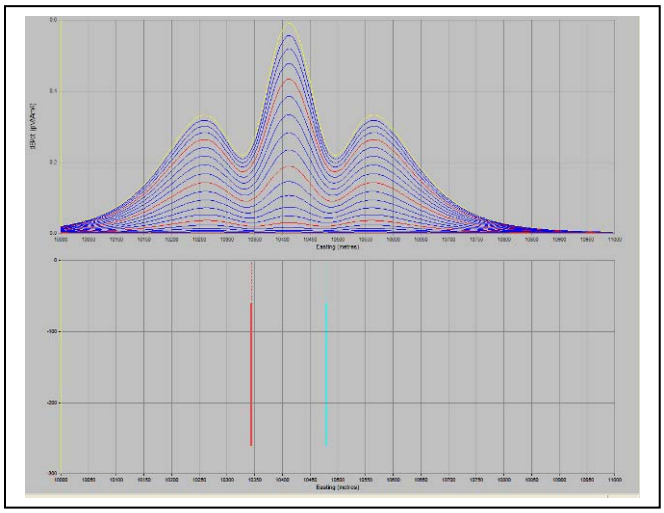


Figure C-17: dB/dt response of two vertical thin plates. Depth=100 m, CT=20 S. The EM response is normalized by the dipole moment and the Rx area.

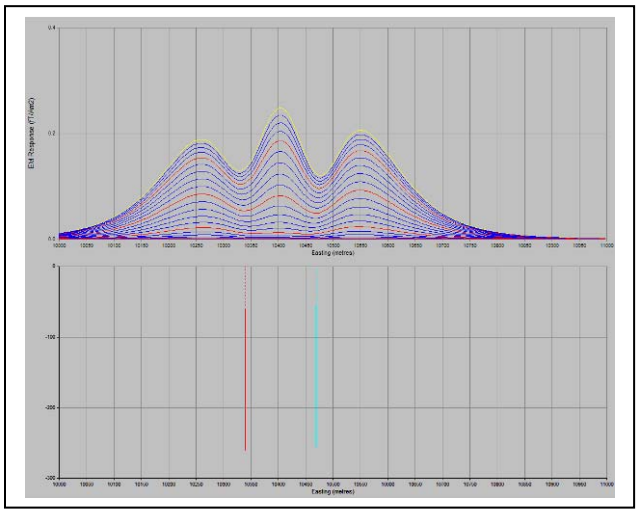


Figure C-18: B-Field response of two vertical thin plates. Depth=100 m, CT=20 S. The EM response is normalized by the dipole moment.

General Interpretation Principals

Magnetics

The total magnetic intensity responses reflect major changes in the magnetite and/or other magnetic minerals content in the underlying rocks and unconsolidated overburden. Precambrian rocks have often been subjected to intense heat and pressure during structural and metamorphic events in their history. Original signatures imprinted on these rocks at the time of formation have, it most cases, been modified, resulting in low magnetic susceptibility values.

The amplitude of magnetic anomalies, relative to the regional background, helps to assist in identifying specific magnetic and non-magnetic rock units (and conductors) related to, for example, mafic flows, mafic to ultramafic intrusives, felsic intrusives, felsic volcanics and/or sediments etc. Obviously, several geological sources can produce the same magnetic response. These ambiguities can be reduced considerably if basic geological information on the area is available to the geophysical interpreter.

In addition to simple amplitude variations, the shape of the response expressed in the wave length and the symmetry or asymmetry, is used to estimate the depth, geometric parameters and magnetization of the anomaly. For example, long narrow magnetic linears usually reflect mafic flows or intrusive dyke features. Large areas with complex magnetic patterns may be produced by intrusive bodies with significant magnetization, flat lying magnetic sills or sedimentary iron formation. Local isolated circular magnetic patterns often represent plug-like igneous intrusives such as kimberlites, pegmatites or volcanic vent areas.

Because the total magnetic intensity (TMI) responses may represent two or more closely spaced bodies within a response, the second derivative of the TMI response may be helpful for distinguishing these complexities. The second derivative is most useful in mapping near surface linears and other subtle magnetic structures that are partially masked by nearby higher amplitude magnetic features. The broad zones of higher magnetic amplitude, however, are severely attenuated in the vertical derivative results. These higher amplitude zones reflect rock units having strong magnetic susceptibility signatures. For this reason, both the TMI and the second derivative maps should be evaluated together.

Theoretically, the second derivative, zero contour or color delineates the contacts or limits of large sources with near vertical dip and shallow depth to the top. The vertical gradient map also aids in determining contact zones between rocks with a susceptibility contrast, however, different, more complicated rules of thumb apply.

Concentric Loop EM Systems

Concentric systems with horizontal transmitter and receiver antennae produce much larger responses for flat lying conductors as contrasted with vertical plate-like conductors. The amount of current developing on the flat upper surface of targets having a substantial area in this dimension, are the direct result of the effective coupling angle, between the primary magnetic field and the flat surface area. One therefore, must not compare the amplitude/conductance of responses generated from flat lying bodies with those derived from near vertical plates; their ratios will be quite different for similar conductances.

Determining dip angle is very accurate for plates with dip angles greater than 30º. For angles less than 30º to 0º, the sensitivity is low and dips can not be distinguished accurately in the presence of normal survey noise levels.

A plate like body that has near vertical position will display a two shoulder, classic **M** shaped response with a distinctive separation distance between peaks for a given depth to top.

It is sometimes difficult to distinguish between responses associated with the edge effects of flat lying conductors and poorly conductive bedrock conductors. Poorly conductive bedrock conductors having low dip angles will also exhibit responses that may be interpreted as surficial overburden conductors. In some situations, the conductive response has line to line continuity and some magnetic correlation providing possible evidence that the response is related to an actual bedrock source.

The EM interpretation process used, places considerable emphasis on determining an understanding of the general conductive patterns in the area of interest. Each area has different characteristics and these can effectively guide the detailed process used.

The first stage is to determine which time gates are most descriptive of the overall conductance patterns. Maps of the time gates that represent the range of responses can be very informative.

Next, stacking the relevant channels as profiles on the flight path together with the second vertical derivative of the TMI is very helpful in revealing correlations between the EM and Magnetics.

Next, key lines can be profiled as single lines to emphasize specific characteristics of a conductor or the relationship of one conductor to another on the same line. Resistivity Depth sections can be constructed to show the relationship of conductive overburden or conductive bedrock with the conductive anomaly.

_____

Roger Barlow
Consultant

_____

Nasreddine Bournas, P. Geo.
Geotech Ltd.

November 2008

APPENDIX III

GEOPHYSICAL REPORT BY CONDOR CONSULTING INC.

Condor Consulting, Inc.

REPORT ON PROCESSING & ANALYSIS OF

VTEM 30 HZ EM AND MAGNETICS DATA

MOR, MOR EXTENSION, CABIN LAKE AND CARIBOU

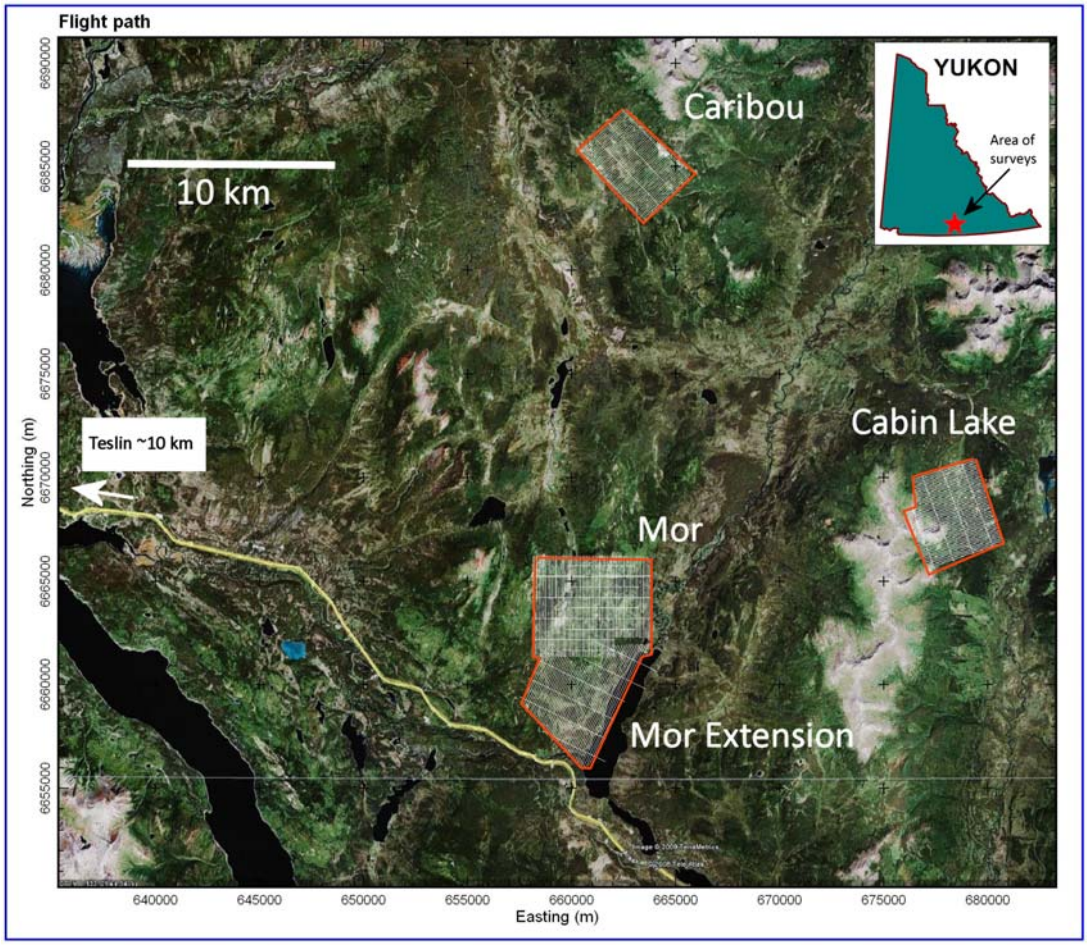
PROPERTIES

TESLIN AREA, YUKON TERRITORY

FOR

TARSIS CAPITAL CORP.

FEBRUARY 2009



Condor Consulting
Lakewood Colorado
USA



REPORT ON PROCESSING & ANALYSIS OF

VTEM 30 HZ EM AND MAGNETICS DATA

MOR, MOR EXTENSION, CABIN LAKE AND CARIBOU

PROPERTIES

TESLIN AREA, YUKON TERRITORY

FOR

TARSIS CAPITAL CORP.

FEBRUARY 2009

Condor Consulting
Lakewood Colorado
USA

CONTENTS

1. SUMMARY 1

2. INTRODUCTION 2
VTEM Survey 2
Target Model 3
Local Geology 5

3. PROCESSING, ANALYSIS TECHNIQUES AND PRODUCTS 9
PROCESSING 9
EM Data Processing 9
Conductivity 3D Model 10
Magnetic Data Processing 10
Magnetic Data Modeling 10
EM ANALYSIS TECHNIQUES 10
Profile Analysis 10
Picking 10
Wide Zones 11
Target Zones 11
PRODUCTS 11
Table 3-1 Survey Products 12

4. SURVEY RESULTS 14
Data Quality 14
Magnetic Results 14
Mor…… 14
Cabin Lake 15
Caribou 16
EM Survey Results 16
Mor…….. 16
Cabin Lake 24
Caribou 27
Discussion 29
Mor……. 29
Cabin Lake 29
Caribou 29

5. CONCLUSIONS & RECOMMENDATIONS 30

6. REFERENCES 31

7. APPENDICES 33
APPENDIX A: BACKGROUND ON EM PROCESSING 34

APPENDIX B: ANOMALY LISTING 35
MOR…… 36
CABIN LAKE 37
CARIBOU 38
APPENDIX C: NOTES ON MAGNETIC PROCESSING & EM3D MODELS 39
APPENDIX D: ARCHIVE DVD 40

1. SUMMARY

This report covers the processing and analysis performed by Condor Consulting, Inc. of VTEM EM and magnetic surveys on three properties held by Tarsis Capital Corp. and being operated by Archer Cathro & Associates. The properties are the Mor, Cabin Lake and Caribou and are located east and north of community of Teslin, Yukon Territory. The primary deposit model for all three properties is VMS.

Mineralization located on the Mor property shows a strong response in the VTEM survey. Follow-up of the 2007 VTEM survey (prior to Condor Consulting, Inc.'s involvement) revealed another zone of mineralization on Mor. The present assessment suggests both areas of known mineralization have likely extensions at depth which are deemed to warrant follow-up. As well several other zones of interest were recognized and are also recommended for follow-up.

On the Cabin Lake property, one zone of interest was indentified and is recommended for further work. This zone is believed to be at least several 100 meters deep and therefore a staged follow up is recommended to upgrade the target prior to drilling.

On the Caribou property, only one bedrock conductor was recognized. As this feature lies on the edge of the survey block, follow-up work to upgrade and better define the overall strike of this zone is recommended prior to drill testing.

2. INTRODUCTION

VTEM Survey

At the request of Tarsis Capital Corp. (Tarsis), Condor Consulting Inc. (Condor) has undertaken to process and analyze VTEM 30 Hz EM and magnetics data over Tarsis's Mor, Mor Extension, Cabin Lake and Caribou properties located east of Teslin, Yukon Territory. The surveys were flown in 2007 and 2008 by Geotech Ltd.; full details of the survey and equipment specifications are provided in Lev, 2007, Lev, 2008, Orlowski et al 2008 and Orlowski et al 2009. These reports are provided in digital form in Appendix D, the archive DVD.

The location of the surveys is shown in Figure 1 and the path plot in Figure 2. A total of 867 line km of data were processed and analyzed.

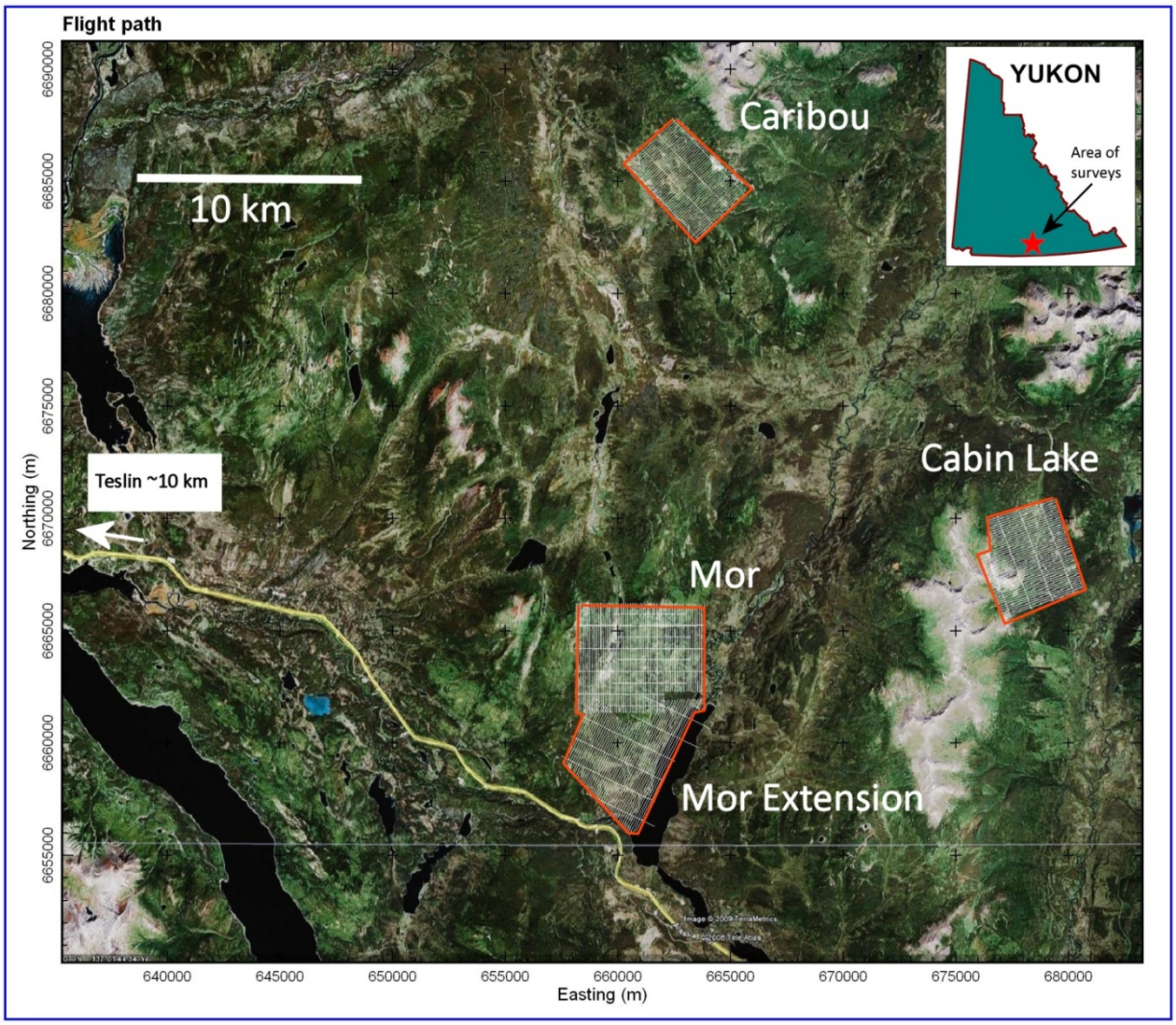


Figure 1: Location of VTEM surveys.

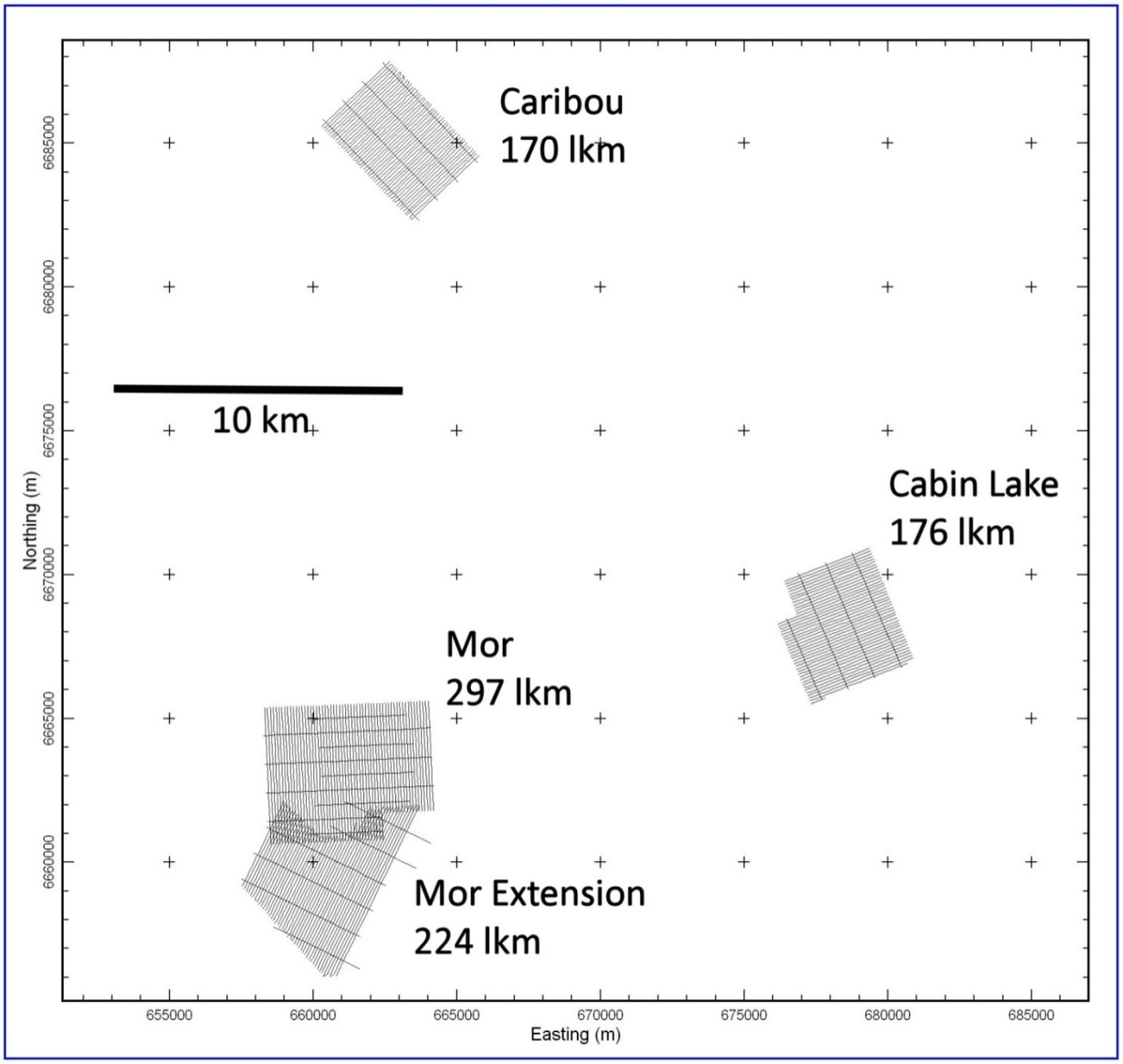


Figure 2: Flight path plots for VTEM surveys.

Target Model

The regional geology for the area is shown in Figure 3 (Downie 2007). The primary target model is VHMS (volcanic hosted massive sulfide) but Cabin Lake has the potential for intrusive related mineralization as well. The VMS-style deposits would contain significant sulfides and would be expected to be at least moderately conductive. An example of such a deposit in the area is the Kudz Ze Kayah (Holroyd et al 1997). They report the deposit had a high conductance (40 S) and strong magnetic response (700-1 000 nT). Figure 4 shows the HLEM (horizontal loop EM or MaxMin) response over the deposit, superimposed on the magnetic response. A copy of their paper is provided in Appendix D.

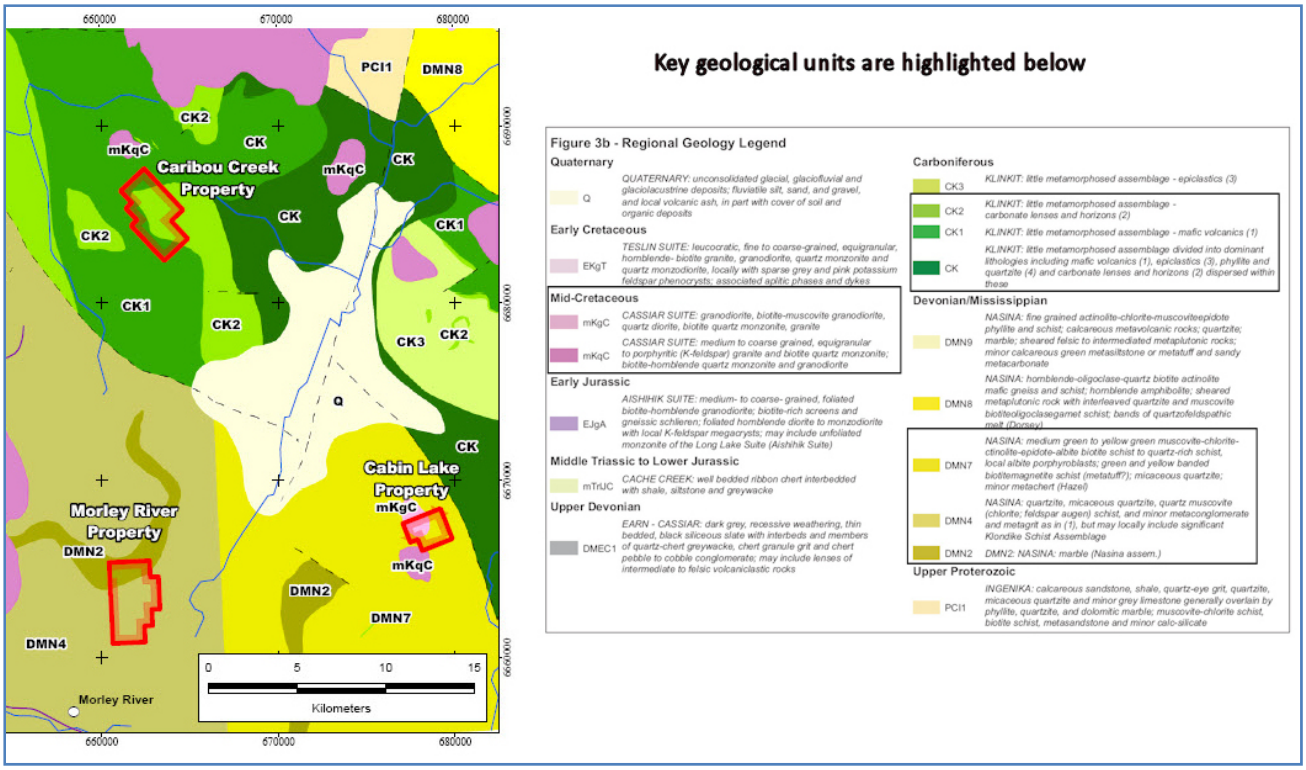


Figure 3: Regional geology for Mor, Cabin Lake and Caribou properties (from Downie 2007).

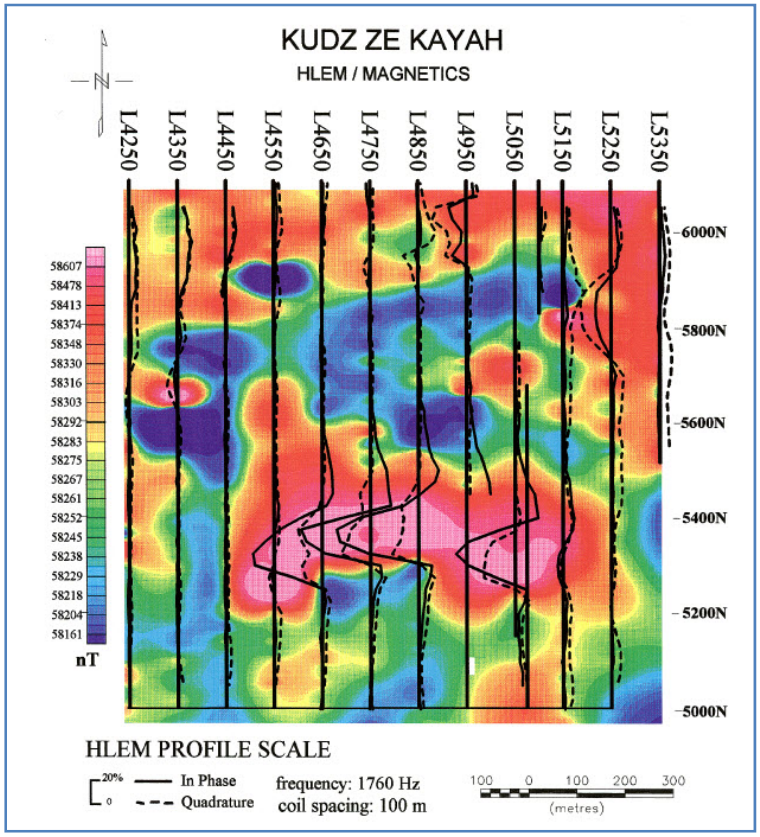


Figure 4: HLEM and magnetic results (from Holroyd et al 1997).

They note the presence of "mudstones and shales which typically have pyrrhotite disseminations, and are variably carbonaceous, making these metasediments locally both magnetic and conductive". While not an issue in the present study, these responsive sediments are a frequent part of the mineralogically favorable geology elsewhere in the Yukon.

Local Geology

MOR

Of the three projects, the Mor area is best known. The local geology is provided in Downie (2007):

The Morley River Property is mainly underlain by a thick sequence of green quartz-chlorite schist and chlorite schist of which protoliths are interpreted as mafic to intermediate volcanic tuffs and minor flows. This assemblage is mainly composed of fine grained, bright to dark green, well foliated chlorite schists/mafic tuff to lapilli tuff. The mafic rocks are interbedded with quartz chlorite schist/intermediate tuff on a centimeter to meter scale. These rocks contain varying amounts of layer parallel quartz and feldspar. Quartzite/chert was also observed locally as interbeds within the mafic dominated succession but never sufficiently thick to form a mappable unit. The rocks are strongly deformed and have a strong, nearly parallel to layering, schistosity which generally strikes east and dips moderately to the south. The sequence has been significantly thickened by tight high amplitude folds which were observed at an outcrop scale. Metamorphic grade is middle greenschist facies. This assemblage of dominantly mafic volcanics may correlate with the "greenstone sequence" of the Big Salmon Complex mapped by Mihalynuk et al (1998).

The northeast portion of the property is underlain by a grey-white, thickly bedded, medium to coarsegrained marble. This unit was observed in flat lying, conformable contact with and overlying the greenstone sequence described above. Bedding in the recrystallized limestone strikes east and dips south at 30 degrees.

One historic zone of mineralization called the Discovery Zone has been recognized and a second zone has been defined in recent work as a follow-up to the 2007 VTEM survey (source Tarsis web site: www.tarsis.ca). Downie (2007) provides the following description of the Discovery Zone:

On the Morley River Property, the main mineralized zone consists of at least four separate quartz-sericite schist/ rhyolitic tuff horizons within a dominantly mafic volcanic sequence. These horizons, where exposed, range from 20 centimeters to 1.75 meters thick, are strongly gossanous and contain pyrite with locally significant amounts of chalcopyrite, gold and silver. Mafic schists in contact with the mineralized quartz-sericite schist units are strongly pyritic and commonly anomalous in copper. The quartz-sericite schist units have been traced over a strike length of 900 meters.

These two areas are outlined in Figure 5. Both zones have a VMS affinity and could be expected to be quite conductive and likely magnetic. A detailed image over the Discovery Zone is shown in Figure 6. Prior to the first VTEM survey being performed over Mor in 2007, an IP survey was conducted over the Discovery area (Power 2004). The results of this survey are shown in Figure 7. Also shown on this figure is the basic geological mapping for the area.

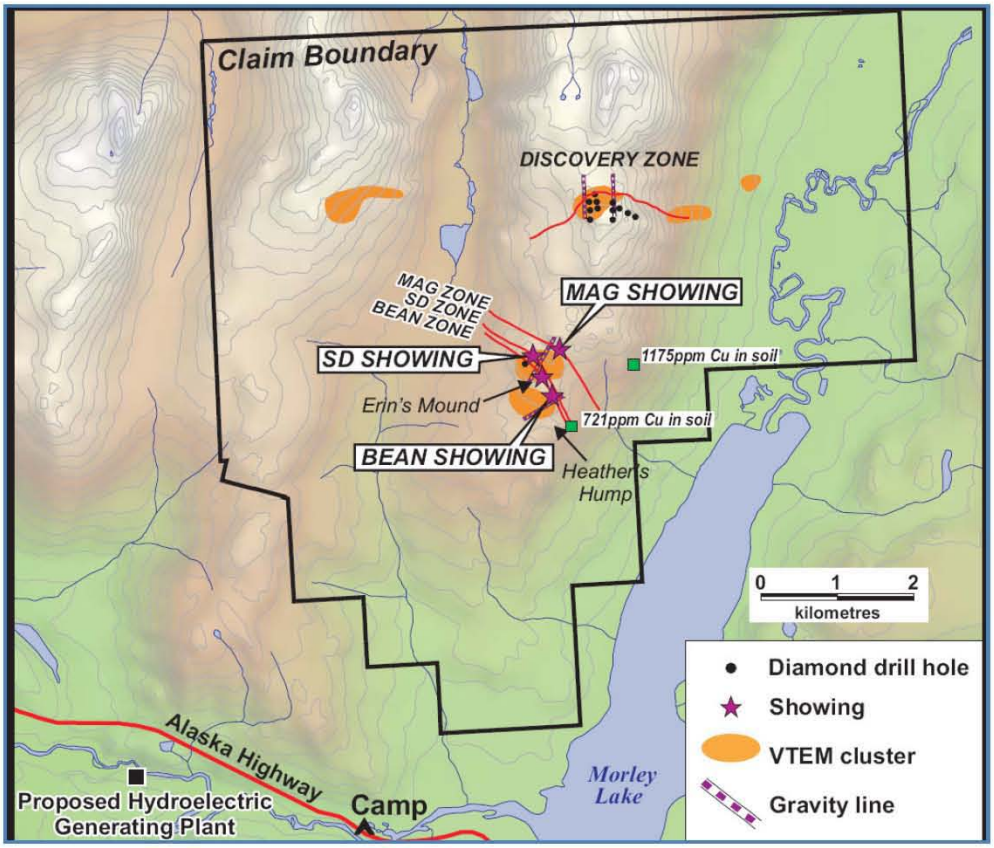


Figure 5: Location of major showings on the Mor property (source-Tarsis web site).

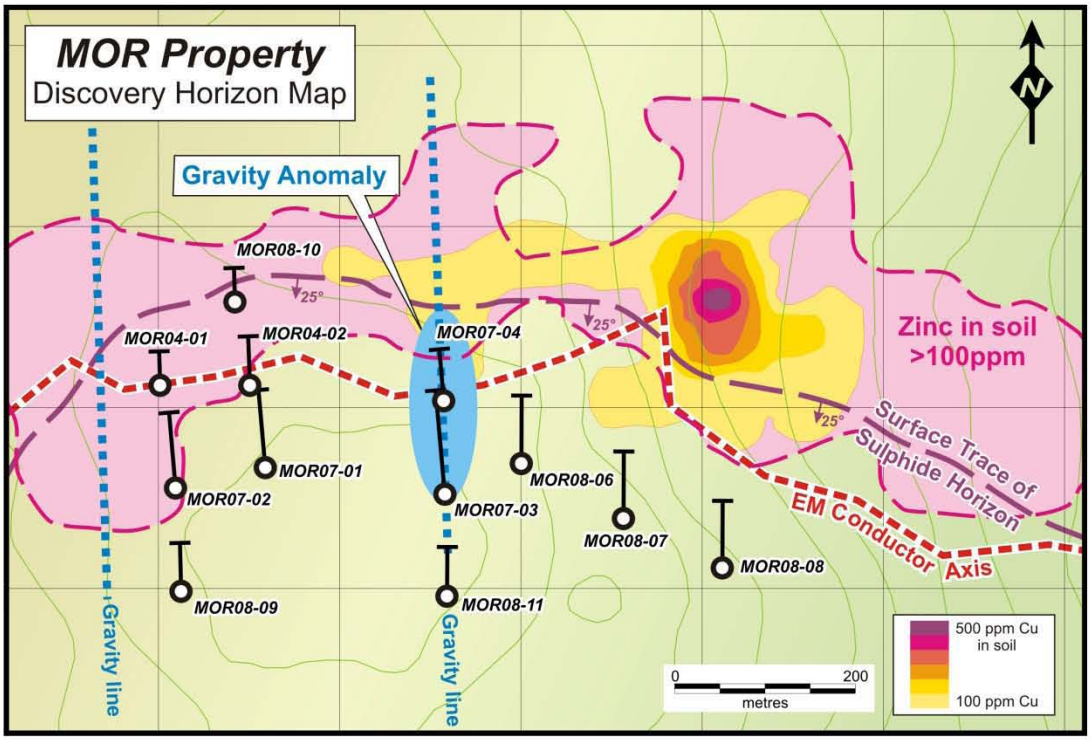


Figure 6: Mor-Discovery Zone showing drilling and geochemical results.

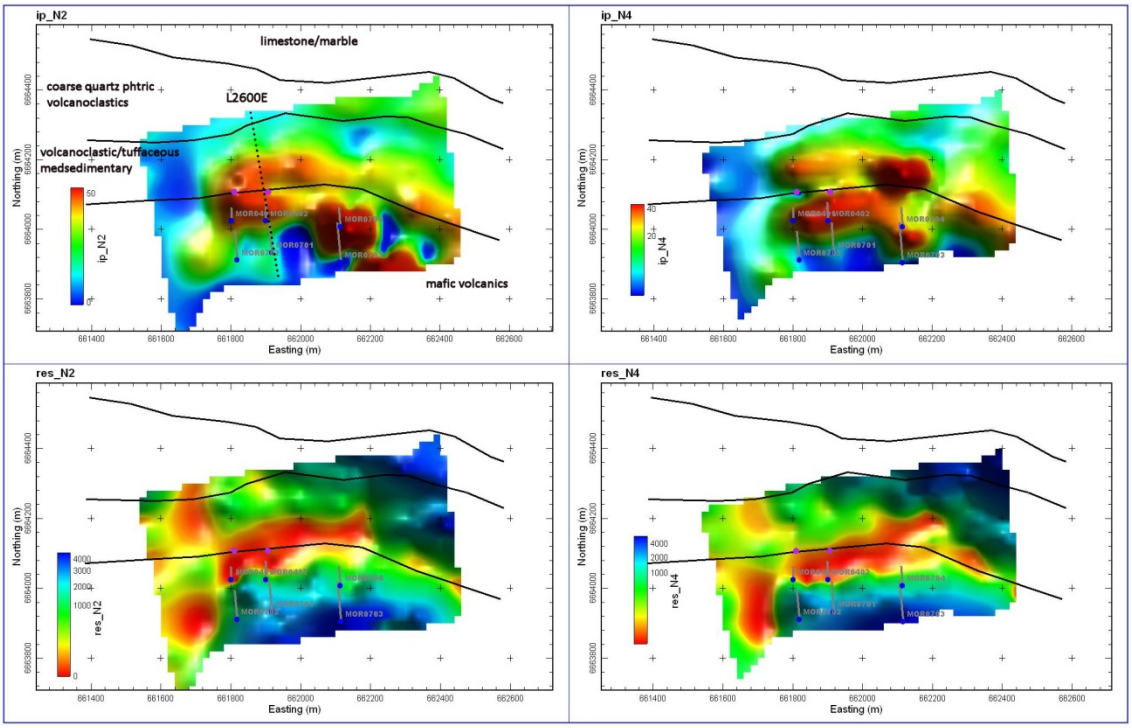


Figure 7: Mor-Discovery Zone: IP chargeability and resistivity; geology annotated in upper left image.

The IP results show the Discovery Zone is a distinct chargeability high and resistivity low. An attempt was made to correlate between the drilling results and IP outcomes and Figure 8 shows the representation of this assessment. Given the narrowness of the mineralized zones and averaging that

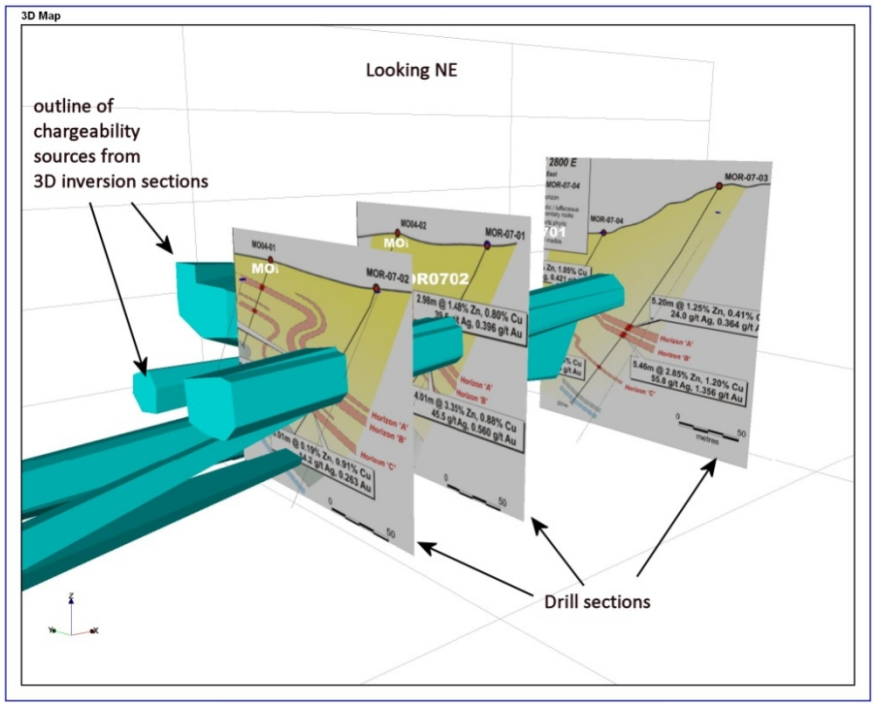


Figure 8: Mor-Discovery Zone: 3D chargeability model and drill sections.

takes place in with the IP measurement and subsequent inversion, the correlation is deemed to be satisfactory. A section of the resistivity inversion through roughly the center of the Zone (L2600E) is shown in Figure 9 (located in Figure 7 upper left image). From the inversion processing, the mineralized zone appears to have a resistivity the order of 10-50 ohm-m. This level of response would be sufficient to be detected with an airborne EM survey assuming there was a sufficient volume of material.

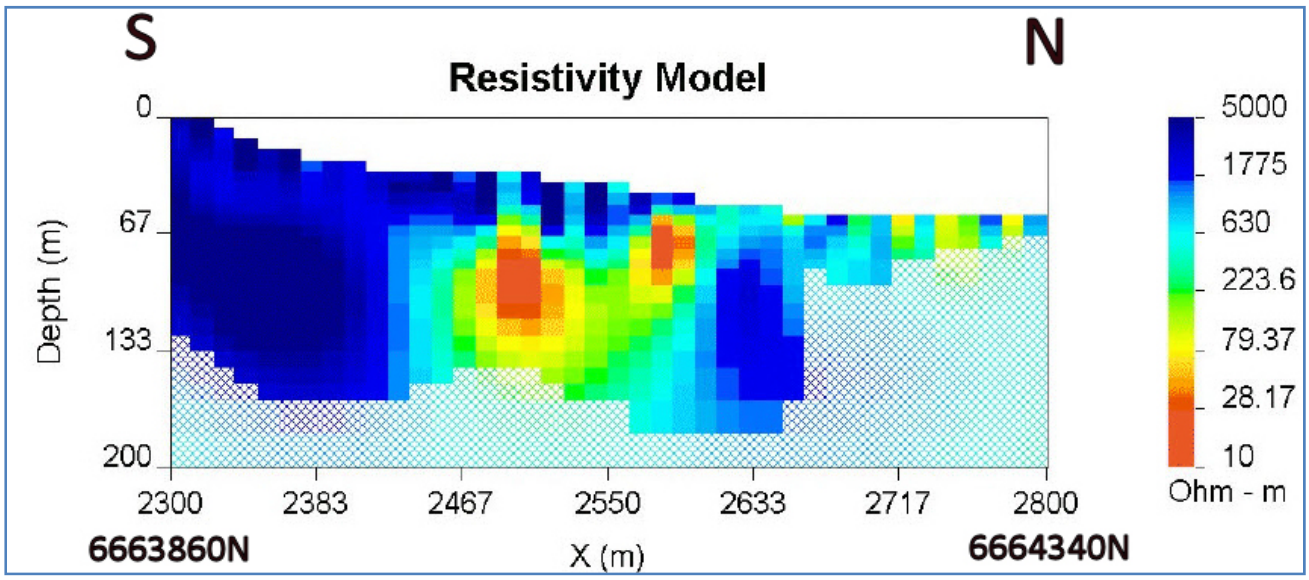


Figure 9: Mor-Discovery Zone: Inverted resistivity data for L2600E-located in Figure 7; Source-Power 2004.

Cabin Lake

No geology (apart from regional shown in Figure 3) is available.

Caribou

No geology (apart from regional shown in Figure 3) is available.

3. PROCESSING, ANALYSIS TECHNIQUES AND PRODUCTS

PROCESSING

To enhance the data and to assist interpretation, the following processing steps were carried out on the VTEM EM and magnetic data. The survey contractor provided the client with both Z off-time (dB/dT) and Z on-time (B-f) data (no X or Y data is recorded with VTEM). Condor processed both data types and selected what was deemed the best outcome for the various products provided.

EM Data Processing

Layered-Earth Inversion

The layered-earth inversion (LEI) algorithm models the EM data with a 28-layered earth model (Farquharson and Oldenburg, 1993, Ellis 1998), increasing in thickness from the surface to depth in an approximately logarithmic fashion. The first layer was 5 m thick and the deepest was 232 m thick. A starting model of 1 000 ohm-m (0.001 S/m) was used, with a reference model of 10 000 ohm-m (0.0001 S/m). The reference model is what the program defaults to at depth when there is no longer enough information to further refine the inversion outcome. The results of the inversion are presented in the form of a conductivity depth section (CDS).

Time Constant: AdTau

The AdTau program calculates the time constant (tau) from time domain decay data. The program is termed AdTau since rather than using a fixed suite of channels as commonly done, the user sets a noise level and depending on the local characteristics of the data, the program will then select the set of five channels above this noise level. In resistive areas, the earlier channels will tend to be used, whereas in conductive terrains the latest channels available can generally be used. Figure 10 shows a typical decay fit; in this case, the last five channels are used.

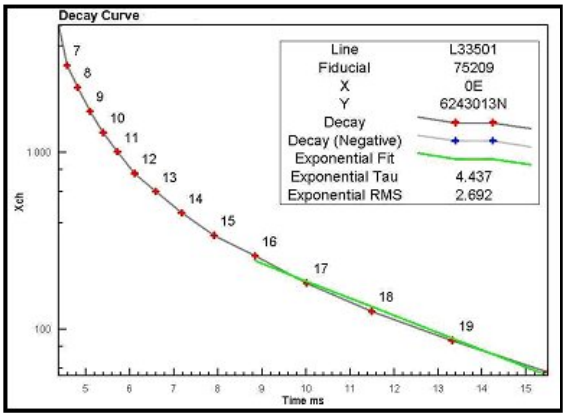


Figure 10: Typical decay showing the derivation of AdTau.

Conductivity 3D Model

Using the 1D inversions created from the EM data, a 3D voxel model of the conductivity has been created using the encom pa application.

Additional information on the EM processing is provided in Appendix A.

Magnetic Data Processing

In addition to the normal filters available in the Geosoft application, additional processing was done using encom pa software and algorithms described by Shi and Butt (2004) – this paper is included in Appendix C. Where one of these products is used, the prefix ZS is attached to the file name.

Magnetic Data Modeling

The magnetic data for the Mor survey block was modeled using the code Mag3D; this is a voxel-style inversion program developed at the University of British Colombia (Li and Oldenburg 1996). Details on the modeling are provided in Appendix C.

EM ANALYSIS TECHNIQUES

Profile Analysis

For discrete plate-like targets, the VTEM system produces two main types of responses; those termed inductively thin or double-peaked responses (DPR) and those termed inductively thick or single-peak responses (SPR). These basic shapes are shown in profile form in Figure 11. While these two classes of response have been picked separately, for the purposes of this review they are treated as having the same geological significance.

Picking

The MultiPlot™[1] display was the primary means to identify and rank the anomalies. This overall process is termed anomaly picking and was done on a line-by-line basis, with several passes being required to finalize the process. An EM picking scheme was used that made use of the following data:

- EM profiles
- AdTau, power line monitor and magnetic profiles and grids
- Conductivity Depth Sections (CDS)

[1] The MultiPlot is produced using the encom pa software from Encom Technology Pty. Ltd.

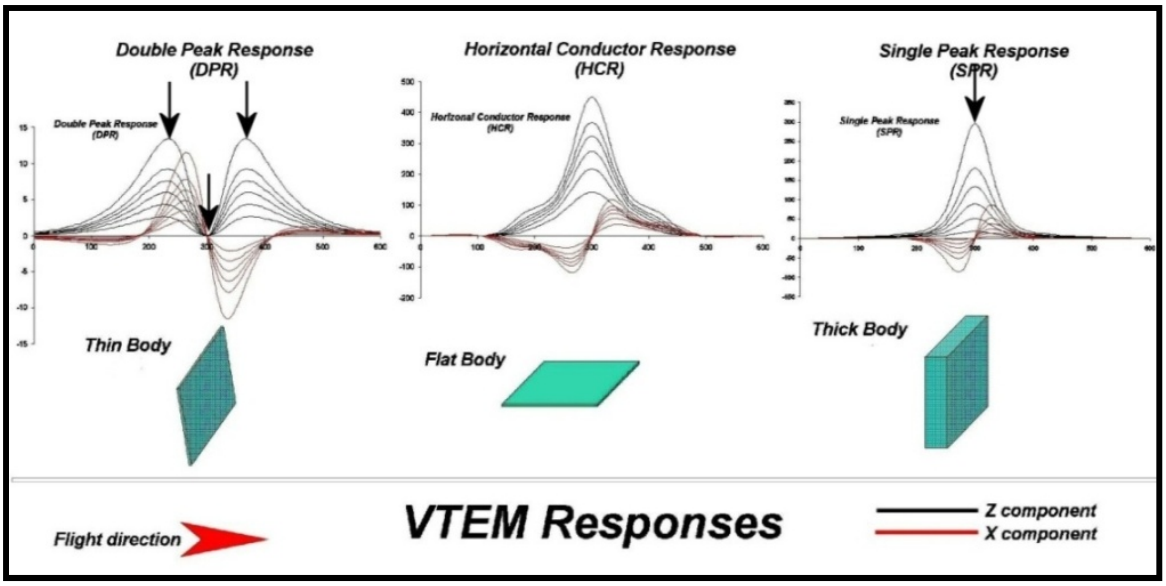


Figure 11: Examples of VTEM responses.

Wide Zones

Wide zones (WZ) are a category of picking where there a broader zone of conductivity recognized in the data. Near-surface WZ are typically related to surficial geology whereas deeper WZ are related to bedrock sources. Frequently discrete conductors and WZ are picked in the same location and represent different aspects of the same mineralized system.

Target Zones

Groupings of conductors are termed Target Zones or TZ. A TZ is deemed as a logical grouping of conductors within the data set and is based on an assessment of the distribution of individual conductor picks, plus any other available geoscience data. The TZs are then prioritized for follow up work based on their overall geophysical character and how this relates to the defined target models for the project.

PRODUCTS

Table 3-1 lists the maps and products that are provided. Other products can be prepared from the existing dataset, if required.

Base Maps: All maps are created using the following parameters:

Projection Description:
Datum: WGS84
Ellipsoid: WGS84
Projection: UTM (Zone: 8N)

Central Meridian: 135ºW

False Northing: 0

False Easting: 500 000

Scale Factor: 0.9996

Table 3-1 Survey Products

TargetMaps @ 1:30 000 (1 hard copy + digital)

All maps show the indicated themes as well as the Condor discrete picks and Target Zones

- Total magnetic Intensity (TMI)
- ZS TMI-Tilt
- EM (dB/dT) Ch 1
- AdTau (dB/dT 0.002 pV/Am^4) + Wide Zones
- DTM (from VTEM survey)

MultiPlots™ @ 1:20 000 (digital only)

Mini-Plates™: TMI, TMI-ZS_Tilt and as noted below for each area:

Cabin Lake: Miniplate 3: EM B-f Ch 1, Miniplate 4: AdTau B-f 0.01 pVms/Am^4

Caribou: Miniplate 3: EM dB/dT Ch 1, Miniplate 4: AdTau dB/dT 0.002 pV/Am^4

MOR: Miniplate 3: EM B-f Ch 1, Miniplate 4: AdTau B-f 0.01 pVms/Am^4

MOR-Ext: Miniplate 3: EM dB/dT Ch 1, Miniplate 4: AdTau dB/dT 0.002 pV/Am^4

On each MultiPlot™ the picked anomalies and Target Zones are indicated along with the following:

- Profiles-EM dB/dT Ch 1-25
- Profiles-EM B-f Ch 1-25
- Profiles-Magnetics: TMI, 1st Vertical derivative and Analytic Signal
- Profiles-AdTau dB/dT (0.005 pV/ Am^4); B-f (0.005 pVms/Am^4) + power line monitor
- LEI-CDS dB/dT;
  Cabin: (0.1-100 mS/m) + bird height
  Caribou: (0.1-10 mS/m) + bird height
  Mor: (0.1-50 mS/m) + bird height + drill holes[2] (± 50 m from section)
  Mor Ext: (0.1-50 mS/m) + bird height)

[2] The drill holes displayed are from the data base provided by the client.

- Susceptibility Depth Section + drill holes (± 50 m from section)
- TrackMap 1: TMI-ZS Tilt filter

Mag3D Modeling

The following products are provided as part of the Mag3D modeling. Some are stand-alone and some are imbedded with other products; the letters S and I are used to flag which; S= stand-alone and I = imbedded.

- UBC mesh and sus files (S)
- Magnetic model X, Y and Z format (S)
- 3D DXFs (S)
- Susceptibility Depth Section (I- in MultiPlots)
- AVI of model (S)
- Notes on processing (S)-Appendix C

Conductivity 3D Model

Using the 1D inversions created from the EM data, a 3D voxel model of the conductivity has been created using the encom pa application. The suite of products (primary and derived) is listed below.

- UBC mesh and con files (S)
- Conductivity model X, Y and Z format (S)
- 3D DXFs (S)
- AVI of model (S)

Processing and Analysis Report (1 copy)

On the Archive DVD (Appendix D) the following files are provided:

-Digital archive in Geosoft format

-Profile Analyst session file (to create MultiPlots™)

-Anomaly data bases in Excel and Geosoft formats

-PDFs of TargetMaps and MultiPlots™

-Processing and Analysis Report (PDF)

-Set of images from report (higher resolution than is possible to reproduce in the report).

- encom pa Viewer (provided at no cost)

4. SURVEY RESULTS

Data Quality

The quality of the EM and magnetic data was deemed to be acceptable and shows noise levels similar to other VTEM data sets acquired in the same time frame as the present survey.

Magnetic Results

Mor

The magnetic results (TMI and TMI-Tilt) are shown in Figure 12. A number of the major linears have been marked on the images. There appears to be at least three magnetic domains or blocks in the survey area; these have been indicated in Figure 12-left image. Block A shows an alternating series of N75W trending bands with several intrusive areas or tightly folded centers (circled in orange). The Discovery Zone lies on the northern edge of one of these more discrete zones. These discrete zones could represent the locations of volcanic centers that have breached the paleostratigraphy. Massive sulfide deposits are associated with these volcanic centers.

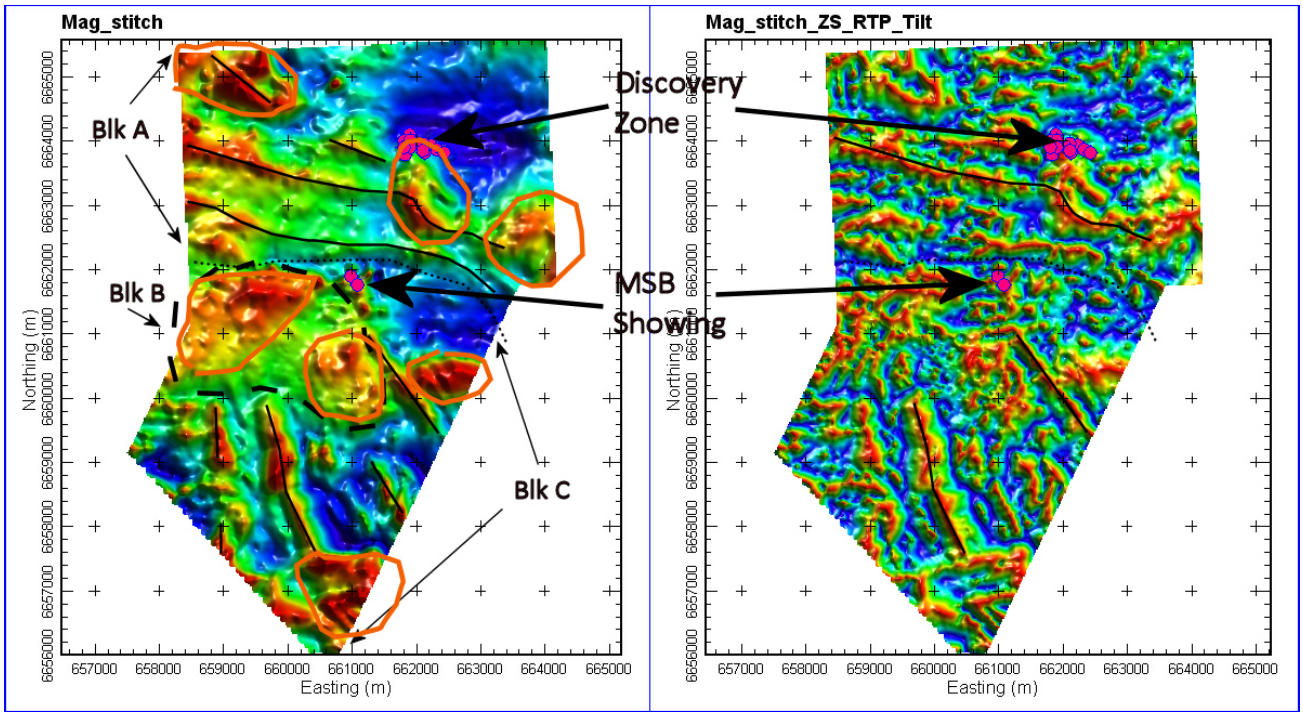


Figure 12: Mor/Mor Extension: TMI and TMI-Tilt with interpretive layer and 2007-2008 drilling (red dots).

Mag3D

A Mag3D model (UBC voxel-style model) was run for the Mor 2007 survey and the provided products are listed in Table 3-1. A snap-shot of the Mag3D model with the Tarsis drilling is shown in Figure 13. The 3D model appears to reinforce the association of mineralization at the edges of discrete magnetic zones. This could be useful in targeting other prospective areas on the property.

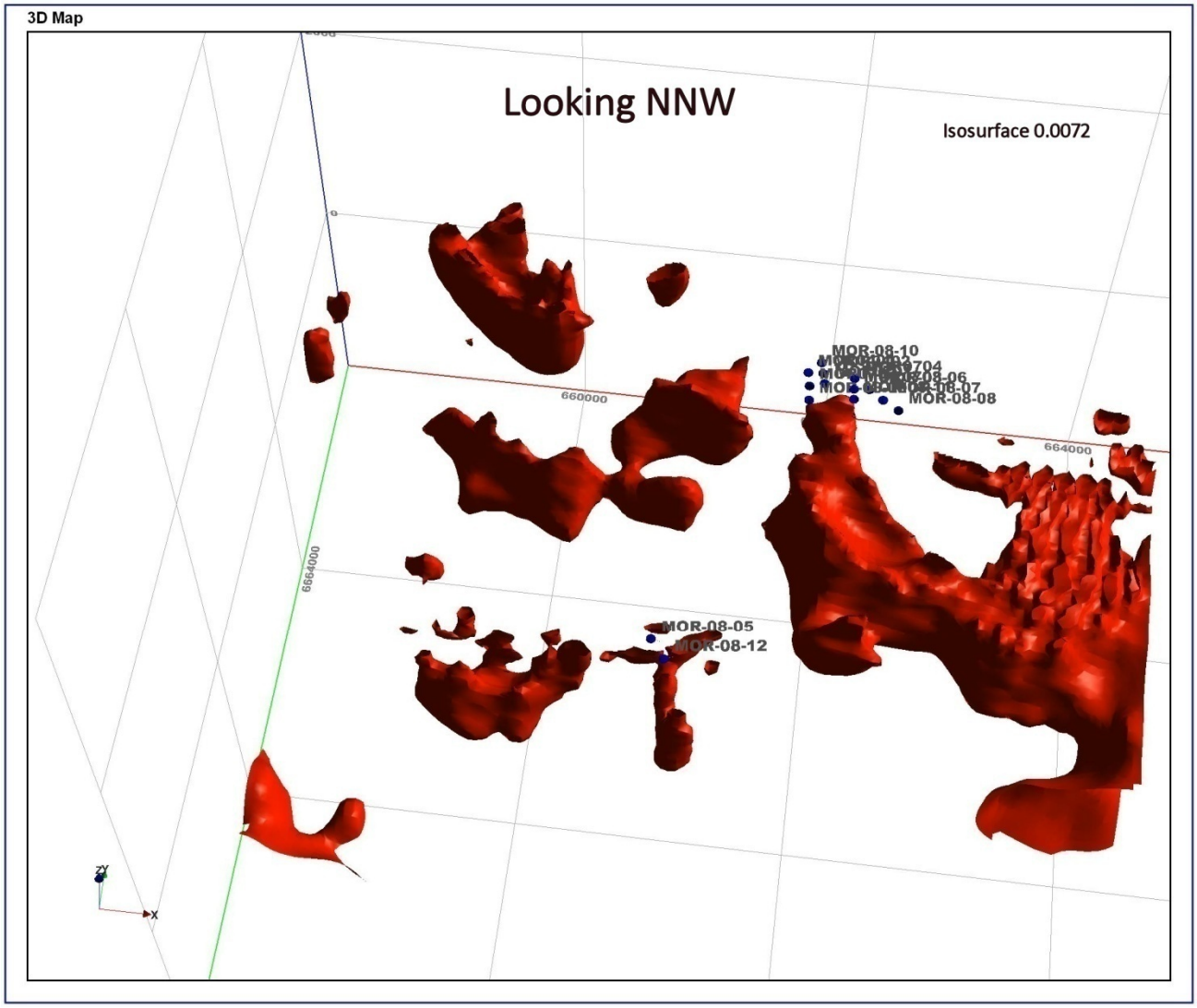


Figure 13: Mor: Mag3D model; 0.0072 SI isosurface + 2007-2008 drilling.

Cabin Lake

The TMI and TMI-Tilt images are shown in Figure 14. A number of the major linears and closures have been annotated on these images. The regional geology map suggests there are intrusives located in the northern end of the block and the SW corner (granodiorite and quartz monzonite). There are

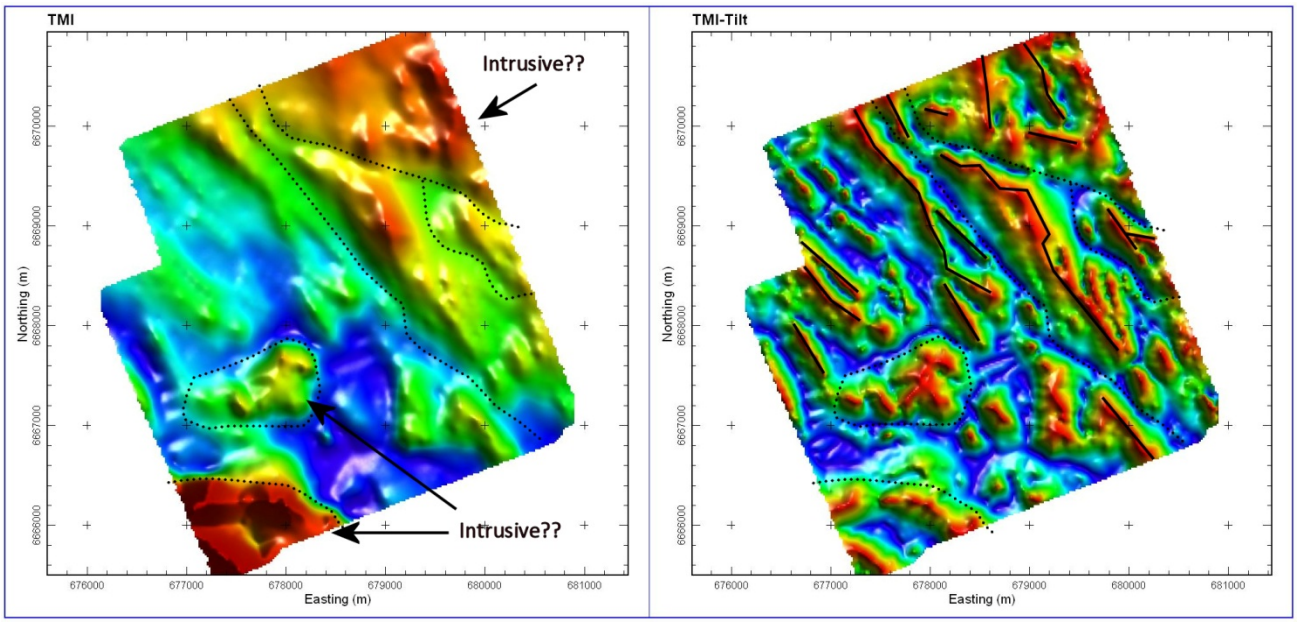


Figure 14: Cabin Lake: TMI and TMI-Tilt with interpretation.

two discrete or semi-discrete sources in the SW part of the block that are suggestive of being intrusives. A zone of elevated magnetic response in the northern end of the block could be intrusive rocks as well. The grain of the magnetic response otherwise is close to N40W. There are no 'knots' of discrete response along the linears as noted on the Mor property.

Caribou

The TMI and TMI-Tilt images are shown in Figure 15. The regional geology indicates there is a mixture of mafic volcanics and carbonate lenses. The images are dominated by a number of semi-discrete highs, showing locally what appears to be tight folding. This terrain does not look like either Cabin Lake or Mor.

EM Survey Results

Mor

The EM Channel 1 and AdTau (B-field) is shown in Figure 16. The two zones of known mineralization are highlighted with the drill hole collars (white dots). The central zone (designated as Mag Showing, SD Showing and Bean Showing in Figure 5 or shortened to MSB Area for this report) appears as a strong, very discrete feature, especially in the AdTau image. The Discovery Zone appears reasonably discrete in the EM Channel 1 image but less so in the AdTau where the zone merges into a larger more formational type feature to the east. The Mor Extension block appears to host only several large formational conductors and no discrete bedrock features were recognized.

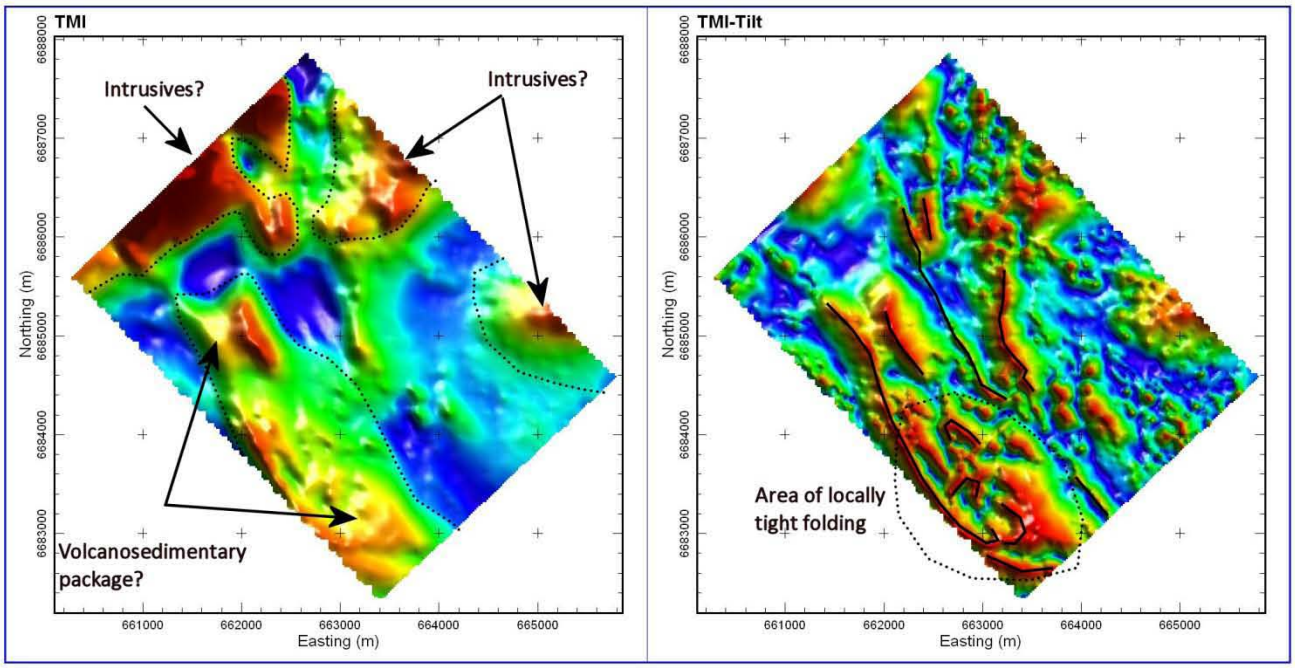


Figure 15: Caribou: TMI and TMI-Tilt with interpretation.

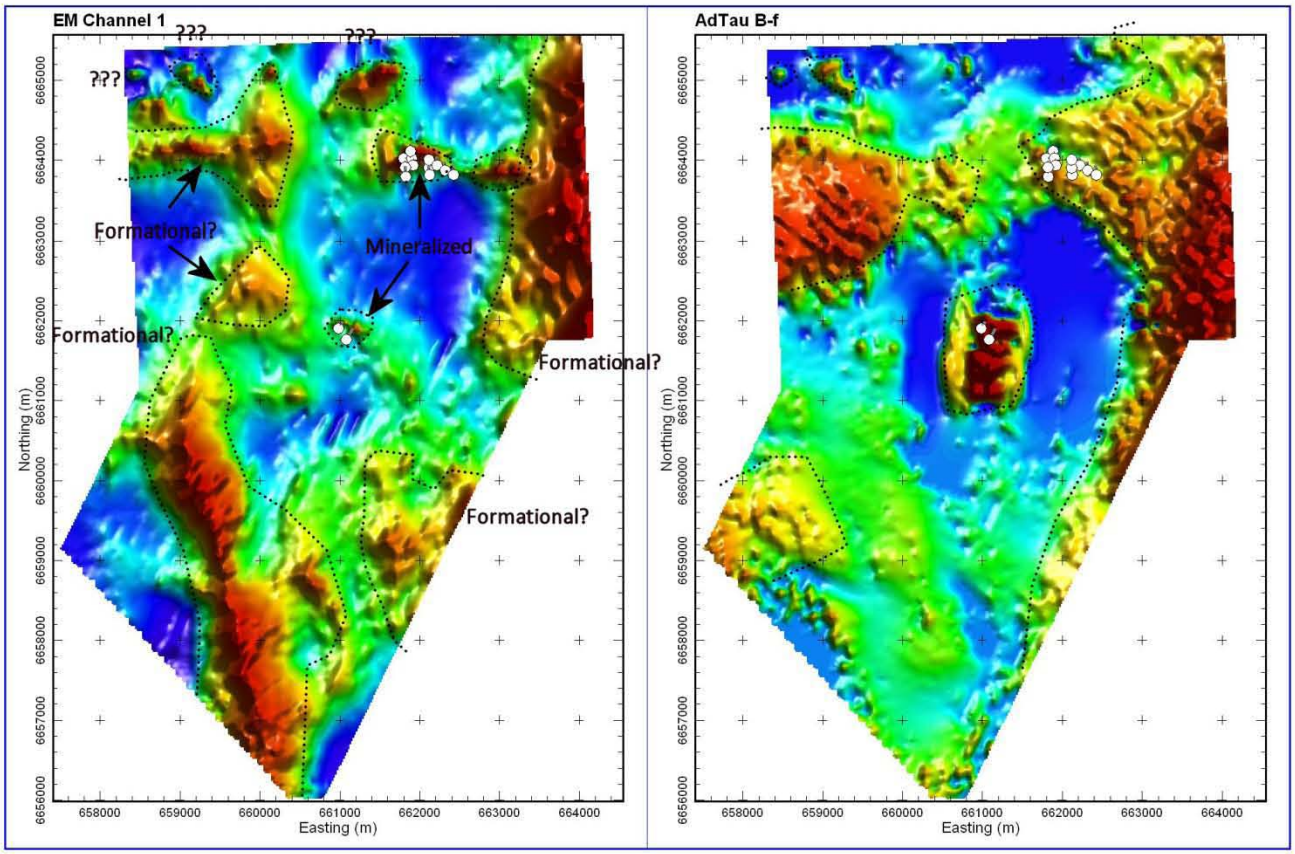


Figure 16: Mor/Mor Extension: EM Channel 1 and AdTau (B-f) with interpretation and drilling (white dots).

Figure 17 shows the same images as in Figure 16 but with the EM picks and Target Zones defined. Tarsis had an earlier assessment performed on the survey by Geotech Ltd. (Bournas 2007) and the labels applied to the zones defined by Bournas were used by Condor where they overlapped. No formal reconciliation between Geotech's and Condor's assessment of the responses has been undertaken.

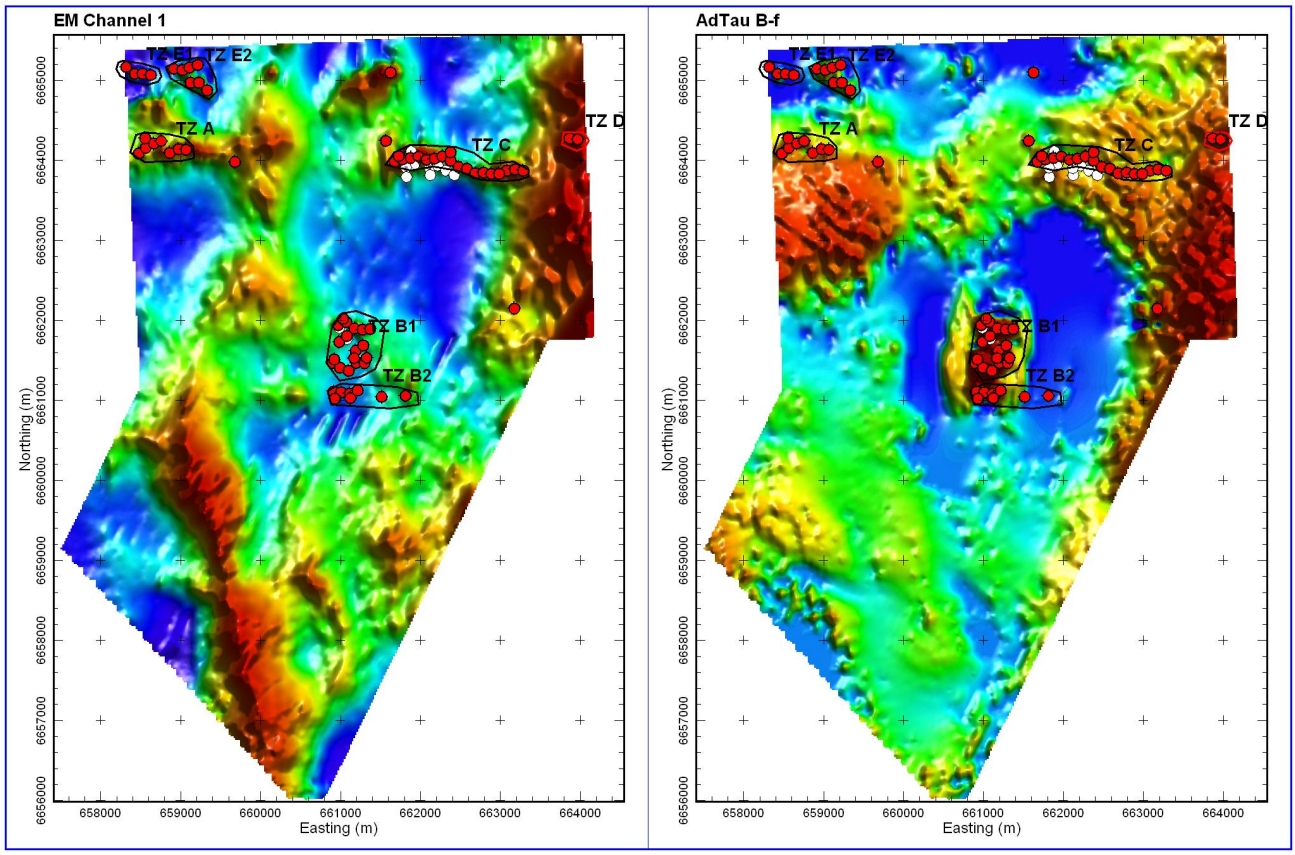


Figure 17: Mor/Mor Extension: EM Channel 1 and AdTau with EM picks (red dots), Target Zones and drilling (white dots).

EM3D

A 3D model of the EM response was created from the 1D inversions along the flight lines; an image of this is shown in Figure 18 and several AVIs and DXFs are provided as well (see Table 3-1). This image suggests there are several different styles of conductivity structure on the property. On the western side of the block, TZ A appears to be at the upper edge of a conductive sheet dipping to the south. TZ B1 and B2 are associated with a discrete "island" of high conductivity that appears disconnected from the other conductivity distributions on the property. TZ C appears as the western extension of a formational type response that extends along the eastern side of the property. TZ D lies over this formational zone. TZ E1 and E2 are isolated features in the far NW corner of the survey block.

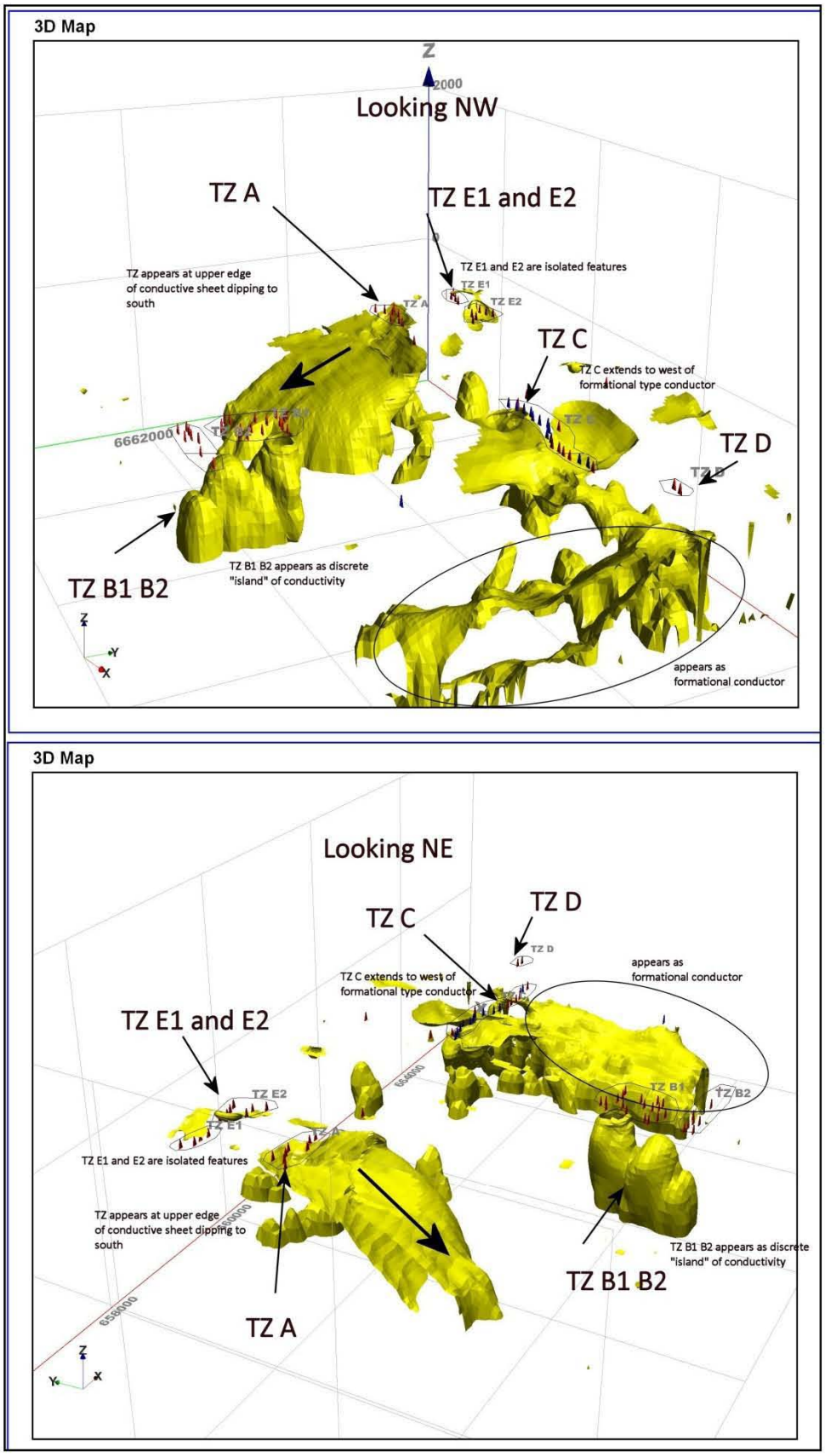


Figure 18: Mor: Views of 3D EM voxel model for Mor showing EM picks and TZs.

TZ

The various TZ are discussed in more detail. For the figures provided, both the Mag3D and EM3D voxel models are displayed.

TZ A: Figure 19: Located in the NW corner of the survey, this is a limited strike length string of discrete EM picks; appears to trend off the survey block to the west. The EM conductivity model shows the TZ to be lying at the upper edge of a southward dipping conductive sheet. The EM Channel 1 response (Figure 17) appears to highlight this upper edge whereas the AdTau appears to be responding more to the depth extent of the horizon. The voxel model and AdTau both suggest this unit is limited spatially to the western side of the survey block. The magnetic results show there are several steeply dipping magnetic highs associated with the overall EM feature. The stronger magnetic response does not appear to correlate directly with the discrete EM picks.

TZ B1 & TZ B2: Figure 20: The EM response appears as a discrete feature that has three distinct sections and these get progressively deeper moving from north to south. There seems to be a shallow magnetic body at the north end of feature with a rod-like protrusion that plunges to the south. A large magnetic source lies just to the west but does not shown any EM response.

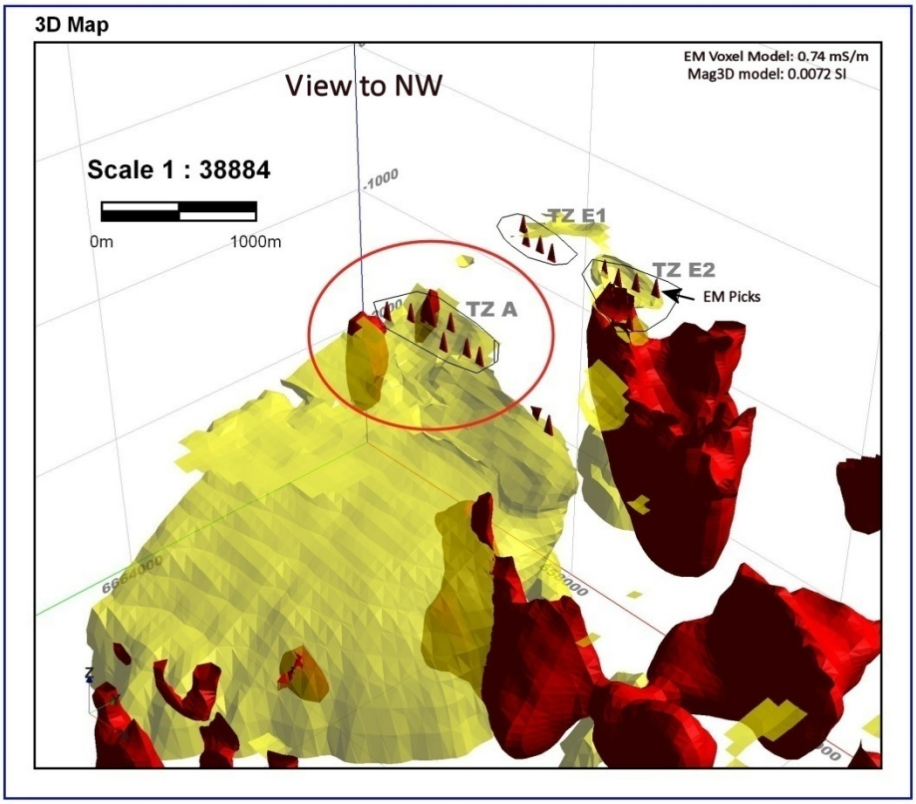


Figure 19: Mor/Mor Extension: TZ A: EM (yellow) and susceptibility (red) models.

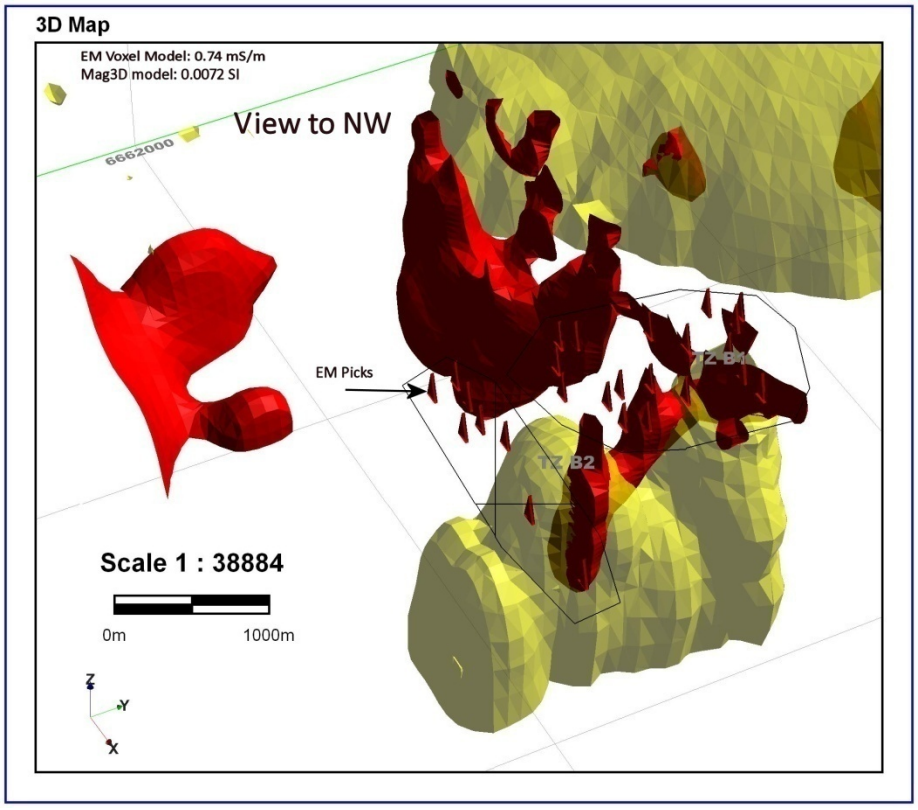


Figure 20: Mor/Mor Extension: TZs B1 and B2; EM (yellow) and susceptibility (red) models.

TZ C: Figures 21 and 22: The EM and magnetic responses in this area are quite complex. The area of known mineralization appears as discrete EM picks but does not image very well in the 3D model. There seems to be a flat-lying EM basement that is dipping off to the east towards the noted formational conductor along the eastern side of the survey block. The magnetic model shows an N-S body that stops at the western end of the TZ and extends to the south. There is another magnetic source at the eastern end of the TZ but at depth; this feature and the other appear to join up to the south and form a larger body. Conductivity appears to infill an embayment made by the magnetic model. Figure 22 provides a view of the models from the north and shows there is a zone of deeper conductivity to the NE of the Discovery Zone.

TZ D: Figure 22: This is a strike limited target with what appears to be coincident EM and magnetic responses.

TZ E1 and E2: Figure 23: There appears to be a modest conductivity zone connecting the two TZ. There also appears to be a significant magnetic body associated with TZ E1.

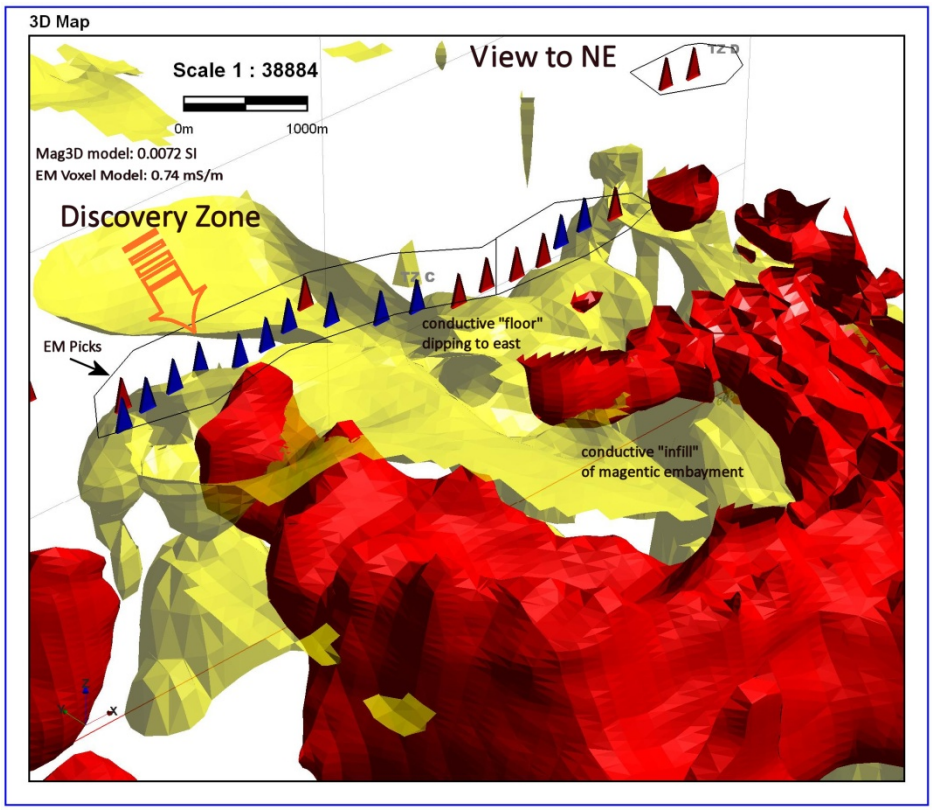


Figure 21: Mor/Mor Extension: TZs C and D; EM (yellow) and susceptibility (red) models.

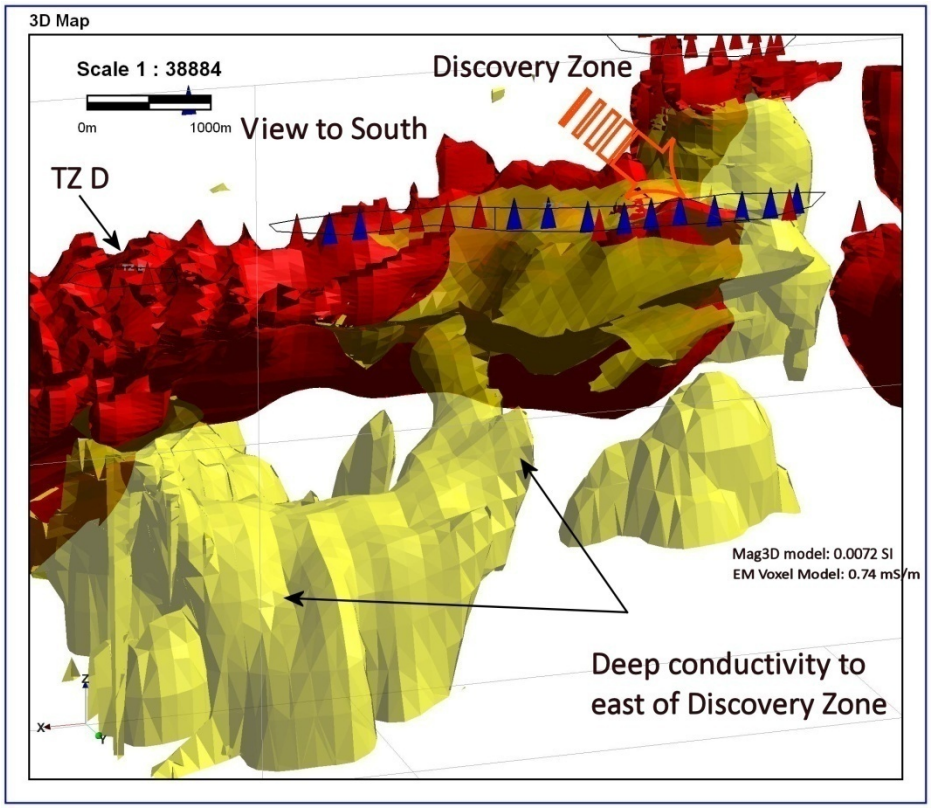


Figure 22: Mor/Mor Extension: TZs C and D; EM (yellow) and susceptibility (red) models.

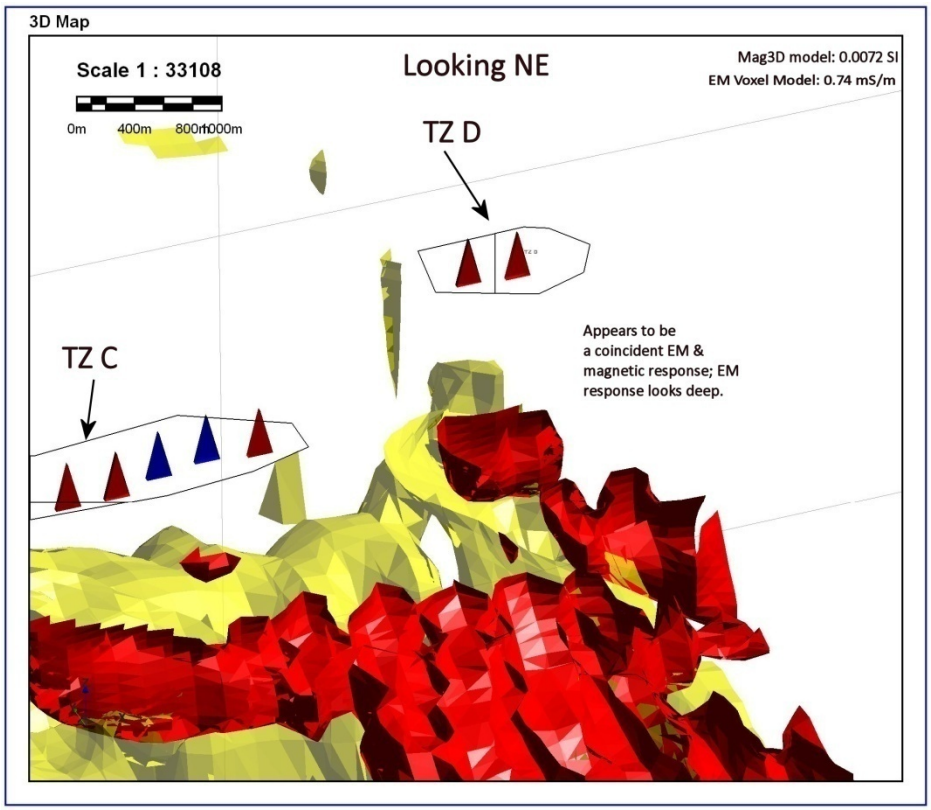


Figure 23: Mor/Mor Extension: TZ D: EM (yellow) and susceptibility (red) models.

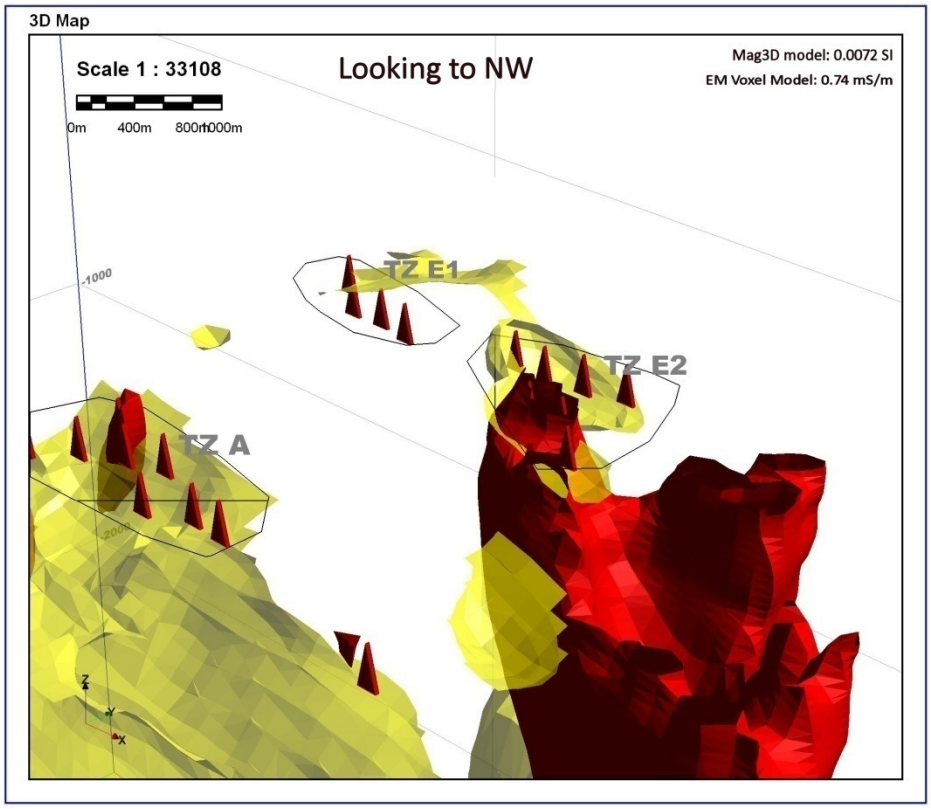


Figure 24: Mor/Mor Extension: TZs E1 and E2; EM (yellow) and susceptibility (red) models.

Cabin Lake

Figure 25 shows the EM Channel 1 and AdTau B-f response with the picking for survey block. Wide Zones were the dormant style of EM response in the survey. A number of discrete picks were selected as well, but these all appeared to represent the edges of Wide Zones rather than discrete bedrock features.

An EM voxel model was created for the survey and Figure 26 shows perspective views of three thresholds with the TZs. There appears to be a complex zone of conductivity at the northern end of the survey block that extends along the eastern margin of the block to the south. The southward extension appears to be mapping out a conductive unit that is steeply dipping along the eastern edge of the block but then dips westward and flattens out at depth. Four TZs have been selected and are discussed below.

TZ 1: Figures 26, 27 and 28: This is a limited strike length feature that lies on the western side of the formational style conductor that extends the full length of the survey in an N-S direction. In Figure 26,

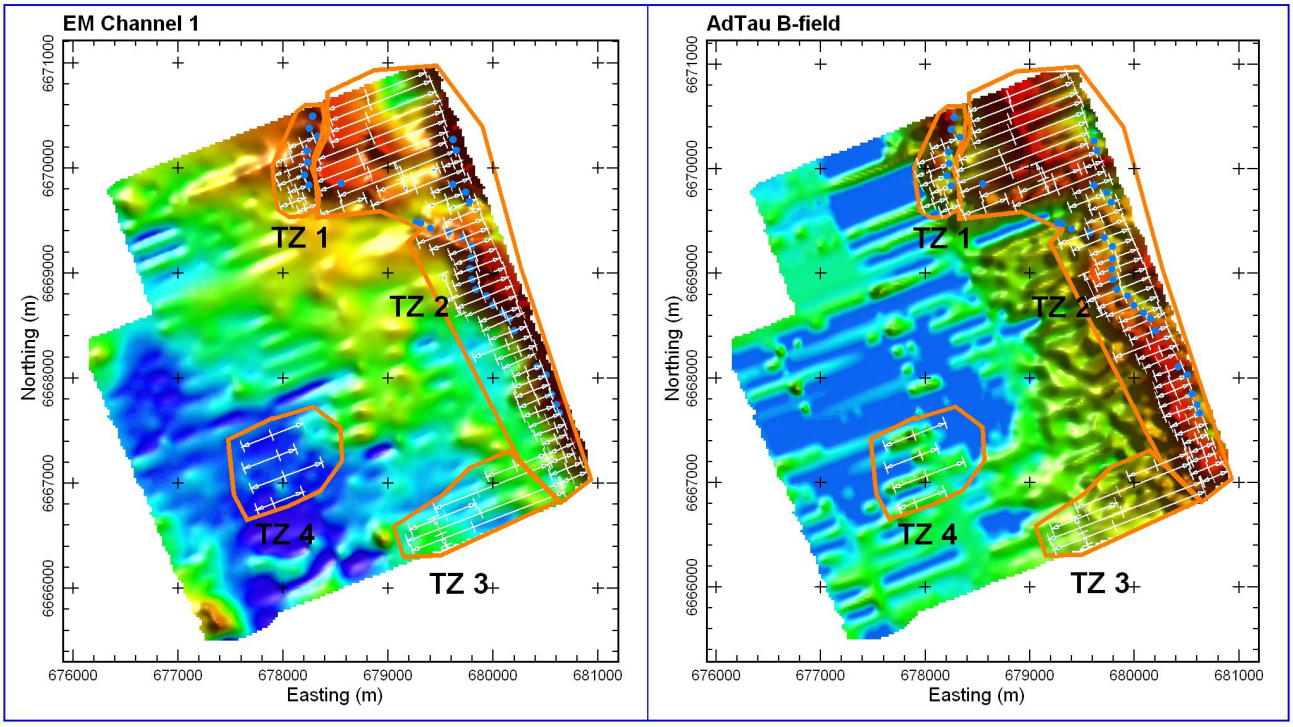


Figure 25: Cabin Lake: EM Channel 1 and AdTau (B-f) with TZs and EM picks.

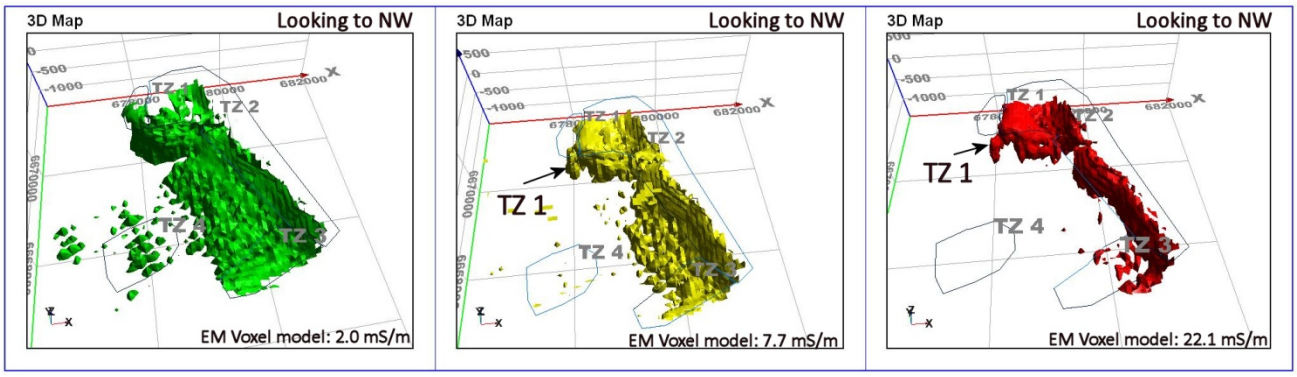


Figure 26: Cabin Lake EM voxel model with three thresholds; 2, 7.7 and 22.1 mS/m with TZ.

its location is highlighted in the central and right hand panels. Figure 27 shows the feature in more detail in the EM voxel model. L8040 passes over the top of this TZ and the geophysical outcomes along this line are shown in Figure 28. Target modeling of this feature is warranted prior to drilling but the depth appears to be the order of several hundred meters.

TZ 2: Figure 29: This zone of conductivity is deemed to be most likely formational and hence not a economic target. However, understanding how it relates to the overall geology of the survey block is deemed important. In Figure 29, two of the conductivity isosurfaces are highlighted in order to better define the Zone's overall character.

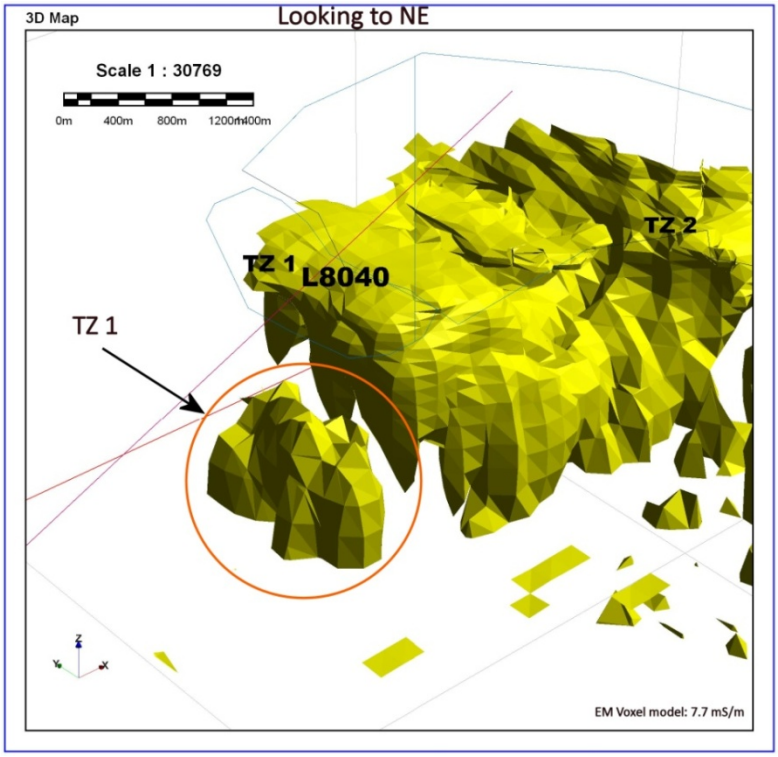


Figure 27: Cabin Lake: EM voxel model showing TZ 1.

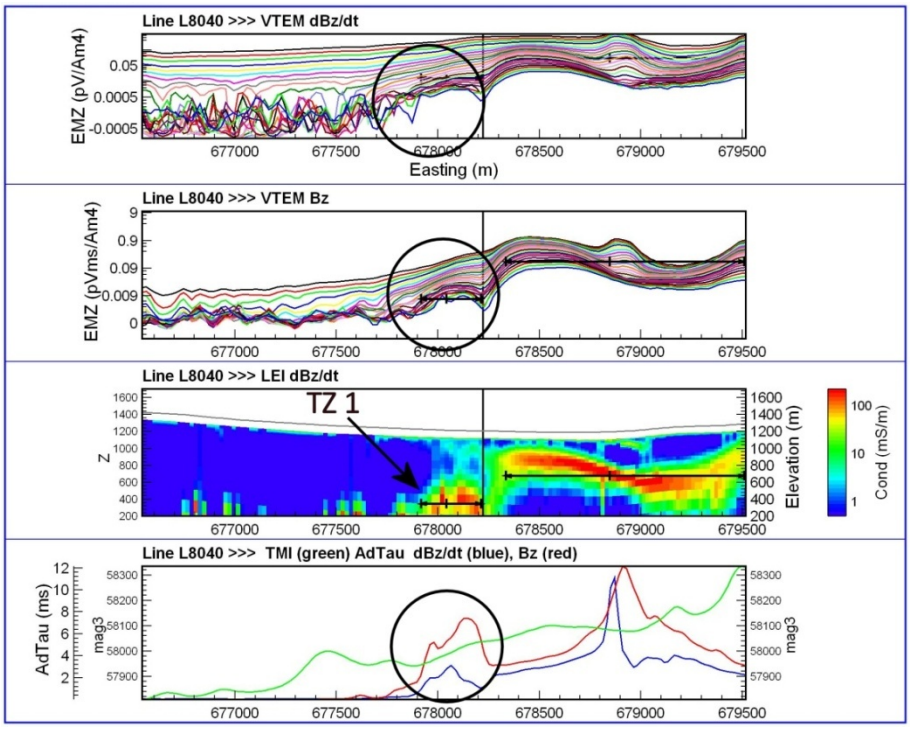


Figure 28: Cabin Lake: MultiPlot for L8040 over TZ 1.

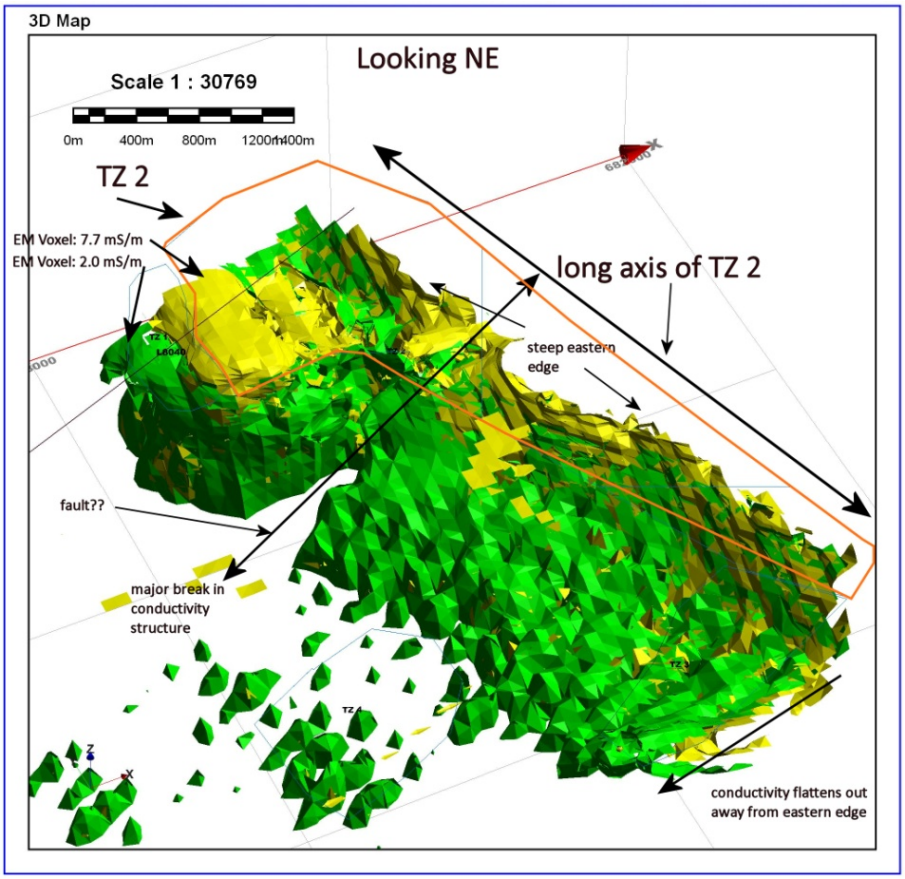


Figure 29: Cabin Lake EM voxel model for TZ 2.

TZ 3: Figure 30: Like TZ 2, this TZ appears to be a formational but represents a major change in the character of the sub-surface conductivity and hence is deemed worthy of taking note of. This TZ is not deemed to be of economic interest based on current information.

TZ 4: Figures 12, 25 and 26: This TZ is a weak change in the EM character that could represent some effect of an intrusive event located in the SW corner of the property as best expressed in Figure 12. The EM character is deemed marginal at best and follow-up using the IP technique is recommended if this TZ were to be further investigated.

Caribou

The EM Channel 1 and AdTau response is shown in Figure 31. Indicated as well is the one EM pick indentified on this block. Figure 32 shows the MultiPlot over this feature. An EM voxel model was created for this block but showed no character of either a discrete target or geological mapping interest. The single pick (contained within TZ 1) is deemed to be a reliable target and given its location on the northern edge of the survey block, could extend off the grid.

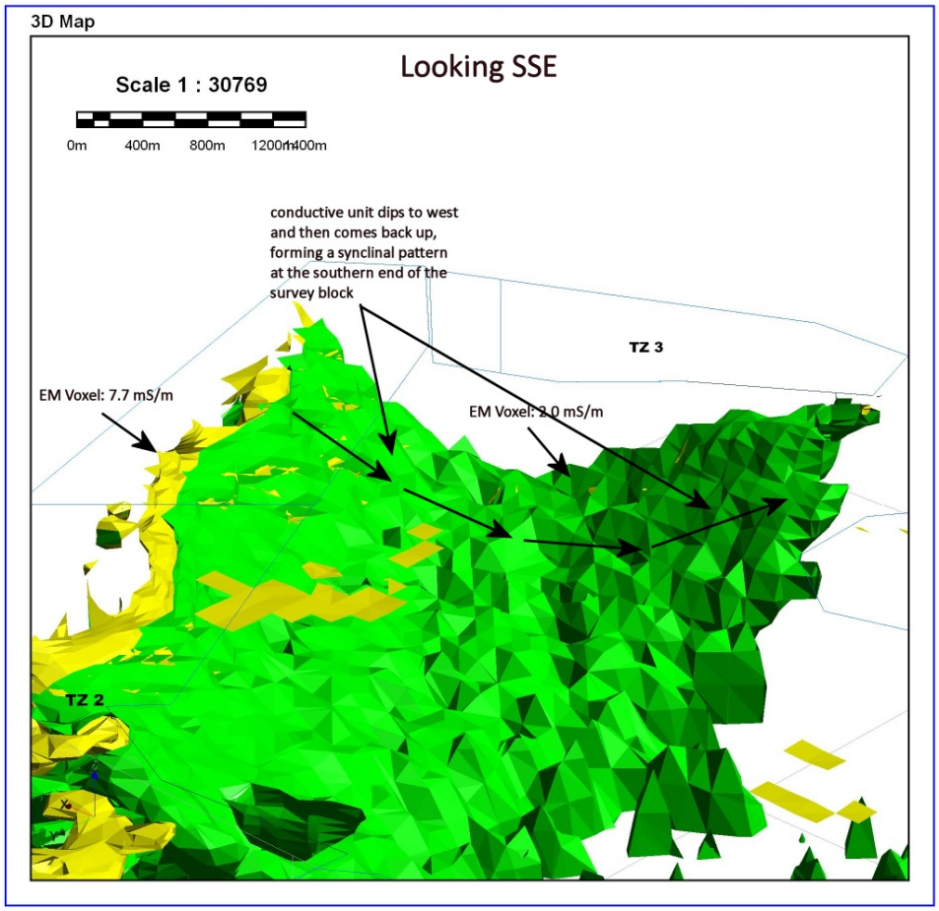


Figure 30: Cabin Lake EM voxel model for TZ 3.

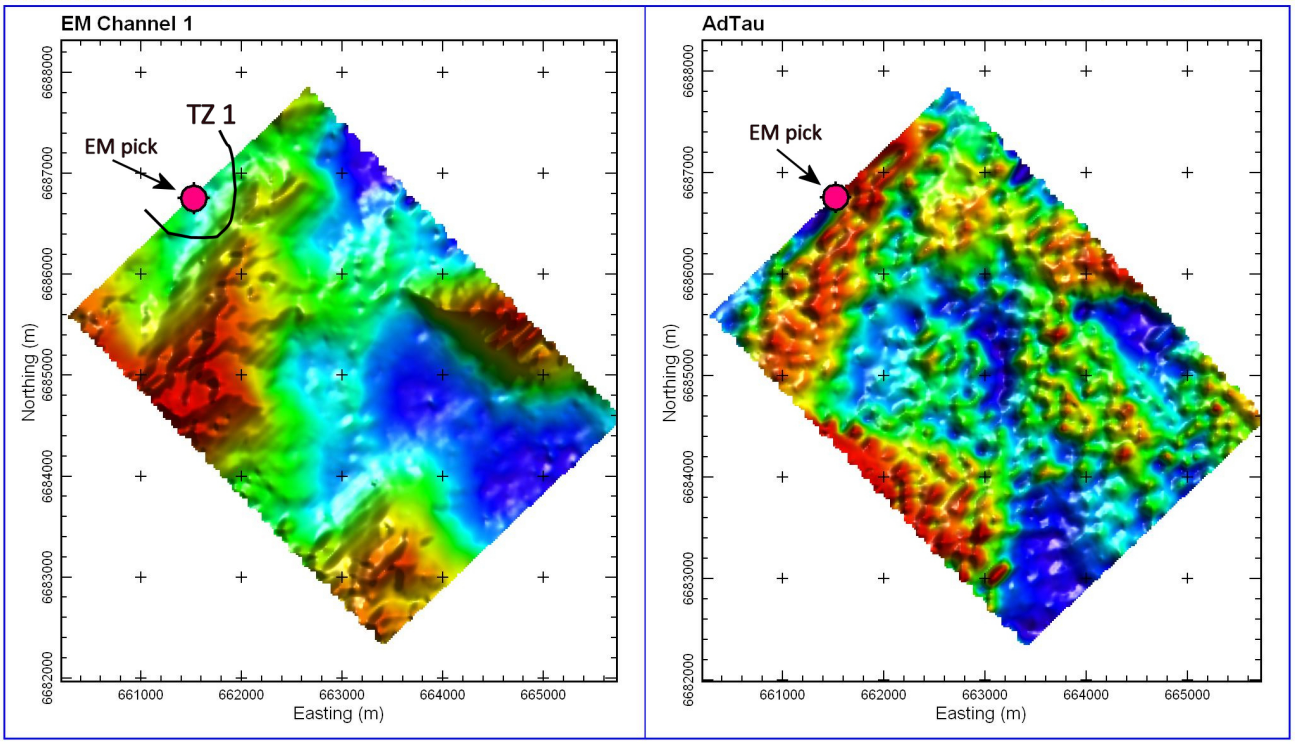


Figure 31: Caribou EM Channel 1 and AdTau showing EM pick.

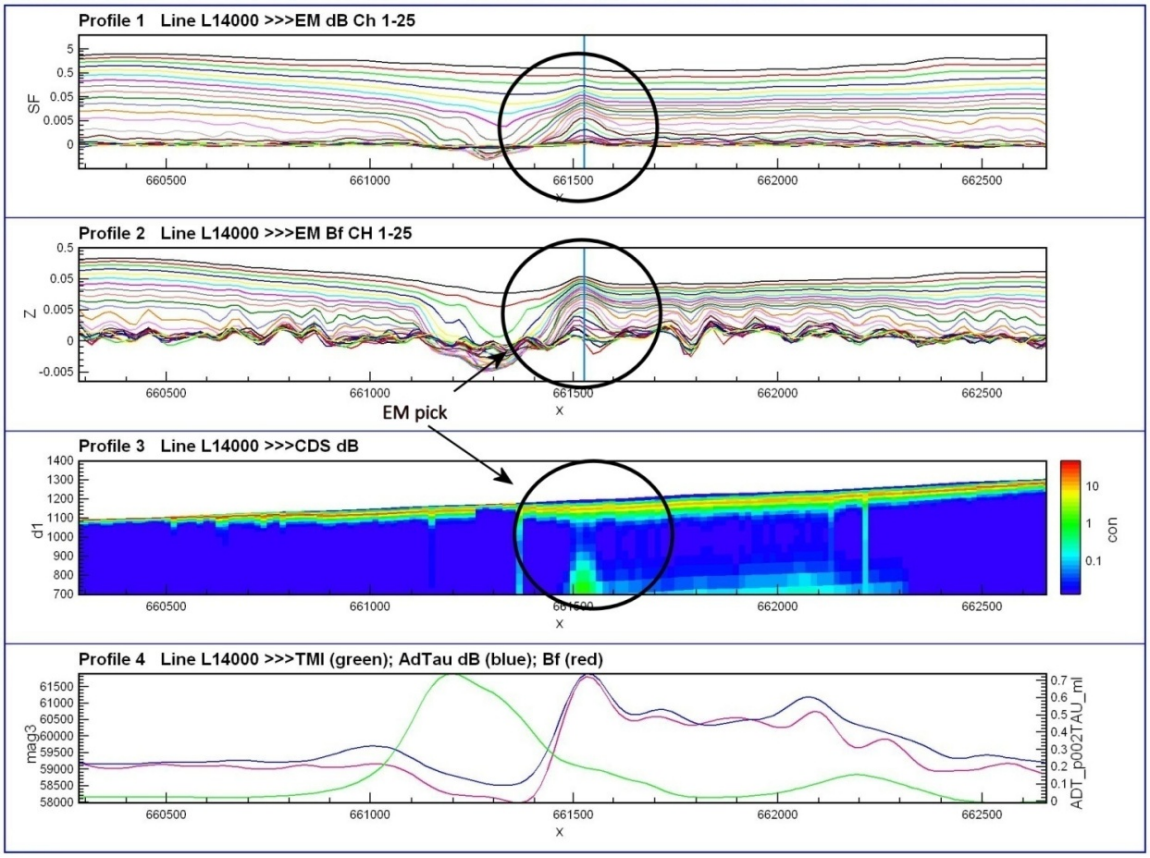


Figure 32: Caribou; MultiPlot L14000 showing EM pick

Discussion

Mor

The Mor assessment shows several untested targets of interest as well as potential extensions to the two known zones of mineralization. These outcomes are summarized below.

TZ A: Appears to be the upper edge of a formation conductor dipping to the south. Minor magnetic response. Low priority

TZ B1 and B2: Corresponds to what is termed the MSB Zone of mineralization. Geophysical modeling suggests extensions of this zone to depth to the south of the known mineralization. High priority

TZ C: Corresponds to the Discovery Zone. Geophysical modeling suggests there could be extensions to this zone both to the east and NE at depth. High priority

TZ D: Strike limited zone in interesting area. Medium priority

TZ E1 and E2: Shows interesting EM and magnetic character especially on the eastern side of the TZ. Medium-high priority.

Cabin Lake

TZ 1: This feature is deemed worthy of further assessment. High priority

TZ 2: Formational conductor. Low priority

TZ 3: Formational conductor. Low priority

TZ 4: Possible alteration halo to intrusive. Low-medium priority

Caribou

One conductor indentified. Medium priority (additional geophysical or geochemical work recommended to investigate area. Staking to extend claim coverage is also recommended.

.

5. CONCLUSIONS & RECOMMENDATIONS

This report provides an assessment of a VTEM EM and magnetics survey over three properties in the southern Yukon held by Tarsis Capital Corp. The primary economic focus was on VMS style targets.

The Mor property appears to hold the greatest potential for further discovery given the presence of significant mineralization in several locations on the property, both of which show strong geophysical responses and appear to offer potential for extensions to know mineralization. Several other zones of interest were recognized as well.

The Cabin Lake property has one target of interest; however, this target is apparently several hundred meters depth below surface and this could preclude early stage testing unless the target can be upgraded with mapping or possibly geochemical surveying.

The Caribou property survey produced one reasonable bedrock EM response on the edge of the flight block. Follow-up mapping and geochemical work is recommended, with consideration to extend the claim block to the north to cover possible extensions to the conductive zone.

Respectfully submitted



Condor Consulting, Inc.

February 4, 2009

6. REFERENCES

Bournas, N. 2007 Report on a Helicopter-Borne Time Domain Electromagnetic Geophysical Interpretation Mor Property Yukon Territory, Canada for Tarsis Capital Corp., Geotech Ltd., December 2007

Downie, C., 2007, Technical Report for the Morley River Property MOR 1 – 52 CLAIMS, for Almaden Minerals Ltd. and Tarsis Capital Corp. January 2007.

Ellis, R. G., 1998a Inversion of airborne electromagnetic data: Explor Geoph Vol 29, pp 121-127.

Farquharson, C.G. and Oldenburg, D. W., 1993, Inversion of time domain EM data for a horizontally layered earth, Geophysical Journal International, Vol. 114, pp 433-441.

Holroyd, B. and Lajoie, J. and Klein, J. 1997 Geophysical Aspects of the Kudz Ze Kayah Massive Sulphide Discovery Southeast Yukon, Canada in "Proceedings of Exploration 97: Fourth Decennial International Conference on Mineral Exploration" *edited by* A.G. Gubins, 1997, p. 1053–1056

Lev, G., 2007, Report on a Helicopter-Borne Versatile Time Domain Electromagnetic (VTEM) Geophysical Survey, Cabin Lake property Yukon, Canada for Tarsis Capital Corp.; Geotech Ltd. November 2007

Lev, G., 2008, Report on a Helicopter-Borne Versatile Time Domain Electromagnetic (VTEM) Geophysical Survey, MOR property Yukon, Canada for Tarsis Capital Corp.; Geotech Ltd. January 2008

Li, Y., and D. W. Oldenburg, 1996, 3-D inversion of magnetic data: Geophysics, **61**, no.2, 394-408.

Orlowski, K., Fiset, N. and Legault, J., 2008, Report on a Helicopter-Borne Versatile Time Domain Electromagnetic (VTEM) Geophysical Survey, Caribou Property, Yukon Canada for Archer Cathro & Associates; Geotech Ltd., November 2008

Orlowski, K., Fiset, N. and Legault, J., 2009, Report on a Helicopter-Borne Versatile Time Domain Electromagnetic (VTEM) Geophysical Survey, Mor Property, Yukon Canada for Archer Cathro & Associates; Geotech Ltd., January 2009

Power, M., 2004, Induced Polarization Survey at the Mor Property, Teslin Area Yukon Territory by Aurora Geoscience Ltd. October 2004

Shi, Z and Butt, G. 2004 New enhancement filters for geological mapping, Preview, 111, 87-88, (2004)

Tarsis Web site: www.tarsis.ca

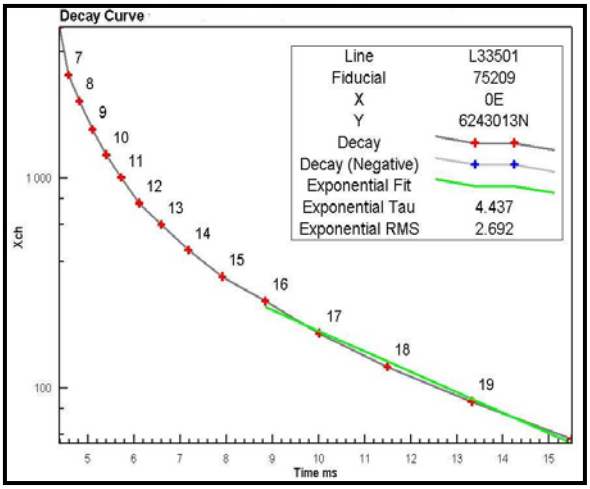
7. APPENDICES

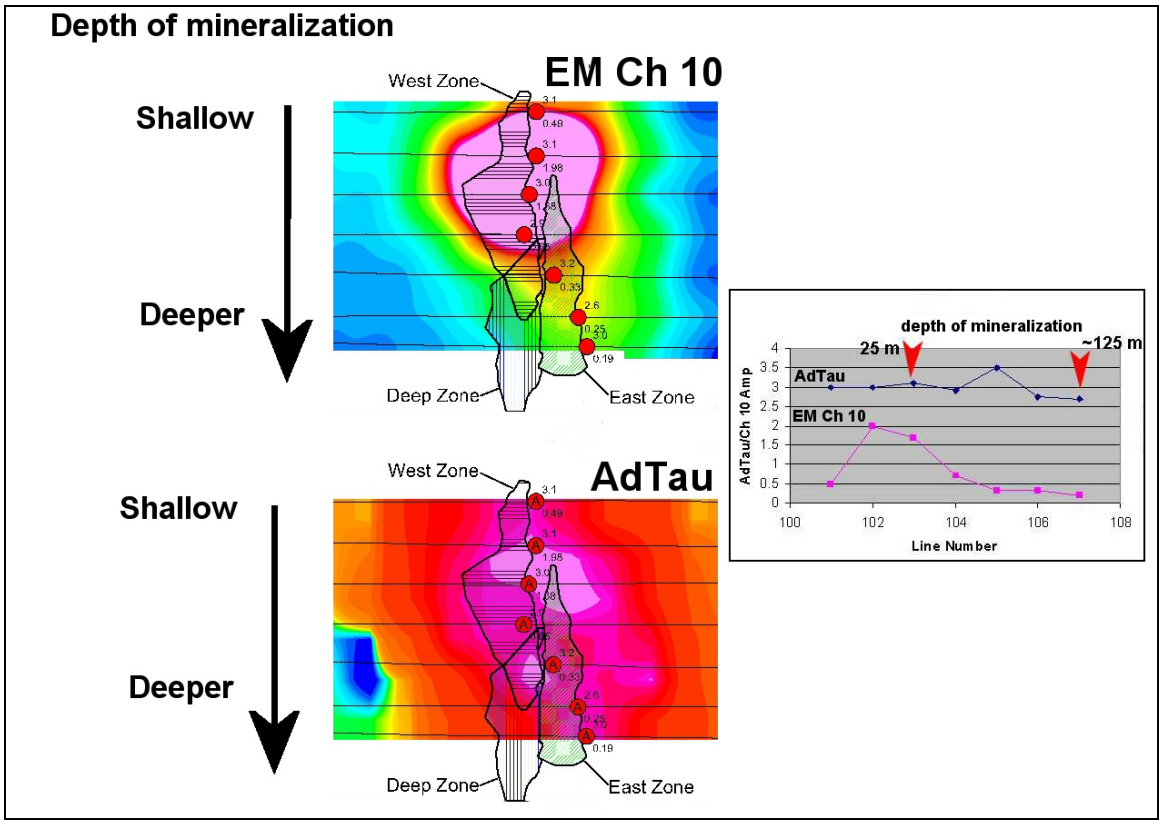
APPENDIX A: BACKGROUND ON EM PROCESSING

Time Constant Analysis
AdTau

Condor Consulting, Inc.

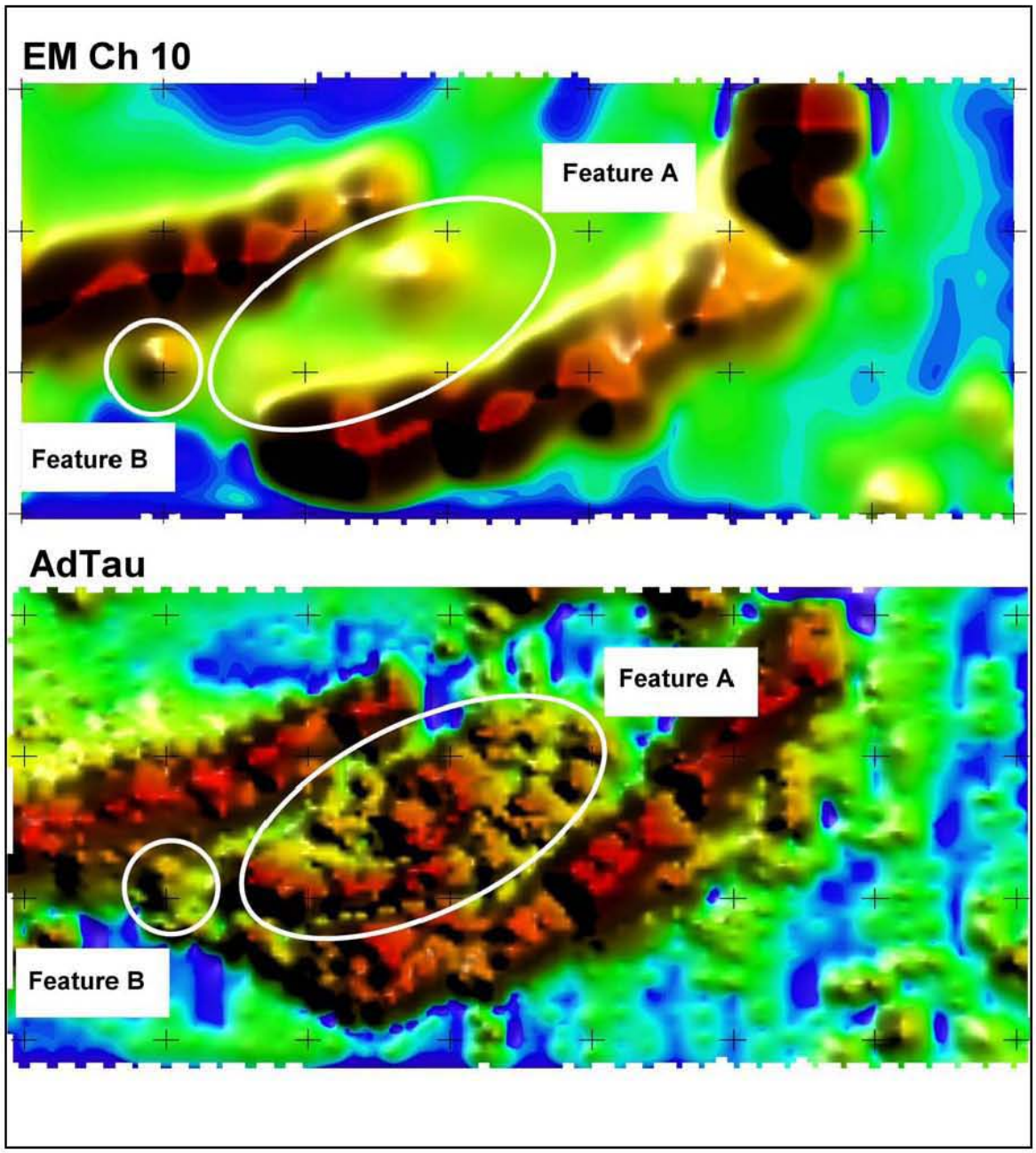
The AdTau program calculates the time constant (tau) from time domain decay data. The program is termed ***AdT***au since rather than using a fixed suite of channels as commonly done, the user sets a noise level and depending on the local characteristics of the data, the program will then select the set of last five channels that are above this noise level. In resistive areas, the earlier channels will tend to be used (i.e. little late time response), whereas in conductive terrains the latest channels available can generally be used. A typical decay fit is shown on the right; the fitted late-time response is shown as the green line.





In the figure above, the upper image shows the EM amplitude plot over the Montcalm Cu-Ni Deposit and the corresponding AdTau image is underneath. From extensive drilling it is known that the deposit is shallow at the northern end (top of image) and deeper at the south. The profiles in the insert box on the right show the responses along the axis of the deposit, highlighting that the EM amplitude response is strongly affected by the depth of mineralization whereas the AdTau response is much less sensitive to depth.

The image below from the Ferguson Lake deposit (East Zone) shows another example of the benefits of examining time constant over simple EM amplitudes. The upper image is that of early time EM data; two zones are highlighted. Feature A is a large area of response with a few modest isolated highs that are bracketed by two strong linear trends. Feature B is a discrete source with what appears to be a moderately high response The AdTau image shows Feature A to be strongly conductive and made up of a number of discrete sources. Feature B on the other hand is not particularly conductive compared to other sources in the area.

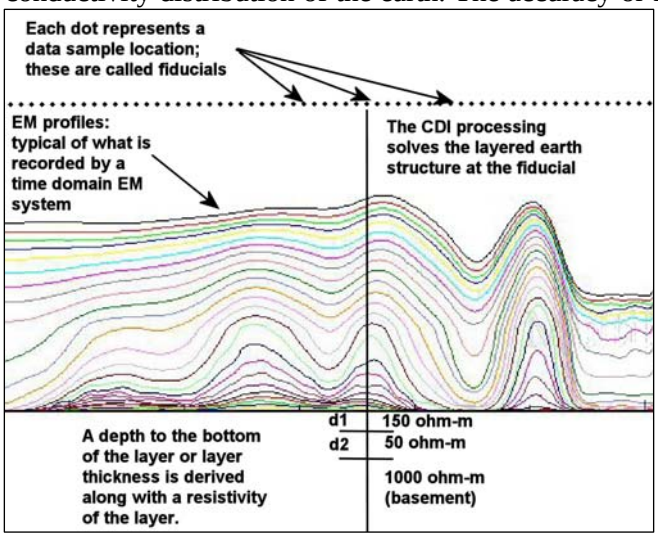


The assessment of airborne EM data requires both the proper tools and prerequisite understanding of how the tools respond in a variety of situations. For additional information the EM character of a range of deposit styles, contact Condor Consulting at www.condorconsult.com.

Conductivity Depth Imaging
Introduction

Condor Consulting, Inc.

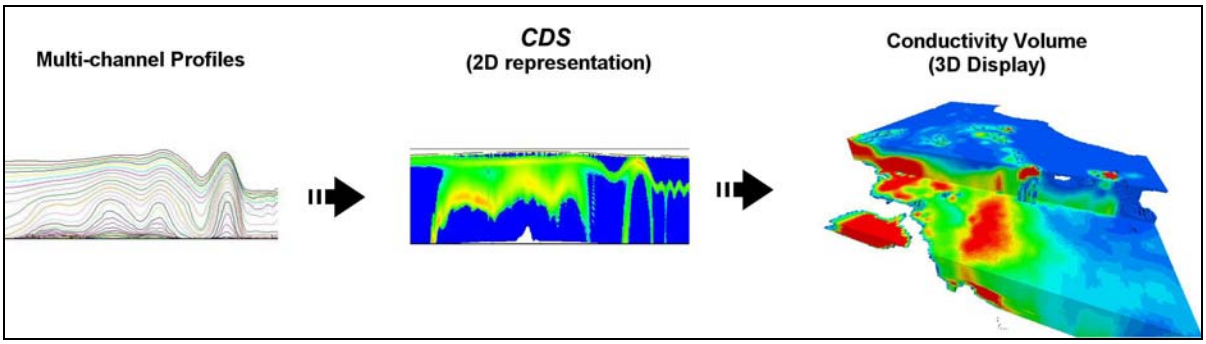
Conductivity Depth Imaging or CDI of airborne EM (AEM) data is the term applied to the mathematical transformation of the EM response recorded in the measuring instrument of the survey aircraft that is the transformed into a conductivity distribution of the earth. The accuracy or resolution of the outcomes of CDI is dependent on a number of factors including the type of EM system employed, the quality of the data the system produces, the terrain covered by the system and methodology of the CDI approach. Basically all CDI approaches in commercial use involve what is termed a 1D approximation of the earth. This means that the mathematical model being fit to the data can only capture changes in conductivity vertically in the earth. Displays of CDI outcomes in 2D (sections along lines) and 3D (gridding between lines) all rely on outcomes that are derived from initial 1D processing.



Imaging vs. Inversion: CDI processing can in turn be broken down into two major approaches in the mathematical process involved in solving the sub-surface conductivity structure; this being what is termed either imaging or inversion methodology. Both approaches are in use by survey contractor and consultants and each technique has advantages and draw backs depending on two primary factors; the EM system which acquired the data and the geological problem. Condor uses both approaches but prefers the inversion approach in most applications.

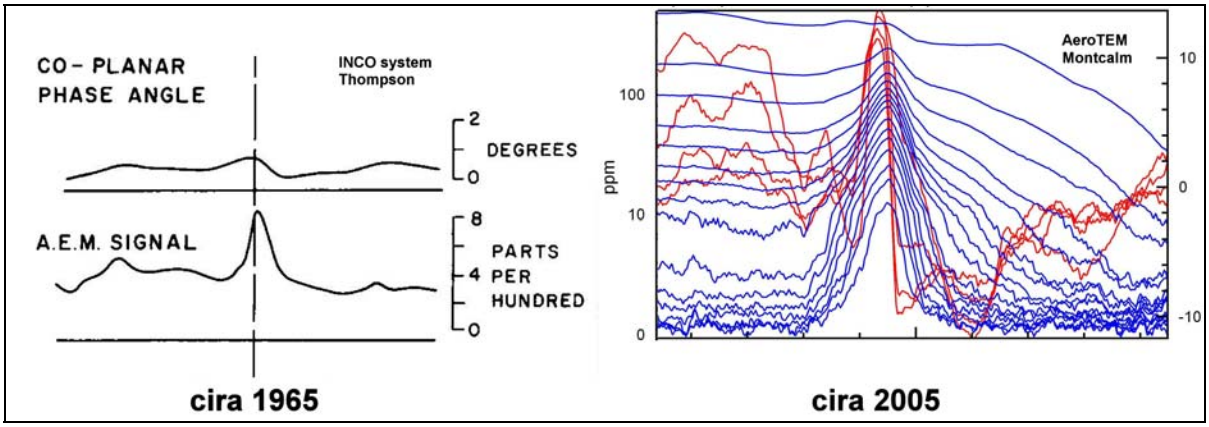
Off-time vs. Bfield: A derived Bfield outcome is now commonly delivered by the major contractors along with the traditional pure off-time data. Condor will routinely process both data streams and then assess which provides the superior outcome for subsequent use specific project assessment. Condor has found this dual processing approach is required as it is very difficult before hand to assess what data stream will provide the best outcome.

In the next several pages, examples of CDI processing will be presented which illustrate the role it can play in modern AEM interpretation. The color section showing a CDI is termed a Conductivity Depth Section or CDS.

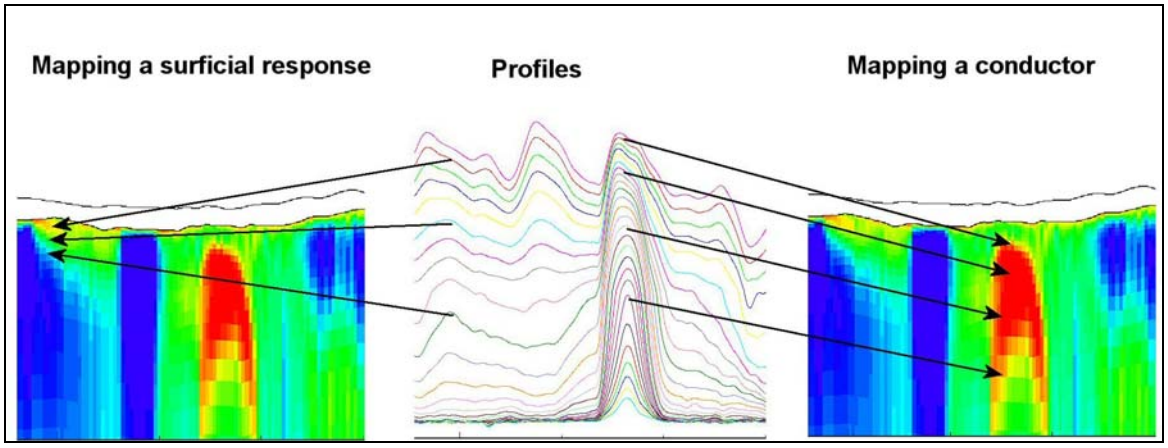


Historically, AEM was used primarily for fairly simple detect of discrete high conductance features which could represent deposits of massive sulfides such as VMS or Ni-Cu. There was little interest in extracting more information other than the X, Y location of the feature and some basic idea of the quality of the conductor. Ground follow-up for location validation and drill hole spotting was always done.

In modern exploration however, there is a far greater range of targets being sought after and in a much wider variety of settings. Even in traditional areas where AEM has been used are now deemed 'mature' explorers are expecting that more sophisticated acquisition and processing techniques will be required to make new discoveries.

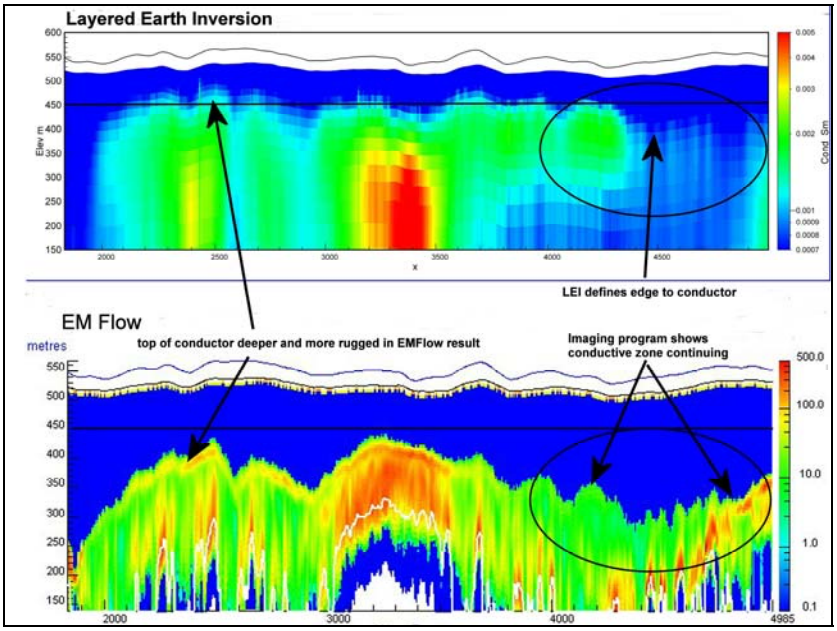


In the CDI process (this applies to either imaging or inversion approaches), those elements of the geology that are dominantly horizontal in nature can be modeled quite well whereas narrow steeply dipping features most often appear with a 'comet-like' shape the depth of which does not necessarily correspond all that well to the actual depth within earth. While this may seem like a major draw back to using these outcomes, a combination of experience, local calibration and access to alternate means to model the data allow the seasoned interpreter to define the subsurface geology quite well. The CDI processing at its best is a very useful means to provide a 3D conductivity "context" of the subsurface which can be extremely valuable in helping to recognize and define zones of interest.



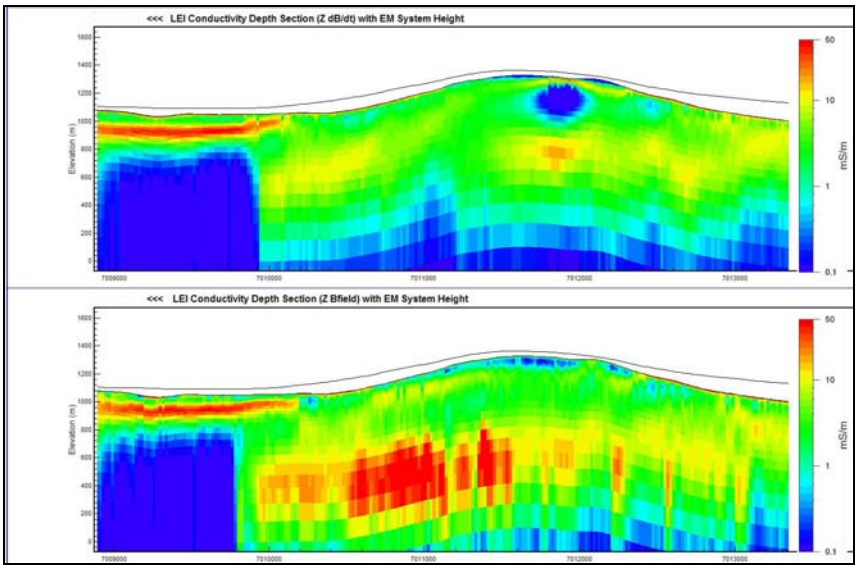
Differences between Imaging and Inversion

The image below shows the outcomes of an inversion program (termed Layered Earth Inversion or LEI) and a imaging program, in this case EMFlow. Three major differences are noted in this example (VTEM survey in the Athabasca Basin); first the depth to the major conductive zone appears deeper in the EMFlow outcome, second the topology of the basement conductor appears to be more rugged in the EMFlow outcome and third, the conductive horizon appears to end in the LEI outcome on the right hand side whereas the EMFlow result shows the zone continuing off the right and side of the image.



Differences between dB/dT and Bfield

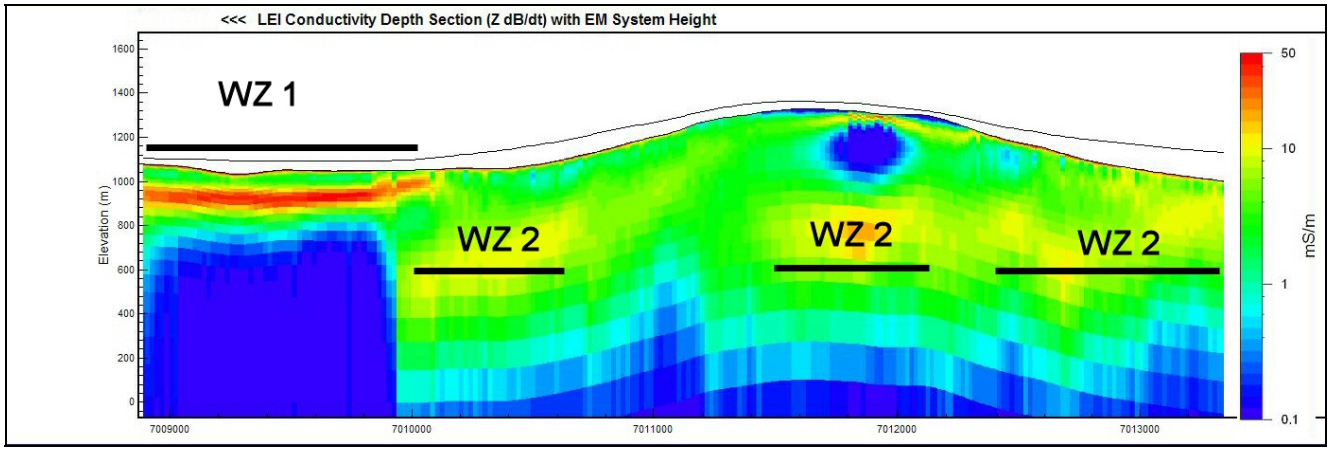
The figure below shows the outcomes of LEI processing to the dB/dT and Bfield outcomes from a VTEM survey undertaken as part of a Ni-Cu search. These results are considered typical in that while the Bfield result shows a nominal greater sensitivity to higher conductance, the results are also somewhat nosier and appear to have slightly less high frequency content than the dB/dT results.

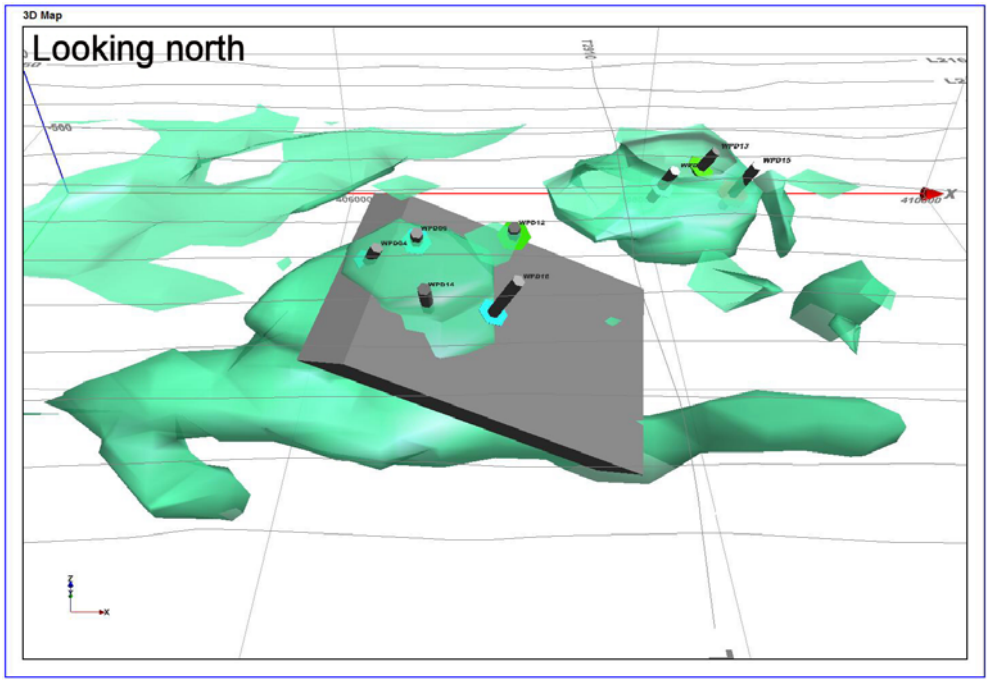


How CDI Helps Interpretation?

A major benefit of having a CDI outcome to interpret is that it coveys a far more geological "feel" to the EM data than profiles along. This is sometimes termed "mapping" with target detection and discrimination a sub-set of this larger interpretive activity.

Using the previous image as an example, the dB/dT CDS has been annotated with what Condor terms Wide Zones. These are zones of broad conductivity in the CDS which are felt to characterize different parts of the geological section. In this case WZ-1 is a thin shallow near surface that could represent lake sediments or a in a weathered terrain, part of a distinctive weather profile over a mafic rock. The WZ-2 features are "in the earth" sources that represent zones of increased conductivity which could represent different rock units or alteration of a specific unit.





Another benefit of the CDI processing is that it in turn allows for the creation of 3D voxel models of the EM outcomes. This is often an excellent means to capture in a holistic sense the sub-surface conductivity distribution either as a stand-alone model or as part of the integrated geoscience model (referred to as a Common Earth Model). An example of such a conductivity model combined with parametric models of specific anomalies (produced using Maxwell) and drill holes is shown in the figure to the left.

	A	B
1	Depth (M)	Layer
2	5	1
3	11	2
4	17	3
5	25	4
6	34	5
7	44	6
8	55	7
9	68	8
10	83	9
11	101	10
12	120	11
13	143	12
14	169	13
15	199	14
16	234	15
17	273	16
18	319	17
19	371	18
20	431	19
21	500	20
22	580	21
23	673	22
24	783	23
25	909	24
26	1056	25
27	1228	26
28	1426	27
29	1658	28

APPENDIX B: ANOMALY LISTING

MOR

X	Y	Line Number	FID	Line	Type	CID	ADT_BFp01TAU_lp	ADT_SFp01TAU_lp
661327	6661533	T5945	36827	5945	SPR	C	0.0	0.1
658624	6665066	L4830	9275	4830	SPR	A	0.0	0.0
658319	6665166	L4800	53102	4800	SPR	A	0.0	0.1
661515	6661043	L5100	9751	5100	SPR	A	0.0	0.1
661812	6661058	T5950	21378	5950	SPR	C	0.0	0.0
658915	6665144	L4860	18004	4860	SPR	B	0.0	0.1
661626	6665100	L5130	59780	5130	SPR	B	0.0	0.1
661976	6664049	L5160	50792	5160	DPR	A	0.1	0.1
663286	6663873	L5290	6489	5290	SPR	A	0.1	0.1
662076	6664010	L5170	48489	5170	DPR	A	0.1	0.1
662479	6663916	L5210	34762	5210	DPR	A	0.1	0.1
663186	6663889	L5280	66843	5280	DPR	A	0.1	0.1
662176	6664021	L5180	45066	5180	DPR	A	0.1	0.1
661122	6661028	T5950	21084	5950	SPR	B	0.1	0.1
661878	6664032	L5150	54096	5150	DPR	A	0.1	0.2
662274	6664050	L5190	42833	5190	DPR	A	0.1	0.1
663082	6663870	L5270	65016	5270	DPR	A	0.1	0.1
660929	6661023	T5950	21014	5950	SPR	A	0.1	0.1
662375	6664102	L5200	36953	5200	SPR	A	0.1	0.1
662377	6663998	L5200	36995	5200	DPR	B	0.1	0.1
658522	6665085	L4820	8358	4820	SPR	C	0.1	0.2
662584	6663894	L5220	32256	5220	DPR	A	0.1	0.2
658425	6665082	L4810	53816	4810	SPR	A	0.2	0.2
661566	6664245	L5120	61383	5120	SPR	A	0.2	0.2
662985	6663834	L5260	63021	5260	SPR	A	0.2	0.3
658973	6664143	L4860	17514	4860	SPR	A	0.2	0.3
658554	6664279	L4820	8001	4820	SPR	B	0.2	0.3
661776	6664015	L5140	56182	5140	DPR	A	0.2	0.4
658863	6664096	L4850	14322	4850	SPR	A	0.2	0.3
661676	6663985	L5130	59423	5130	DPR	A	0.2	0.3
658664	6664210	L4830	9548	4830	SPR	B	0.2	0.3
662887	6663832	L5250	61047	5250	SPR	A	0.2	0.3
659066	6664136	L4870	22610	4870	SPR	B	0.3	0.3
661299	6661468	L5080	14490	5080	SPR	C	0.3	0.2
659678	6663979	L4930	36687	4930	SPR	A	0.3	0.3
661728	6664055	T5920	27510	5920	SPR	A	0.4	0.4
659020	6665131	L4870	22274	4870	SPR	A	0.4	0.4
658563	6664159	L4820	7945	4820	SPR	A	0.4	0.5
658473	6664087	L4810	54152	4810	SPR	B	0.4	0.5
662791	6663848	L5240	58856	5240	SPR	A	0.5	0.5
662685	6663841	L5230	16023	5230	SPR	A	0.5	0.5
663867	6664276	L5350	21553	5350	SPR	A	0.6	0.8
661282	6661688	L5080	14406	5080	SPR	B	0.7	0.3
663964	6664263	L5360	23177	5360	SPR	A	0.8	0.9

661211	6661123	L5070	18361	5070	SPR	A	0.8	0.4
658757	6664241	L4840	12719	4840	SPR	A	0.8	0.3
661372	6661895	L5090	11018	5090	SPR	A	1.0	0.6
661009	6661101	L5050	23625	5050	SPR	A	1.6	0.2
660972	6661938	L5050	23926	5050	SPR	D	1.6	0.9
661197	6661470	L5070	18480	5070	SPR	B	1.6	0.9
661169	6661527	T5945	36778	5945	SPR	B	2.0	0.7
661071	6661981	L5060	22211	5060	SPR	A	2.0	0.8
661032	6662020	T5940	23632	5940	SPR	A	2.1	1.3
660983	6661731	L5050	23849	5050	SPR	C	2.2	0.9
661186	6661621	L5070	18543	5070	SPR	C	2.2	0.5
661115	6661087	L5060	22568	5060	SPR	D	2.7	0.3
661278	6661884	L5080	14336	5080	SPR	A	2.8	1.3
661081	6661805	L5060	22281	5060	SPR	B	3.2	1.5
660913	6661109	L5040	27944	5040	SPR	B	4.0	0.4
660993	6661409	L5050	23737	5050	SPR	B	4.0	1.2
661175	6661898	L5070	18648	5070	SPR	D	4.8	3.2
660921	6661513	T5945	36687	5945	SPR	A	5.2	1.4
660899	6661468	L5040	27783	5040	SPR	A	5.3	1.4
661102	6661371	L5060	22456	5060	SPR	C	5.4	2.6

CABIN LAKE

X	Y	Line Number	FID	Type	Line
679715.9	6669339	L8160	1442	SPR	8160
679793.7	6669259	L8170	77	SPR	8170
679791.8	6669144	L8180	1442	SPR	8180
679784.4	6669040	L8190	112	SPR	8190
679800.2	6668939	L8200	1400	SPR	8200
679836.4	6668845	L8210	105	SPR	8210
679939.6	6668784	L8220	1512	SPR	8220
679997.9	6668693	L8230	77	SPR	8230
680091.9	6668619	L8240	1575	SPR	8240
680155.8	6668565	L8250	49	SPR	8250
680202.8	6668452	L8260	1645	SPR	8260
680420.3	6668107	L8300	1575	SPR	8300
680505.1	6668031	L8310	7	SPR	8310
680555.3	6667845	L8330	14	SPR	8330
680601	6667745	L8340	1610	SPR	8340
680629.1	6667667	L8350	14	SPR	8350
679309.1	6669474	T8530	1029	SPR	8530
679574.9	6669391	L8150	189	DPR	8150
679401.2	6669428	L8140	1344	DPR	8140
679263.6	6669480	L8130	287	DPR	8130
679778.3	6669682	L8130	42	DPR	8130
679740.3	6669770	L8120	1225	DPR	8120
679616.9	6669842	L8110	84	DPR	8110
679647.5	6670168	L8080	1050	DPR	8080
679616.5	6670269	L8070	14	DPR	8070
678554.6	6669853	L8070	462	DPR	8070
678248	6669838	L8060	532	DPR	8060
678207.6	6669935	L8050	623	DPR	8050
678233.6	6670051	L8040	560	DPR	8040
678227.9	6670161	L8030	518	DPR	8030
678332.1	6670302	L8020	637	DPR	8020
678250.1	6670379	L8010	539	DPR	8010
678281.1	6670493	L8000	721	DPR	8000

CARIBOU

X	Y	Fid	Type	Line Number
661525.8	6686755	553	SPR	L14000

APPENDIX C: NOTES ON MAGNETIC PROCESSING & EM3D MODELS

GEOPHYSICS, VOL. 61, NO. 2 (MARCH-APRIL 1996); P. 394-408, 18 FIGS.

3-D inversion of magnetic data

Yaoguo Li* and Douglas W. Oldenburg*

ABSTRACT

We present a method for inverting surface magnetic data to recover 3-D susceptibility models. To allow the maximum flexibility for the model to represent geologically realistic structures, we discretize the 3-D model region into a set of rectangular cells, each having a constant susceptibility. The number of cells is generally far greater than the number of the data available, and thus we solve an underdetermined problem. Solutions are obtained by minimizing a global objective function composed of the model objective function and data misfit. The algorithm can incorporate a priori information into the model objective function by using one or more appropriate weighting functions. The model for inversion can be either susceptibility or its logarithm. If susceptibility is chosen, a positivity constraint is imposed to reduce the nonuniqueness and to maintain physical realizability. Our algorithm assumes that there is no remanent magnetization and that the magnetic data are produced by induced magnetization only. All minimizations are carried out with a subspace approach where only a small number of search vectors is used at each iteration. This obviates the need to solve a large system of equations directly, and hence earth models with many cells can be solved on a deskside workstation. The algorithm is tested on synthetic examples and on a field data set.

INTRODUCTION

Magnetic surveying has been used widely over the years, resulting in a great amount of data with enormous area1 coverage. Magnetic data have been used for mapping geological structures, especially in the reconnaissance stage of exploration, but when used in detailed prospecting, robust and efficient inversion algorithms must be used. However, a principal difficulty with the inversion of the potential data is the inherent nonuniqueness. By Gauss' theorem, if the field distribution is known only on a bounding surface, there are infinitely many equivalent source distributions inside the boundary that can produce the known field. Any magnetic field measured on the surface of the earth can be reproduced by an infinitesimally thin zone of magnetic dipoles beneath the surface. From a mathematical perspective, this means there is no depth resolution inherent in magnetic field data. A second source for nonuniqueness is the fact that magnetic observations are finite in number and are inaccurate. If there exists one model that reproduces the data, there are other models that will reproduce the data to the same degree of accuracy. The severity of the nonuniqueness problem for magnetic data is illustrated in Figures l-3. (The gray scale in all figures indicates susceptibility in SI units for model sections and magnetic data in nT for data plots.) A 3-D dipping prism of uniform susceptibility in Figure 1 produces the surface magnetic field shown in Figure 2, which consists of 441 data. Slices of a 3-D susceptibility model that adequately reproduces the 441 data are shown in Figure 3. That result, however, bears little resemblance to the true model. Susceptibility is concentrated near the surface and displays zones of negative values. This mathematical model solution provides little information about the true structure that is useful.

Faced with this extreme nonuniqueness, previous authors have mainly taken two approaches in the inversion of magnetic data. The first is parametric inversion, where the parameters of a few geometrically simple bodies are sought in a nonlinear inversion and values are found by solving an overdetermined problem. This methodology is suited for anomalies known to be generated by simple causative bodies, but it requires a great deal of a priori knowledge about the source expressed in the form of an initial parameterization, an initial guess for parameter values, and limits on the susceptibility allowed (e.g., Bhattacharyya, 1980; Zeyen and Pous, 1991). Nonuniqueness is not generally an issue because only a small subset of possible models is considered due to the restrictive nature of the inversion algorithm. A related, but unique, approach in Wang and Hansen (1990) assumes polyhedronal causative bodies and

Presented at the 63rd Annual International Meeting, Society of Exploration Geophysicists. Manuscript received by the Editor May 2, 1994; revised manuscript received June 29, 1995.
*UBC-Geophysical Inversion Facility, Dept. of Geophysics and Astronomy, University of British Columbia, 129-2219 Main Mall, Vancouver, BC V6T 1Z4, Canada.
© 1996 Society of Exploration Geophysicists. All rights reserved.

inverts for the position of the vertices of these bodies using the spectrum of the magnetic data. The method is general in principle but has difficulties both in constructing the causative bodies from the recovered vertices and in obtaining the susceptibility distribution.

In the second approach to inverting magnetic data, the earth is divided into a large number of cells of fixed size but of unknown susceptibility. Nonuniqueness of solution is recognized and the algorithm produces a single model by minimizing an objective function of the model subject to fitting the data. Green (1975) minimizes a weighted model norm with respect to a reference model, and this allows the interpreter to guide the inversion by varying the weighting according to the available information. Last and Kubik (1983) choose to minimize the total volume of the causative body so that the final model is compact and structurally simple. Guillen and Menichetti (1984) minimize the moment of inertia of the causative body with respect to the center of gravity or an axis passing through it. Their inversion result is guided by the estimate of the central depth and dip of the causative body. These approaches have merit but they are not flexible enough to handle problems we are concerned with. This is especially true of methods that attempt to collapse the anomalous susceptibility into a single body; such a solution is rarely an adequate representation of geologic structure.

In our inversion approach, we first make a decision about the variable in which the interpretation is to be made, that is, whether susceptibility, log susceptibility, or some function of susceptibility is sought. Next, we form a multicomponent objective function that has the flexibility to generate different types of models. The form of this objective function is such that it can correct for the undesirable aspects of the mathematically acceptable model in Figure 3, namely-the concentration of susceptibility near the surface, the excessive structure, and the existence of negative susceptibilities. Our objective function incorporates an optional reference model so that the constructed model is close to that. It penalizes roughness in three spatial directions, and it has a depth weighting designed to distribute the susceptibility with depth. Additional 3-D weighting functions in the objective function can be used to incorporate further information about the model. Such information might be available from other geophysical surveys, geological data, or the interpreter's qualitative or quantitative understanding of the geologic structure and its relation to the magnetic susceptibility. These 3-D weighting functions can also be used to answer questions about the existence of susceptibility features found from previous inversions. Negative susceptibilities are prevented by making a transformation of

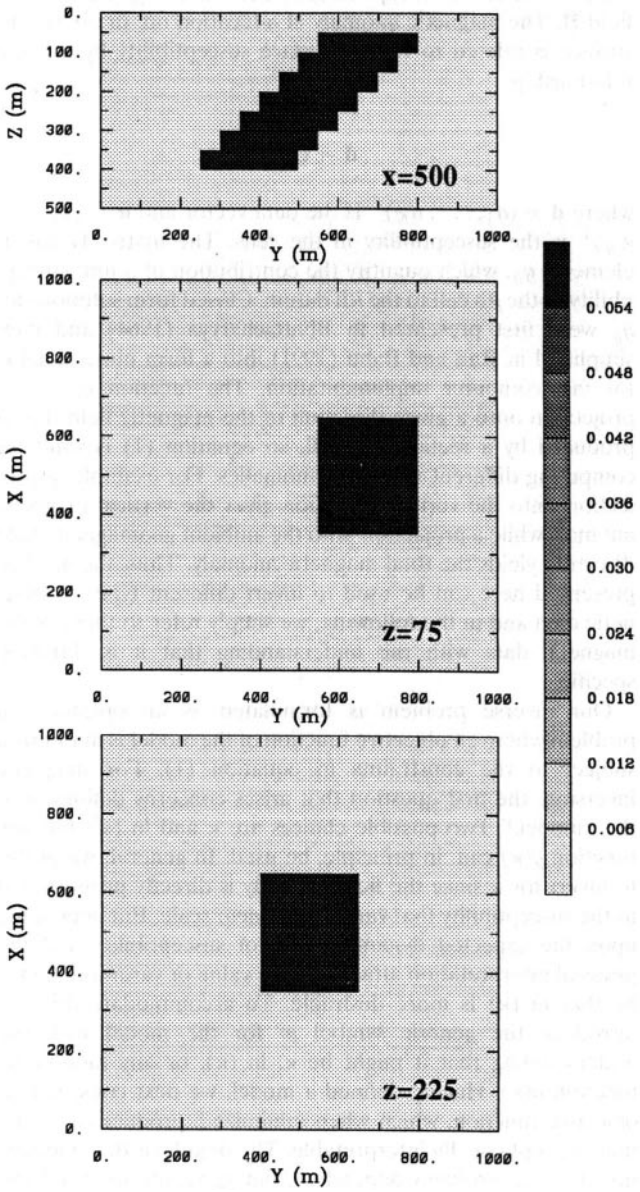


FIG. 1. Slices through a 3-D magnetic susceptibility model composed of a dipping slab in a nonsusceptible half-space. The slab is buried at a depth of 50 m and extends to 400-m depth at a dip angle of 45° . The gray scale indicates the value of magnetic susceptibility in SI units.

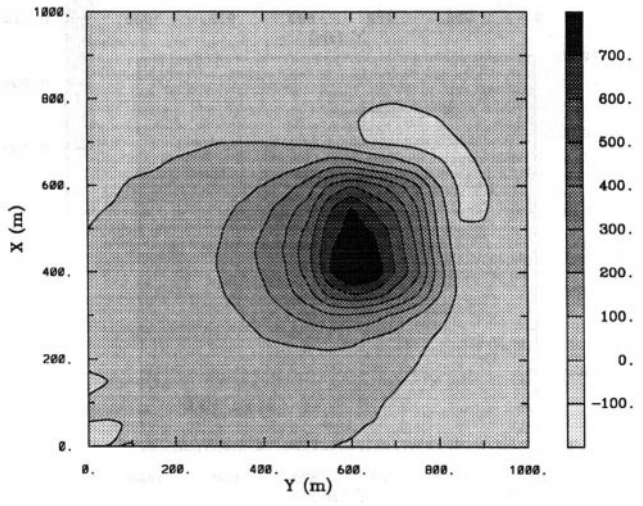


FIG. 2. The total field anomaly produced by the slab model in Figure 1. The inducing field has direction $I = 75°$ and $D = 25°$ and a strength of 50 000 nT. Uncorrelated Gaussian noise, with a standard deviation of 2% of the datum magnitude plus 1 nT, is added to the data. The gray scale indicates the magnetic anomaly in nT.

variables and solving a nonlinear inverse problem. The numerical solution for the inversion is accomplished by dividing the earth into a large number of cells so that relatively complex geologic bodies can be constructed. The computational difficulties often encountered in solving large matrix systems are avoided by working explicitly with a generalized subspace algorithm.

The paper begins by outlining our inversion methodology and empirically estimating parameters for the depth weighting based upon synthetic inversion of single 3-D prisms. Data from two synthetic models are then inverted. The paper concludes by inverting a field data set over a copper-gold porphyry deposit and a subsequent discussion.

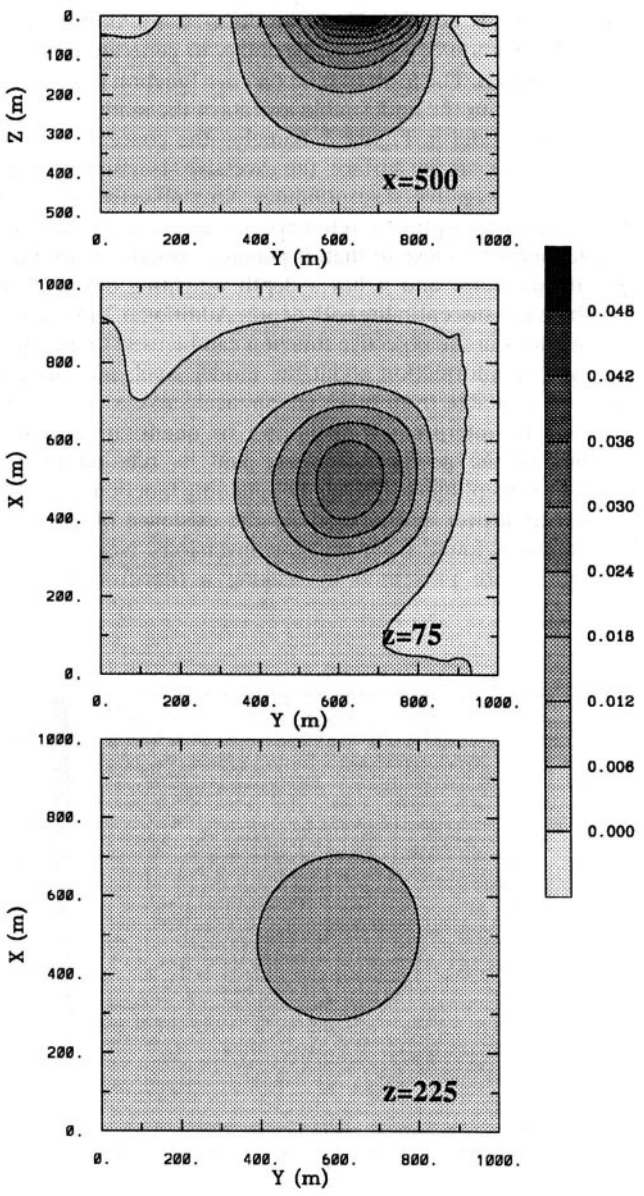


FIG. 3. The susceptibility model constructed by minimizing $\|\kappa\|^2$ subject to fitting the data in Figure 2. As a mathematical solution, this model provides little, if any, information about the subsurface susceptibility distribution. It effectively illustrates the nonuniqueness inherent to the inversion of static magnetic field data.

INVERSION METHODOLOGY

Each magnetic anomaly datum observed above the surface can be evaluated by calculating the projection of the anomalous magnetic field onto a given direction. Let the source region be divided into a set of rectangular cells by an orthogonal 3-D mesh and assume a constant magnetic susceptibility value κ within each cell. Further we assume that there is no remanent magnetization and that the demagnetization effect is negligible. Thus only the induced magnetization is considered. This magnetization is uniform within each cell and is given by the product of the susceptibility and the inducing geomagnetic field $\underline{\mathbf{H}}$. The magnetic anomaly at a location on, or above, the surface is related to the subsurface susceptibility by a linear relationship

$$\mathbf{d} = \underline{\mathbf{G}}\boldsymbol{\kappa}, \tag{1}$$

where $\mathbf{d} = (d_1, \ldots, d_N)^T$ is the data vector and $\boldsymbol{\kappa} = (\kappa_1, \ldots, \kappa_M)^T$ is the susceptibility in the cells. The matrix $\underline{\mathbf{G}}$ has as elements g_{ij}, which quantify the contribution of a unit susceptibility in thejth cell to the ith datum. Closed form solutions for g_{ij} were first presented in Bhattacharyya (1964) and later simplified in Rao and Babu (1991) into a form more suitable for fast computer implementation. The function g_{ij} is the projection onto a given direction of the magnetic field that is produced by a rectangular cell, so equation (1) is valid for computing different magnetic anomalies. For example, a projection onto the vertical direction gives the vertical magnetic anomaly while a projection onto the ambient geomagnetic field direction yields the total magnetic anomaly. Thus, the method presented here can be used to invert different types of magnetic data and in the following, we simply refer to them as the magnetic data with the understanding that it is direction specific.

Our inverse problem is formulated as an optimization problem where an objective function of the model is minimized subject to the constraints in equation (1). For magnetic inversion, the first question that arises concerns definition of the "model." Two possible choices are κ and $\ln(\kappa)$, but any function $g(\kappa)$ can, in principle, be used. In general, we prefer to invert for κ since the field anomaly is directly proportional to the susceptibility that varies on a linear scale. But depending upon the expected dynamic range of susceptibility and the physical interpretation attached to its value or variation, it may be that $\ln(\kappa)$ is more desirable. To accommodate this, we introduce the generic symbol m for the model with the understanding that it might be κ, $\ln(\kappa)$, or any monotonic function $g(\kappa)$. Having defined a model, we next construct an objective function, which when minimized, produces a model that is geophysically interpretable. The details of the objective function are problem dependent, but generally we need the flexibility to be close to a reference model m_0 and also require that the model be relatively smooth in three spatial directions. Here we adopt a right-handed Cartesian coordinate system with x positive north and z positive down. Let the model objective function be

$$\phi_m(m) = \alpha_s \int_V w_s\{w(z)[m(\mathbf{r}) - m_0]\}^2\, dv + \alpha_x \int_V w_x\left\{\frac{\partial w(z)[m(\mathbf{r}) - m_0]}{\partial x}\right\}^2 dv + \alpha_y \int_V w_y\left\{\frac{\partial w(z)[m(\mathbf{r}) - m_0]}{\partial y}\right\}^2 dv + \alpha_z \int_V w_z\left\{\frac{\partial w(z)[m(\mathbf{r}) - m_0]}{\partial z}\right\}^2 dv, \quad (2)$$

where functions w_s, w_x, w_y, and w_z are spatially dependent weighting functions while α_s, α_x, α_y, and α_z are coefficients that affect the relative importance of different components in the objective function. Here, $w(z)$ is a depth weighting function. It is convenient to write equation (2) as $\phi_m(m) = \phi_{ms} + \phi_{mv}$, where ϕ_{ms} refers to the first term in equation (2) and ϕ_{mv} refers collectively to the remaining three terms that involve variation of the model in three spatial directions.

The objective function in equation (2) has the flexibility of constructing many different models. The reference model m_0 may be a general background model that is estimated from previous investigations, or it could be the zero model. The reference model would generally be included in ϕ_{ms} but can be removed if desired from any of the remaining terms. Often we are more confident in specifying the value of the model at a particular point than in supplying an estimate of the gradient. The relative closeness of the final model to the reference model at any location is controlled by the function w,. For example, if the interpreter has high confidence in the reference model at a particular region, he or she can specify w_s to have increased amplitude there compared to other regions of the model. The weighting functions w_x, w_y, and w_z can be designed to enhance or attenuate structures in various regions in the model domain. If geology suggests a rapid transition zone in the model, then a decreased penalty for variation can be put there, and the constructed model will exhibit higher gradients provided that this feature does not contradict the data. Therefore, the reference model and four 3-D weighting functions allow for the incorporation into the inversion of additional information other than the magnetic data. The additional information can be from previous knowledge about the susceptibility, from other geophysical surveys, or from the interpreter's qualitative or quantitative understanding about the geologic structure and its relation to susceptibility. When this extra information is incorporated, the inversion derives a model that not only fits the data, but more importantly, also has a likelihood of representing the earth. From the viewpoint of magnetic inversion, such an approach allows one to construct a most-likely earth model that uses all available information, and it can also be used to explore the nonuniqueness. These two aspects form the foundation of a responsible interpretation.

The kernels (values of g_{ij}) for the surface magnetic data decay with depth. It is for this reason that an inversion that minimizes $\|m - m_0\|^2 = \int (m - m_0)^2\, dv$ subject to fitting the data will generate a susceptibility that is concentrated near the surface. To counteract the geometric decay of the kernels and to distribute susceptibility with depth, we introduce a weighting of the form $w(z) = (z + z_0)^{-\beta/2}$ into ϕ_{ms}, and optionally include it in ϕ_{mv}. The values of β and z_0 are investigated in the following section, but their choice essentially allows equal chance for cells at different depths to be nonzero.

The next step in setting up the inversion is to define a misfit measure. Here we use the 2-norm measure

$$\phi_d = \|\underline{\mathbf{W}}_d(\mathbf{d} - \mathbf{d}^{obs})\|_2^2, \quad (3)$$

and we assume that the contaminating noise on the data is independent and Gaussian with zero mean. Specifying $\underline{\mathbf{W}}_d$ to be a diagonal matrix whose ith element is $1/\sigma_i$ where σ_i is the standard deviation of the ith datum, makes ϕ_d a chi-squared variable distributed with N degrees of freedom. Accordingly $E[\chi^2] = N$ provides a target misfit for the inversion.

The inverse problem is solved by finding a model m that minimizes ϕ_m and misfits the data by a predetermined amount. This is accomplished by minimizing $\phi(m) = \phi_m + \lambda^{-1}(\phi_d - \phi_d^*)$, where ϕ_d^* is our target misfit and λ is a Lagrangian multiplier. To perform a numerical solution, we first discretize the objective function in equation (2) using a finite-difference approximation according to the mesh defining the susceptibility model. This yields

$$\phi_m(\mathbf{m}) = \phi_{ms} + \phi_{mv} = (\mathbf{m} - \mathbf{m}_0)^T\underline{\mathbf{W}}_s^T\underline{\mathbf{W}}_s(\mathbf{m} - \mathbf{m}_0) + (\mathbf{m} - \mathbf{m}_0)^T(\underline{\mathbf{W}}_x^T\underline{\mathbf{W}}_x + \underline{\mathbf{W}}_y^T\underline{\mathbf{W}}_y + \underline{\mathbf{W}}_z^T\underline{\mathbf{W}}_z)(\mathbf{m} - \mathbf{m}_0)$$
$$\equiv (\mathbf{m} - \mathbf{m}_0)^T\underline{\mathbf{W}}_m^T\underline{\mathbf{W}}_m(\mathbf{m} - \mathbf{m}_0) = \|\underline{\mathbf{W}}_m(\mathbf{m} - \mathbf{m}_0)\|^2, \quad (4)$$

where $\mathbf{m}$ and $\mathbf{m_0}$ are M- length vectors. The individual matrices $\underline{\mathbf{W}}_s$, $\underline{\mathbf{W}}_x$, $\underline{\mathbf{W}}_y$, $\underline{\mathbf{W}}_z$ are calculated straightforwardly once the model mesh and the weighting functions w_s, w_x, w_y, w_z, and $w(z)$ are defined (see Appendix). The cumulative matrix $\underline{\mathbf{W}}_m^T\underline{\mathbf{W}}_m$ is then formed. For our formulation, the matrix $\underline{\mathbf{W}}_m$ is never computed explicitly but we shall use it to derive our final equations.

The inverse problem is solved by minimizing $\phi(\mathbf{m})$ with an appropriate minimization technique. To reduce computation and to invoke positivity, we use a subspace methodology. In its general form, the subspace technique allows the model parameter to be both positive and negative, and thus to ensure positive susceptibility, we may need to invoke a transformation

of variables. Whether or not the transformation is required depends upon the relationship between m_i and κ_i. If $m_i = \ln(\kappa_i)$, so that interpretations are carried out in the logarithmic domain, then no further transformation is necessary since κ_i will be positive irrespective of the sign of m_i. However, if $m_i = \kappa_i$, or $m_i = g(\kappa_i)$, and $g(\kappa)$ is a positive function, then a transformation is required. All possibilities can be handled by introducing a new parameter p, such that $m_i = f(p_i)$, where $f(p)$ is a monotonic function whose inverse and first-order derivative exist. This mapping is then incorporated directly into the subspace minimization process.

Let $\mathbf{p}^{(n)}$ denote the parameter vector at the nth iteration and δp denote the sought perturbation. Performing a Taylor expansion of the perturbed model objective function about the point $\mathbf{p}^{(n)}$ yields

$$\phi_m(\mathbf{p}^{(n)} + \delta p) = \|\underline{\mathbf{W}}_m \underline{\mathbf{F}} \delta p + \underline{\mathbf{W}}_m(\mathbf{m}^{(n)} - \mathbf{m}_0)\|^2, \tag{5}$$

where $\underline{\mathbf{F}}$ is a diagonal matrix with elements

$$F_{ii} = \left.\frac{\partial f_i}{\partial p}\right|_{p_i^{(n)}} = \left.\frac{\partial m_i}{\partial p_i}\right|_{p_i^{(n)}}. \tag{6}$$

A similar Taylor expansion applied to the misfit objective functional $\phi_d(\mathbf{p}^{(n)} + \delta p)$ yields

$$\phi_d = \|\underline{\mathbf{W}}_d \underline{\mathbf{G}} \underline{\mathbf{F}} \delta p + \underline{\mathbf{W}}_d(\mathbf{d}(\mathbf{p}^{(n)}) - \mathbf{d}^{obs})\|^2. \tag{7}$$

At each iteration we desire a perturbation that minimizes equation (4) subject to generating a data misfit of $\phi_d = \phi_d^{*(n)}$, where $\phi_d^{*(n)}$ is the target misfit at the nth iteration. In the subspace technique we represent the perturbation as

$$\delta p = \sum_{i=1}^{q} \alpha_i \mathbf{v}_i \equiv \underline{\mathbf{V}} \boldsymbol{\alpha}, \tag{8}$$

where the M-length vectors $\mathbf{v}_i$ ($i = 1, q$) are as yet arbitrary. Writing the objective function to be minimized in terms of the coefficients $\boldsymbol{\alpha}$ yields

$$\phi(\boldsymbol{\alpha}) = \|\underline{\mathbf{W}}_m \underline{\mathbf{F}} \underline{\mathbf{V}} \boldsymbol{\alpha} + \underline{\mathbf{W}}_m(\mathbf{m}^{(n)} - \mathbf{m}_0)\|^2 + \lambda^{-1}(\|\underline{\mathbf{W}}_d \underline{\mathbf{G}} \underline{\mathbf{F}} \underline{\mathbf{V}} \boldsymbol{\alpha} + \underline{\mathbf{W}}_d(\mathbf{d}(\mathbf{p}^{(n)}) - \mathbf{d}^{obs})\|^2 - \phi_d^*). \tag{9}$$

Differentiating with respect to the coefficients a yields the final equations

$$\underline{\mathbf{B}} \boldsymbol{\alpha} = \mathbf{b},$$

$$\underline{\mathbf{B}} = \underline{\mathbf{V}}^T \underline{\mathbf{F}}^T (\underline{\mathbf{G}}^T \underline{\mathbf{W}}_d^T \underline{\mathbf{W}}_d \underline{\mathbf{G}} + \lambda \underline{\mathbf{W}}_m^T \underline{\mathbf{W}}_m) \underline{\mathbf{F}} \underline{\mathbf{V}},$$

$$\mathbf{b} = -\underline{\mathbf{V}}^T \underline{\mathbf{F}}^T \underline{\mathbf{G}}^T \underline{\mathbf{W}}_d^T \underline{\mathbf{W}}_d (\mathbf{d}^{(n)} - \mathbf{d}^{obs}) - \lambda \underline{\mathbf{V}}^T \underline{\mathbf{F}}^T \underline{\mathbf{W}}_m^T \underline{\mathbf{W}}_m (\mathbf{m}^{(n)} - \mathbf{m}_0). \tag{10}$$

We note that the matrix $\underline{\mathbf{B}}$ is q x q and therefore the system of equations is easily solved if q is small. At each iteration, we search for a value of λ that yields the target misfit for that iteration. If the target misfit cannot be reached, then the value of λ that achieves the smallest misfit is taken. The search is usually accomplished by solving equation (10) a number of times using different λ values. Once the optimum value of λ is found, the system is solved again to obtain the coefficients $\boldsymbol{\alpha}$ and the model perturbation. This iterative process is continued until the final expected data misfit is achieved and the model objective function undergoes no significant decrease with successive iterations. Subspace vectors $\mathbf{v}_i$ are generated mainly from the gradients of the data and model objective functions. The data are grouped to form subobjective functions of misfit, and a steepest descent vector corresponding to each subobjective function is used as a subspace vector. Partitioning of the data can be formed by grouping data that are spatially close, or by grouping data such that each group has approximately the same contribution to the total data misfit. Both approaches have worked well. The model objective function is partitioned and the gradient vector associated with each of the four components in the model objective function provides additional subspace vectors. In addition, a constant vector is always included, and the selected subspace vectors are orthonormalized before being used in the search. More details on the implementation of the subspace method for the linear inverse problem can be found in Oldenburg and Li (1994).

The final item of practical importance is the specification of the mapping needed to ensure positivity of susceptibility. The positivity is required since we are dealing only with induced magnetization, and the presence of negative susceptibility is negligible in practical geophysical applications. Although our formalism permits the minimization of $m = g(\kappa)$, the two most common situations are $m = \ln(\kappa)$ and $m = \kappa$. When $m = \ln(\kappa)$, we set $p = m$ and hence the matrix $\underline{\mathbf{F}}$ in equation (10) is the identity matrix. If $m = \kappa$, we use the two-stage mapping proposed in Oldenburg and Li (1994). It is composed of an exponential segment and a straight line. The two segments are joined together such that the mapping and its first derivative are both continuous. The mapping is given by

$$\kappa = \begin{cases} 0 & p < p_b \\ e^p - \kappa_b & p_b \le p \le p_1 \\ (p - p_1 + 1)e^{p_1} - \kappa_b & p > p_1 \end{cases}, \tag{11}$$

where $p = p_1$ is the transition point between exponential and linear segments, and κ_b is selected to be small enough such that susceptibilities smaller than κ_b are not significantly different from zero when the final interpretation is carried out. Here, κ_1 and hence p_1 are chosen so that the ratio $(\kappa_1 + \kappa_b)/\kappa_b$ does not exceed about two orders of magnitude. This prevents the elements F_{ii} from becoming too disparate. We note that the ith row of $\underline{\mathbf{V}}$ is multiplied by F_{ii}, and if this value is too small, the ith row of $\underline{\mathbf{V}}$ is essentially annihilated and there will be no possibility of adjusting the value of the ith cell. However, if the ratio is too small, the flexibility in the mapping will be restricted and this affects the convergence rate of the algorithm. In the limit that $\kappa_b \to \kappa_1$, the nonlinear mapping degenerates into a linear truncation and the inversion will not converge. However, between the above two extremes, there is a wide range of values for the ratio that can yield a good mapping. Based upon numerical experiments (Oldenburg and Li, 1994), we have chosen a value of 50.0 for this ratio for the examples throughout this paper.

DEPTH WEIGHTING

It is well known that static magnetic data have no inherent depth resolution. For instance, when minimizing $\|m\|_2^2 = \int m^2\, dv$, structures tend to concentrate near the surface regardless of the true depth of the causative bodies. In terms of model construction, this is a direct manifestation of the nature of the kernels whose amplitudes rapidly diminish with depth. The tendency to put structure at the surface can be overcome by introducing a depth weighting to counteract this natural decay. Intuitively, a weighting that approximately compensates for the decay gives cells at different depths equal probability to enter into the solution with a nonzero susceptibility. Before proceeding with the details of the weighting function for magnetic inversion, we illustrate the necessity, and effectiveness, of such a weighting function using a simple 1-D problem.

Consider a set of data $\mathbf{d} = (d_1, , \ldots, d_N)^T$ generated from the equation

$$d_i = \int_0^1 g_i(z) m(z)\, dz, \qquad i = 0, \ldots, N, \tag{12}$$

where the kernels are

$$g_i(z) = e^{-az} \cos(2\pi i z).$$

The decay factor e^{-az} causes the constructed model m,(z) to have structure concentrating toward the region of small z in the classic model construction that minimizes $\|m\|^2$, since the model will be a linear combination of the kernels, i.e.,

$$m_c(z) = \sum_{i=0}^{N} \alpha_i e^{-az} \cos(2\pi i z). \tag{13}$$

This is shown in Figure 4a and 4b for two different models. These models are constructed from five data (i = 0,4) to which noise has been added. It is apparent that the constructed model is shifted toward small z where the amplitude of kernels is relatively large. One way to counteract the bias is to seek a solution in model space that is spanned by the nondecaying portion of the kernels, in this case just the cosine functions. The desired model would have the form

$$m_c(z) = \sum_{i=0}^{N} \tilde{\alpha}_i \cos(2\pi i z), \tag{14}$$

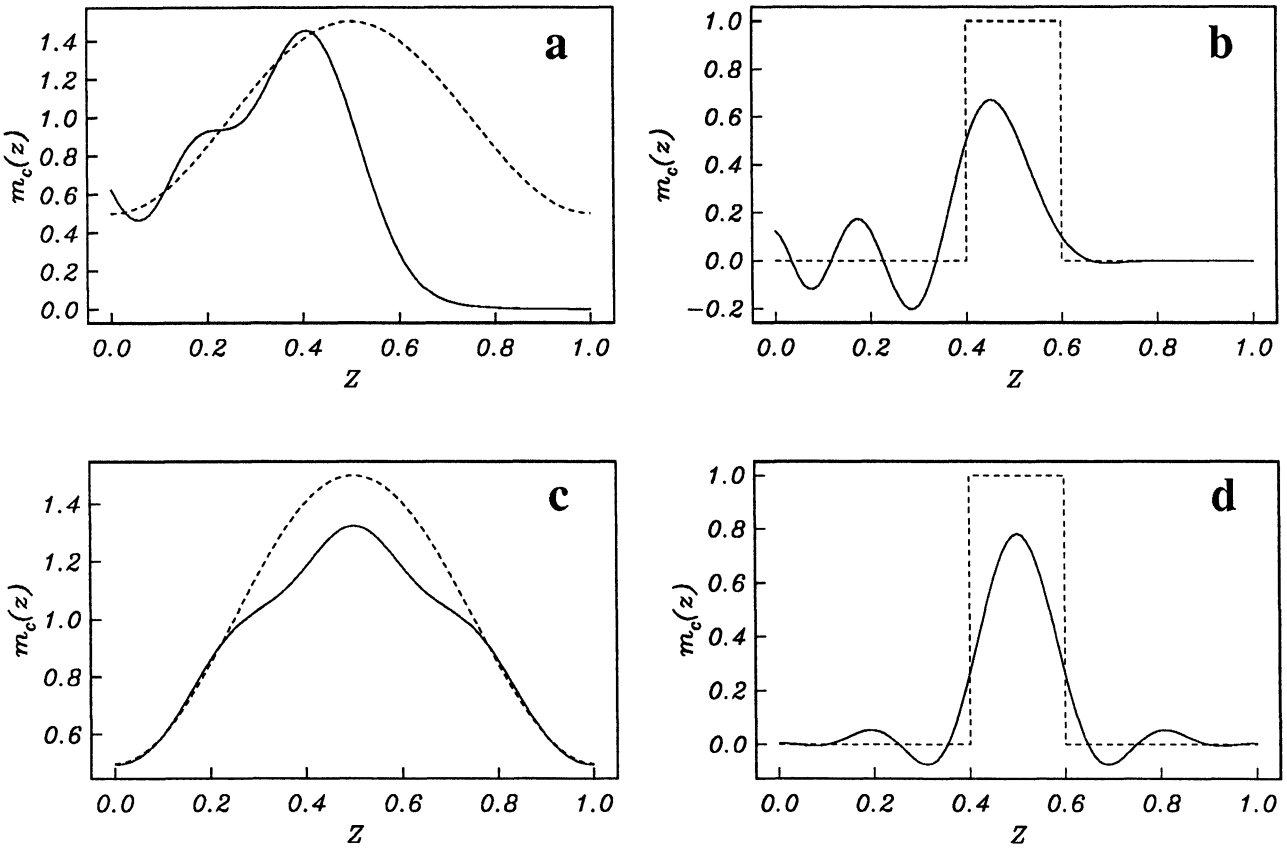


FIG. 4. A 1-D example showing the use of a weighting function in the inversion procedures to counteract the natural decay in the kernel function. In all panels the dashed line shows the true model. Panels (a) and (b) show, for the two different true models, respectively, the model constructed using the original kernel functions with the decaying factor e^{-az}. Notice the shift of the recovered model towards the small z region. Panels (c) and (d) show the weighted models recovered by applying a weighting function $w(z) = e^{-az/2}$. They are better representations of the true model.

where $\tilde{\alpha}_i$ are coefficients. Free from the influence from the decay factor, a model constructed from this set of basic functions should have a better chance of having significantly high values at depth.

We accomplish this by finding an appropriate weighting function $w(z)$. We first rewrite the data equation as

$$d_i = \int_0^1 \frac{g_i(z)}{w(z)} * w(z)m(z)\,dv \equiv \int_0^1 g_i^w(z)m^w(z)\,dv, \quad (15)$$

where $g_i^w(z)$ are the weighted kernels and $m^w(z)$ is the weighted model. Then the inverse problem is solved by minimizing $\|m^w(z)\|^2$ and the solution is given by

$$m_c^w(z) = \sum_{i=0}^{N} \tilde{\alpha}_i g_i^w(z). \quad (16)$$

Dividing $m_c^w(z)$ by the weighting function and substituting in $g_i^w(z)$ yields

$$m_c(z) = \sum_{i=0}^{N} \tilde{\alpha}_i \frac{g_i(z)}{w^2(z)} = \sum_{i=0}^{N} \tilde{\alpha}_i \frac{e^{-az}\cos(2\pi iz)}{w^2(z)}. \quad (17)$$

This equation can be made identical to equation (14) by choosing $w(z) = e^{-az/2}$. Carrying out the weighted inversion for the above two data sets produces models shown in Figures 4c and 4d. They are much better representations of true models.

This methodology is then applied to the inversion of surface magnetic data by finding the appropriate weighting function that counteracts the depth decay of the data kernels. There is no distinct separable factor defining the decay in the kernel, therefore we resort to an empirical estimate. Since the decay rate depends upon the observation height as well as the size and aspect ratios of the cells making up the 3-D model, such estimates are expected to be problem dependent. Numerical experiments indicate that the function of the form $(z + z_0)^{-3}$ closely approximates the kernel's decay directly under the observation point, given a correctly chosen value of z_0. This is consistent with the fact that, to first order, a cubic-shaped cell acts like a dipole source whose magnetic field decays by inverse distance cubed. The value of z_0 can be obtained by matching the function $(z + z_0)^{-3}$ with the kernel function beneath the observation point. Thus, a reasonable candidate for the depth weighting function is given by

$$w(z) = \frac{1}{(z + z_0)^{3/2}}. \quad (18)$$

The susceptibility model constructed by minimizing a model objective function consisting of only ϕ_{ms}, i.e.,

$$\phi_m(m) = \int_V (w(z)m(x, y, z))^2\,dv, \quad (19)$$

subject to fitting the data should place the recovered anomaly at approximately the depth of the causative body. This hypothesis is tested by inverting surface data produced by a susceptible cubic body at three different, depths. The cube is 200 m on a side. Data are calculated over a 21 **X** 21 grid of 50-m spacing in both directions, and 2% Gaussian noise is then added. The observation is assumed to be 1 m above the surface and the inducing field has $I = 75°$, $D = 25°$. The region directly beneath the data grid is taken as the model domain and discretized into 4000 cells (20 cells in each horizontal direction and 10 along depth) of 50 m on a side.

Given the stated data parameters and model discretization, the estimated value of z_0 in the depth weighting function is 25 m. Figure 5 shows the comparison of the kernel beneath a datum point and the function $w^2(z)$. This weighting function is used to invert surface data caused by the susceptible prism, and the results of minimizing ϕ_{ms} are shown in Figure 6. Each panel in the figure is the cross-section through the center of the model obtained by inverting the data set produced by a cube at a different depth. They are rather good recoveries in terms of source depth, which is indicated by the superimposed outline of the true body in each section.

In the above analysis we have established a practical way for estimating an appropriate depth weighting function that distributes the susceptibility more uniformly with depth. The weighting is valid when the model objective function consists only of ϕ_{ms}. In general, we like to include a penalty against roughness and thereby produce a model that is smooth. To incorporate the above weighting scheme in the spatial variations, we make the following argument. Since minimizing ϕ_{ms} tends to provide a reasonable depth distribution, we wish only to improve the model's smoothness while maintaining the depth characteristic. A conceptually consistent approach would be to apply the roughness measures to the weighted model. We form a generic model objective function

$$\phi_m(m) = \alpha_s \int_V w_s\{w(z)[m(\mathbf{r}) - m_0]\}^2\,dv + \alpha_x \int_V w_x\left\{\frac{\partial w(z)[m(\mathbf{r}) - m_0]}{\partial x}\right\}^2 dv + \alpha_y \int_V w_y\left\{\frac{\partial w(z)[m(\mathbf{r}) - m_0]}{\partial y}\right\}^2 dv$$

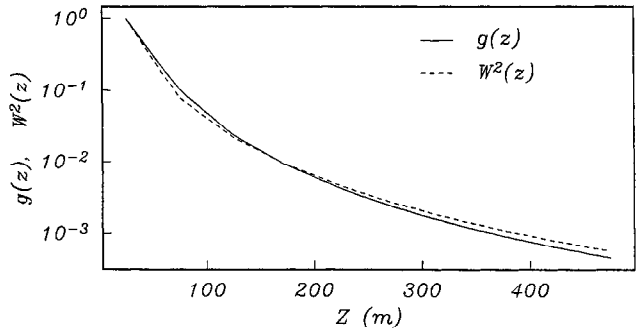


FIG. 5. Comparison of the kernel function (solid) directly beneath the observation point with the estimated curve (dashed) given by $w^2(z) = (z + z_0)^{-3}$ with $z_0 = 25$ m. The source cell is a cube of 50 m on a side. Here, z denotes the depth to the center of the cell. Both curves are normalized for comparison.

$$+ \alpha_z \int_V w_z \left\{ \frac{\partial w(z)[m(\mathbf{r}) - m_0]}{\partial z} \right\}^2 dv, \qquad (20)$$

where the depth weighting is applied inside the derivatives of the roughness components and the reference model m_0 can be removed from any term if desired. This type of depth weighting has proven to work satisfactorily on a number of synthetic examples and is the default choice in our algorithm. The examples to be presented in the following sections all use this depth weighting function.

Before proceeding further, we remark that the above weighting represents only one possibility. One could potentially design a different weighting by incorporating the depth weighting in the usual 3-D weighting functions w_s, w_x, w_y, w_z. Such an approach applies the depth weighting outside the derivative operators directly. However, the decay rate of the depth weighting for each component will be different, and it is difficult to establish a consistent rule for the choice of the different weightings. In addition, the extra set of parameters required by such a weighting scheme introduces more subjectivity into the inversion process. We have not explored this approach in detail; however, it is observed that straightforward inclusion of the depth weighting derived above into the 3-D weighting function in the form of $\int_V w_z w^2(z)\{\partial[m(\mathbf{r}) - m_0]/\partial z\}^2 dv$ can yield reasonable results.

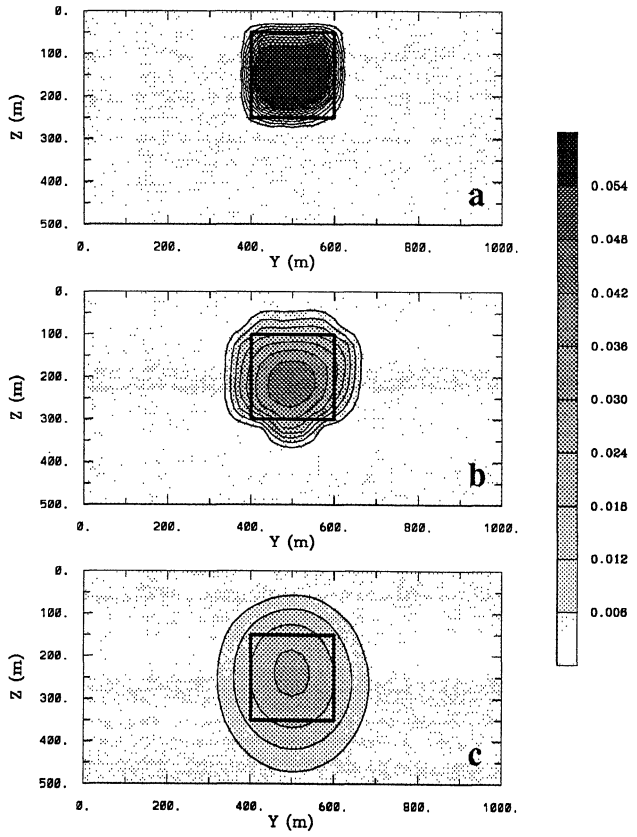


FIG. 6. Cross-sections through the center of the recovered model for a cube at a central depth of 150,200, and 250 m. The cube is 200 m on a side. The inversion uses the weighting function derived from the kernel decay estimated in Figure 5. The true position of the cube is outlined in each cross-section. As the true source depth increases and, as a result, the high-frequency content in the data decreases, the recovered model becomes increasingly smooth and attains a smaller amplitude. However, the depth of the recovered model is close to the true value.

PRACTICAL ASPECTS OF DATA PREPARATION

The data used in the inversion are the residual data obtained by subtracting a regional field from the initial observation. The inversion algorithm has been developed under the assumptions that the surface magnetic anomaly is produced by the induced magnetization only and that there are no remanent magnetization or demagnetization effects present. Incorrect removal of regional field, or any deviation from the above assumptions, is expected to cause a deterioration in the inversion results. Furthermore, the susceptibility distribution is mathematically represented by a piece-wise constant function defined on a user-specified grid of cells. Magnetic sources, however, have a wide range of physical sizes. In some cases, source dimensions will be significantly smaller than the size of cells in the mathematical model. If measurements are taken close to such a source, the resulting anomaly will have a width that is significantly smaller than that produced by a single cell in the mathematical model and this may produce artifacts. We ameliorate this problem by inverting data that have been upward continued to a height approximately equal to the width of the surface cells in the model. We arrive at this conclusion from a numerical experiment. We first generate the magnetic field H_ℓ from a small localized surface source that is assumed to be a cube of width ℓ. At each height h above the surface, a one-parameter inverse problem is carried out to find a uniform susceptibility of a large surface cube that has a width of L and shares a common horizontal center with the small cube. If H_L is the field of the large cell that best reproduces H_ℓ then the misfit functional,

$$r(h) = \frac{\int_{\Delta S} (H_\ell - H_L)^2 \, ds}{\int_{\Delta S} H_\ell^2 \, ds}, \qquad (21)$$

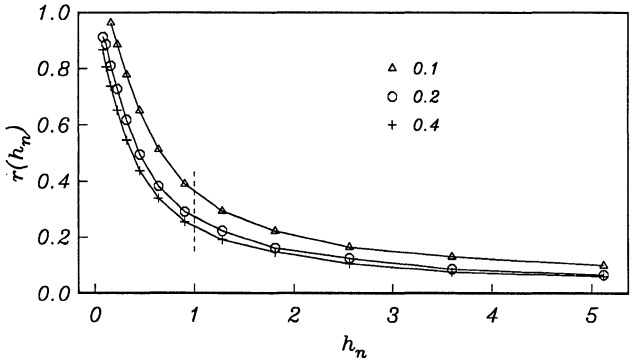


FIG. 7. The misfit between magnetic field as a result of a small cubic source and the field as a result of a larger cubic model cell having a best fitting susceptibility. The numbers indicate the ratio of the cell width. The misfit is plotted as a function of the observation height normalized by the width of the model cell. Note that the misfit decreases rapidly until the height is approximately equal to the width of the model cell, and that it changes slowly thereafter.

can be computed, where ΔS is the surface area of the data map. Figure 7 shows the misfit function r (h) for trial values of ℓ/L = 0.1, 0.2, 0.4. We note that r (h) decreases rapidly until $h \approx L$, and that it changes slowly thereafter. Since the above misfit analysis is a worst case scenario because the contaminating body is located at the surface, the suggestion of upward continuing the data to a height approximately equal to the width of surface cells may be somewhat conservative, and inversionists may want to vary this. However, in many field surveys, magnetically susceptible small bodies exist close to the surface and hence upward continuing the data prior to inversion is prudent.

SYNTHETIC EXAMPLES

As the first example, we invert the total field anomaly data given in the Introduction. The model consists of a 3-D dipping slab buried in a nonsusceptible half-space (slab model). Figure 1 shows three slices through the slab model. The susceptibility of the slab is 0.06 (SI unit). Under an inducing field with a strength of 50 000 nT and a direction at I = 75° and D = 25°, the slab model produces the surface total magnetic anomaly shown in Figure 2, which consists of 441 data over a 21 **X** 21 grid of 50-m spacing. The data have independent Gaussian noise added whose standard deviation is equal to 2% of the accurate datum magnitude plus 1 nT. We invert these 441 noise-contaminated data to recover the susceptibility of an earth model parametrized by 4000 cells of 50 m on a side (20 cells in each horizontal direction and 10 in depth).

The data are partitioned into 49 groups to provide 49 search vectors for the subspace algorithm. In addition, each component in the model objective function provides one basis vector, and a constant vector is included. For the depth weighting, the value of z_0 is estimated as 25 m. The additional 3-D weightings in the objective function are all set to unity. The reference susceptibility model is set to zero. For the nonlinear mapping, we choose κ_b = 0.0002 and κ_1 = 0.01.

First, we invert the data by minimizing an objective function composed only of the ϕ_{ms} and using $m = \kappa$ as the model parameter. A total of 51 subspace vectors are used at each iteration. The inversion reaches the expected misfit in 13 iterations but a few extra iterations are performed in an attempt to further reduce the value of the model objective function while keeping the misfit at the target value. By iteration 18, the objective function is decreasing by less than 1% per iteration, and the process is terminated. The constructed susceptibility model is shown in Figure 8 and can be compared with the true model in Figure 1. The tabular shape of the anomaly and its dipping structure are clear, and the depth extent is reasonably recovered. The amplitude of the recovered model is slightly higher than the true value, but the dip angle inferred from the recovered model is close to the true value. We point out that the model sections should be plotted using gray shading for each cell to reflect the piece-wise constant nature of the model. However, when the model has only a small number of cells in each spatial direction, the structural trends are more readily shown when contours are used. For this reason, we have contoured the model sections.

Next, the same data are inverted using a model objective function that includes penalty terms on spatial roughness, ϕ_{mv}. The depth weighting is applied to all terms, as in equation (20). The inversion uses 54 subspace vectors and achieves the expected misfit in 13 iterations. The recovered model is shown in Figure 9. It is smoother, has a slightly lower amplitude than the model in Figure 8, and it recovers the essential features of the true model such as the depth and dip angle.

It is observed, in this example and in other synthetic and field test examples, that minimizing either the first term in the model objective function in equation (20), ϕ_{ms}, or using all four terms, generates models that are reasonable representations of the true structure. In the absence of prior information, both models can provide useful information about the subsurface susceptibility distribution. However, the model minimizing ϕ_{ms} can be obtained at less computational cost. Further-

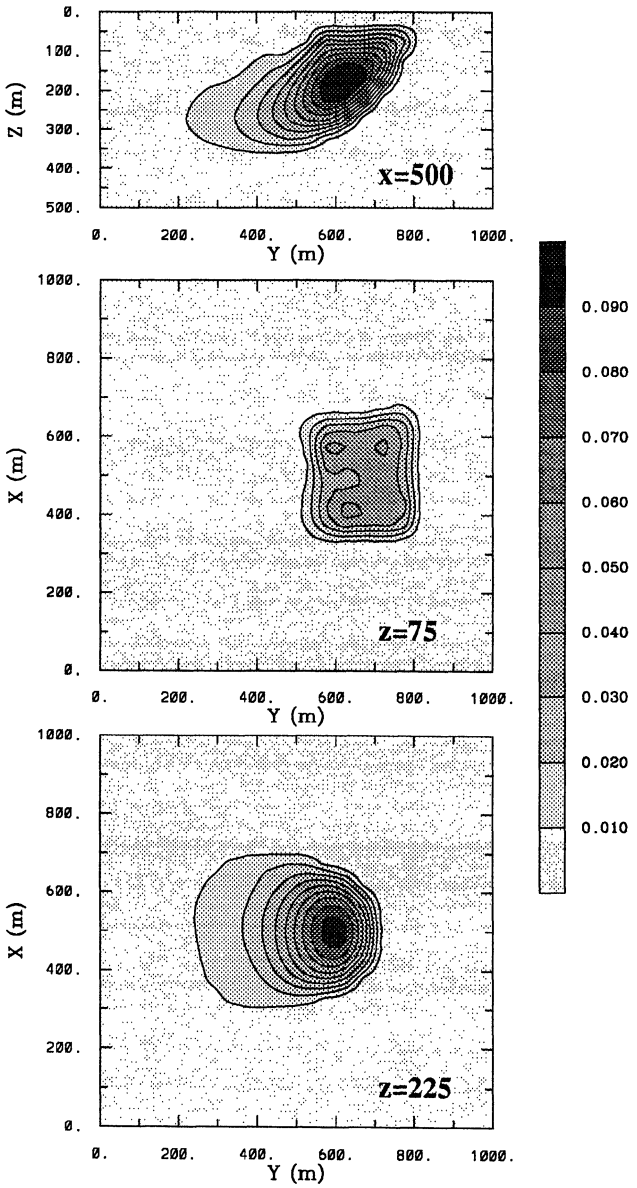


FIG. 8. Model obtained from inverting the data shown in Figure 2 by minimizing only ϕ_{ms}, which has the depth weighting applied. This is to be compared with the true model in Figure 1. The major features in the true model, such as dip angle and depth exte nt, are evident in the recovered model.

more, the depth weighting in this case is rather well supported by mathematical analysis whereas it is an argued extension for the three roughness components. Therefore, a reasonable approach to inverting field data might be a two-step process. The data can be inverted first by minimizing ϕ_{ms}, and the resultant model may be used in the interpretation as a preliminary result. If there are interesting features present and if one desires to refine the model by incorporating prior information to enhance or attenuate the structural complexity in different regions, a second inversion can be carried out using an objective function consisting of both ϕ_{ms} and ϕ_{mv}. The model obtained by minimizing ϕ_{ms} can then be used in this inversion as an initial model. The available prior information can be incorporated into the second inversion by forming a reference model and 3-D weighting functions, w_s, w_x, w_y, w_z.

We now invert the same data by using $m = \ln(\kappa)$ as the model. It is not possible to incorporate a zero susceptibility as the reference model, so we minimize an objective function consisting of ϕ_{mv} with the reference model removed. The same depth weighting is applied to all terms of ϕ_{mv}. Since $\kappa = e^m$, the positivity of the susceptibility is ensured without invoking the transformation of variables. The result is shown in Figure 10a. This is a cross-section at x = 500 m and plotted on a logarithmic scale in accordance with the model used in the inversion. The inverted susceptibility shows the presence of the dipping anomaly as a broad region of high susceptibility. However, the interpretation based upon such a model can be complicated by the variations of susceptibility that are small and have little effect on the surface data. We have replotted the cross-section on a linear scale in Figure 10b and the anomalous region is now delineated more clearly. Its top portion indicates the tabular body and defines the depth to the

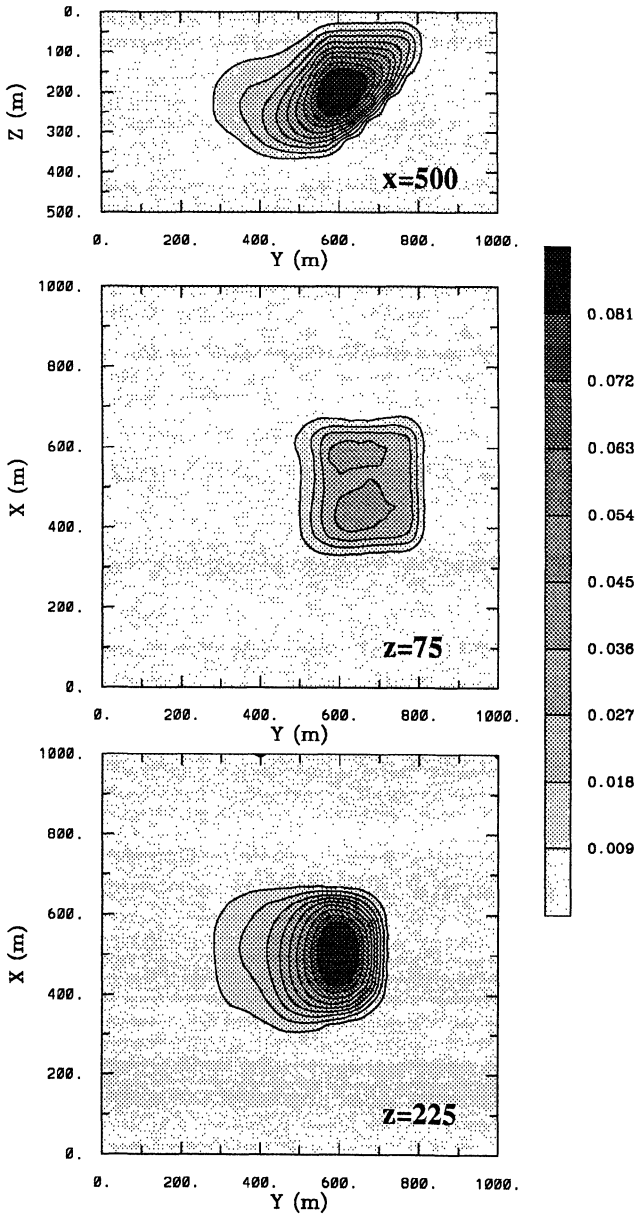


FIG. 9. The model derived from inverting the slab model data in Figure 2 by minimizing the model objective function having both ϕ_{ms} and ϕ_{mv}. The same depth weighting is used. This model appears to be smoother and has a smaller amplitude than that in Figure 8.

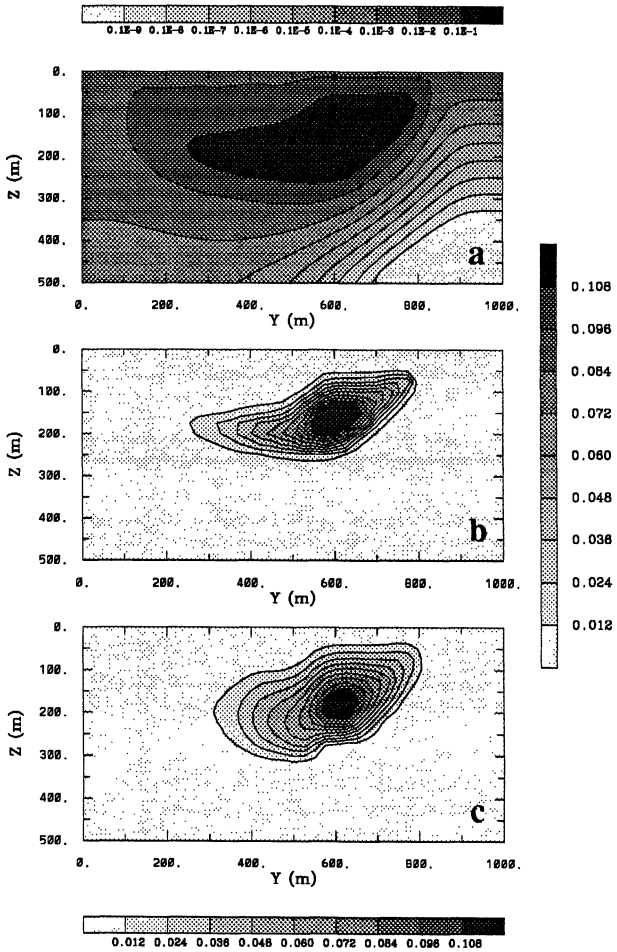


FIG. 10. The model obtained from inverting the data shown in Figure 2 by using $m = \ln(\kappa)$ as the model and minimizing ϕ_{mv} with the reference model removed. The inverted logarithmic susceptibility in cross-section at x = 500 m is shown in (a) and it is replotted on a linear scale in (b). As a comparison, the result obtained by using $m = \kappa$, and the same objective function is shown in (c).

top and dipping angle. The anomaly terminates at a shallower depth than the true model and has a nearly horizontal extension to the left. As an exact comparison, Figure 10c is the susceptibility model obtained by minimizing ϕ_{mv} but using $m = \kappa$ as model and invoking the positivity. This is a smoother model and exhibits more gradual changes in the susceptibility. It has a slightly deeper extent than the model in Figure 10b. With the exception of details toward the bottom, however, both models provide almost the same information about the anomalous susceptibility region. It might be concluded that inversion using either linear or logarithmic susceptibility is viable for practical applications. However, we note that the presentation in Figure 10b is inconsistent with the model used in the inversion. Since the inverted susceptibility is easier to interpret on a linear scale as demonstrated here, and since the magnetic data are linearly related to the susceptibility, we generally prefer to work with the susceptibility κ as the model in the inversion.

As the second example we invert the total field anomaly data produced by a slightly more complicated model and with two different inducing field directions. The true model is shown in Figure 11 in the same format as before. It is a dipping slab having its top and bottom portions offset to simulate the result of a normal faulting. The faulted slab strikes north. The data from this model, when the inducing field has a direction of I = 45° and D = 45°, are shown in Figure 12. Again Gaussian noise has been added to the data. The inversion minimizes an objective function consisting of ϕ_{ms} and ϕ_{mv} that have the same depth weighting and nonlinear mapping as used to produce the results in Figure 9. Figure 13 displays the recovered model in three slices. It shows two distinct anomalous regions of susceptibility that correspond to those in the true model. The dipping structure is evident from the top block. On plan view, the strike direction and the strike length of the anomaly are also well recovered.

When the inducing field direction is I = 0° and D = 45°, the surface anomaly with added Gaussian noise is that shown in Figure 14. Carrying out the inversion using an identical model objective function generates the model shown in Figure 15. It is similar to the model shown in Figure 13, which is recovered under an inducing field at 45° inclination. Again, the two separate blocks, the dipping direction, and the length and direction of the strike, are all reasonably recovered. This is a positive result in that, although the surface anomalies have very different expressions under different inducing field directions, the inversion algorithm is able to consistently recover the source structure. Moreover, the algorithm had no difficulty in inverting data generated from an inducing field having zero inclination; such data often pose problems in interpretations that include a reduction to pole.

We emphasize that positivity has played a pivotal role in all the inversions. Magnetic data generally have regions of nega-

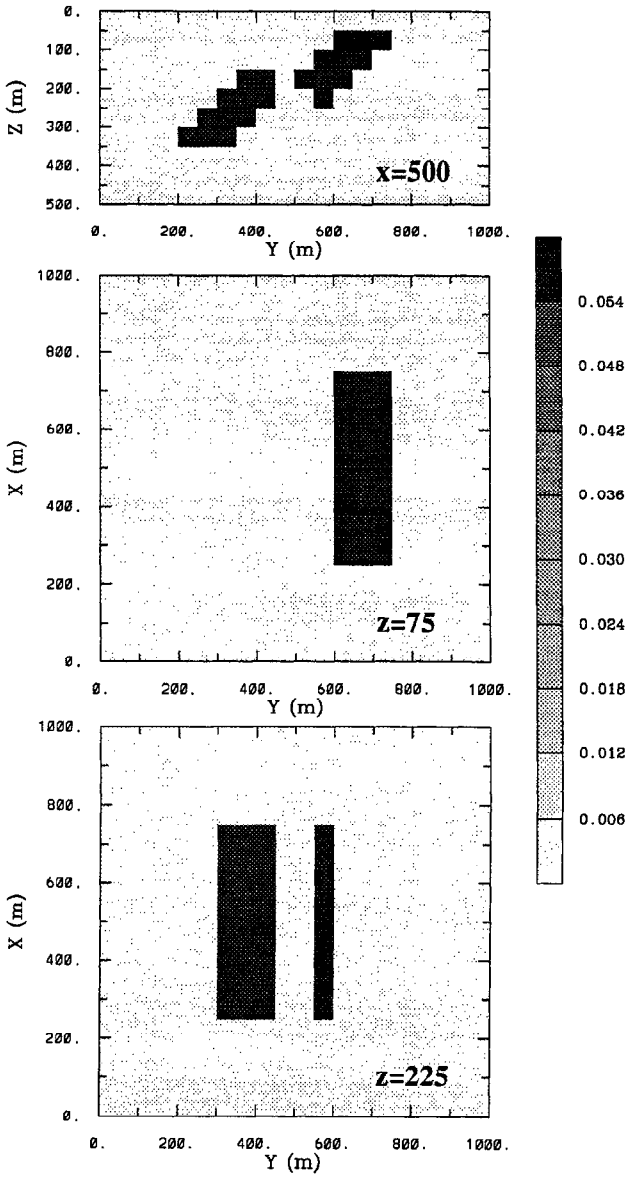


FIG. 11. The second synthetic test example. The top and bottom portions of the anomalous susceptibility are offset to simulate a norm fault structure. It also has a large strike length in the north direction.

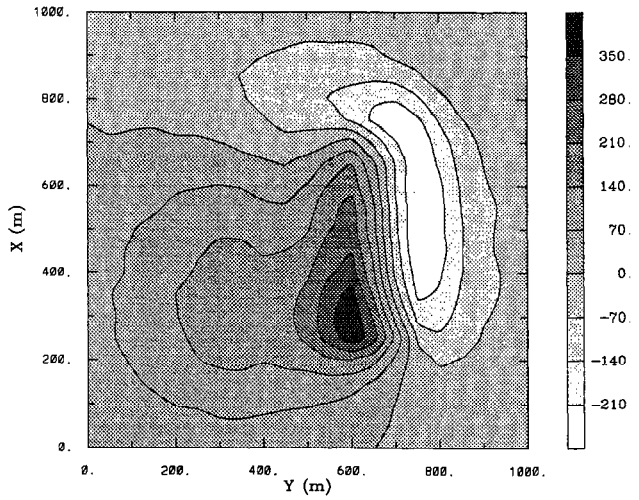


FIG. 12. The surface total field anomaly produced by the faulted slab in Figure 11, under an inducing field at I = 45° and D = 45°. Uncorrelated Gaussian noise is again added to the data.

tive values that result from dipping bodies or inclined inducing field, or both. Without positivity, the constructed susceptibility is often negative and the dipping bodies appear more vertical. Recovery of correct dip and, to some extent, depth to the top of the anomalous body, are often the result of invoking positivity. Once the positivity is imposed, it is no longer true that an equivalent stratum that reproduces the data exists at any depth. Therefore, cells of anomalous susceptibility cannot be placed arbitrarily close to the surface, and no equivalent source can be constructed with negative susceptibilities. This restricts the class of admissible models and, consequently, reduces the nonuniqueness.

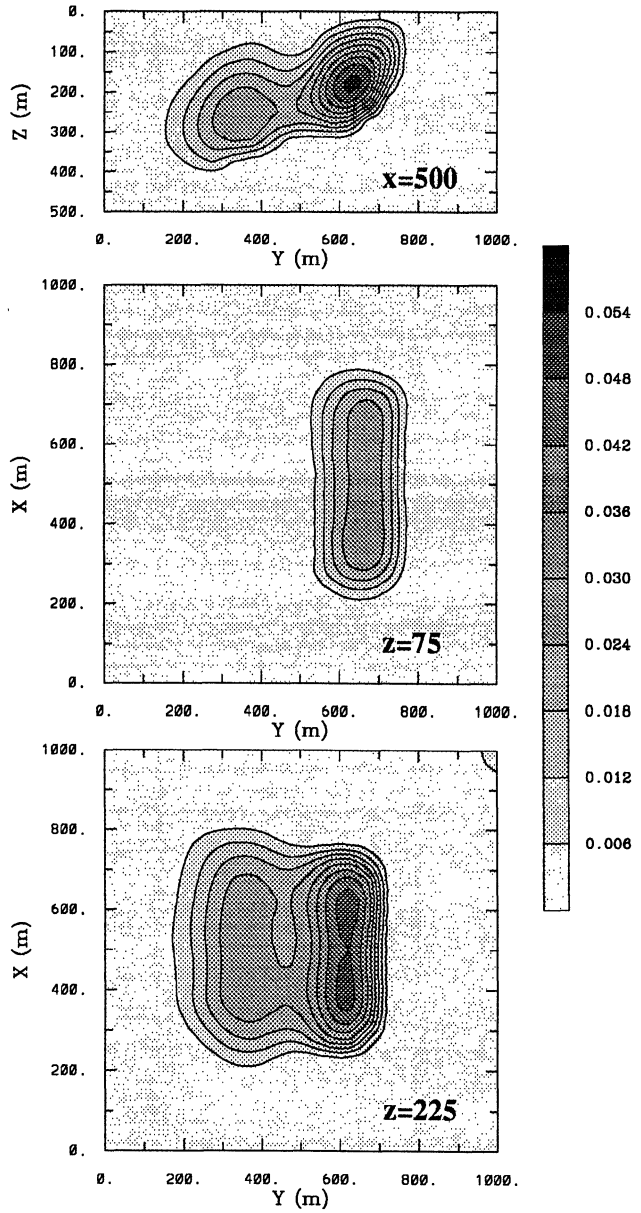


FIG. 13. The susceptibility model recovered from the data shown in Figure 12. It is seen that both the top and bottom block of the true model are recovered and the strike direction and length are well defined.

FIELD EXAMPLE

As the final example, we invert field data taken over a copper-gold porphyry deposit at Mt. Milligan in central British Columbia. The host rocks for the deposit are early Mesozoic volcanic and sedimentary rocks and contain intrusive monzonitic rocks that have accessory magnetite. Porphyry-style alteration and copper-gold mineralization are contemporaneous with the intrusive events. The copper and gold are known to be concentrated in the potassic alteration assemblage, which is mainly around the contact of the monzonite intrusions and may extend outward and into fractured volcanic rocks. Among other minerals, magnetite is one of the strong indicators of the potassic alteration. Ground magnetic data are acquired in the region at 12.5-m spacing along lines in the east direction and spaced 50 m apart. Our study of the data set has focused on a 1.2 km x 1 km area, which covers a large monzonite body known as the MBX stock and contains a reasonably isolated set of magnetic anomalies. Fairly detailed information about the geology is available through a major drilling program, but no susceptibility logs were available.

Magnetic data from a larger area were first upward continued to 20 m. A regional field was then defined and removed from the upward continued data. The continuation operation suppresses the noise in the data and also facilitates the discretization of the topographic surface for the model so that all observation points remain above the discretized surface. Although the original data were collected at 12.5-m spacing, we use the data at 25-m spacing. This yields 1029 data points at varying elevations. Figure 16 shows the data contoured according to their horizontal locations. The direction of the inducing field is $I = 75°$ and $D = 25.73°$. Several major magnetic highs are observed in the map. However, the influence of anomalies adjacent to the map is also visible along the edges. We choose a model domain that is horizontally larger than the data area, coincides at the top with the highest point on the topographic surface, and extends to 450-m depth. The model is discretized horizontally at a 25-m interval beneath the area of data. In the

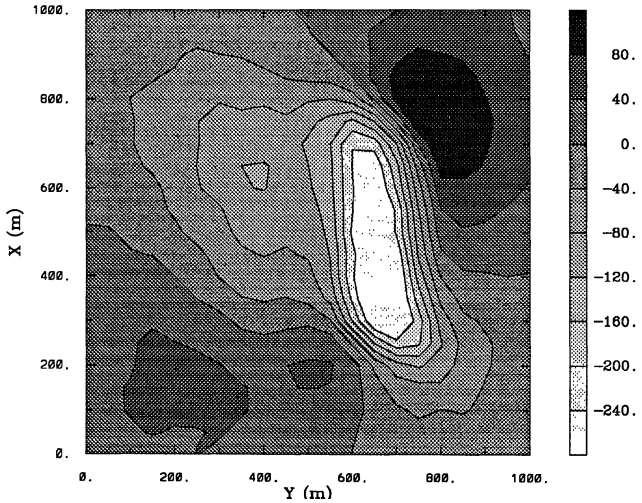


FIG. 14. The surface total field anomaly produced by the faulted slab in Figure 11 under an inducing field at $I = 0°$ and $D = 45°$. Uncorrelated Gaussian noise is added to the data.

vertical direction, the first 100 m is divided at a 12.5-m interval so that the surface can be adequately discretized onto the model mesh. Below the depth of 100 m, an interval of 25 m is used. This results in a mesh with 52 x 44 x 22 cells. Once the mesh is defined, the topography is discretized onto it. The 43 428 cells below this surface define the susceptibility model, and the inverse problem is therefore formalized by inverting 1029 data to recover the susceptibilities in those cells. The depth weighting is referenced to the top of the model domain. Each datum is assumed to have an error whose standard deviation is equal to 5% of its magnitude plus 10 nT. The error estimate includes not only the repeatability of the instrument reading but also the geological noise and errors introduced by the inaccurate recording position and by separating the anomalous field from the initial total field measurements. One hundred subspace vectors generated by dividing the data map into small subareas are used in the inversion. We use a nonlinear mapping with $\kappa_b = 0.0002$ and $\kappa_1 = 0.02$. The recovered model is shown in Figure 17 as one plan-section and three cross-sections. From the plan-section, two concentrated susceptibility highs are observed in the central region. Surrounding them are three linear anomalies trending northeast. In the cross-sections, the major anomalies are seen at moderate depths but there is considerable variation in the depth to the top. There are also smaller anomalies extending to the surface. In general, there are more detailed structures near the surface and the model becomes increasingly smooth at greater depths. As required by the objective function, there is no excessive structure associated with each unit of high susceptibility region. Comparison with drill logs indicates that the recovered magnetic susceptibility highs are mostly associated with the monzonite intrusions and with faults or fracture zones. Figure 18 compares the recovered susceptibility model with the geology (Cam DeLong, personal communication) in the cross-section at x = 600 m. The large susceptibility high is spatially well-correlated with the MBX stock and reflects the initial magnetite content in the intrusion. Two smaller susceptibility highs are present east of the stock. The high at y = 650 m coincides with the boundary of stock and porous trachytic units while the high at y = 900 m coincides with the upper portion of the Rainbow dyke. These are locations of the most intensive potassic alterations and the susceptibility highs are indicative. of the magnetite produced by the alteration process. Over all, this is a rather encouraging result.

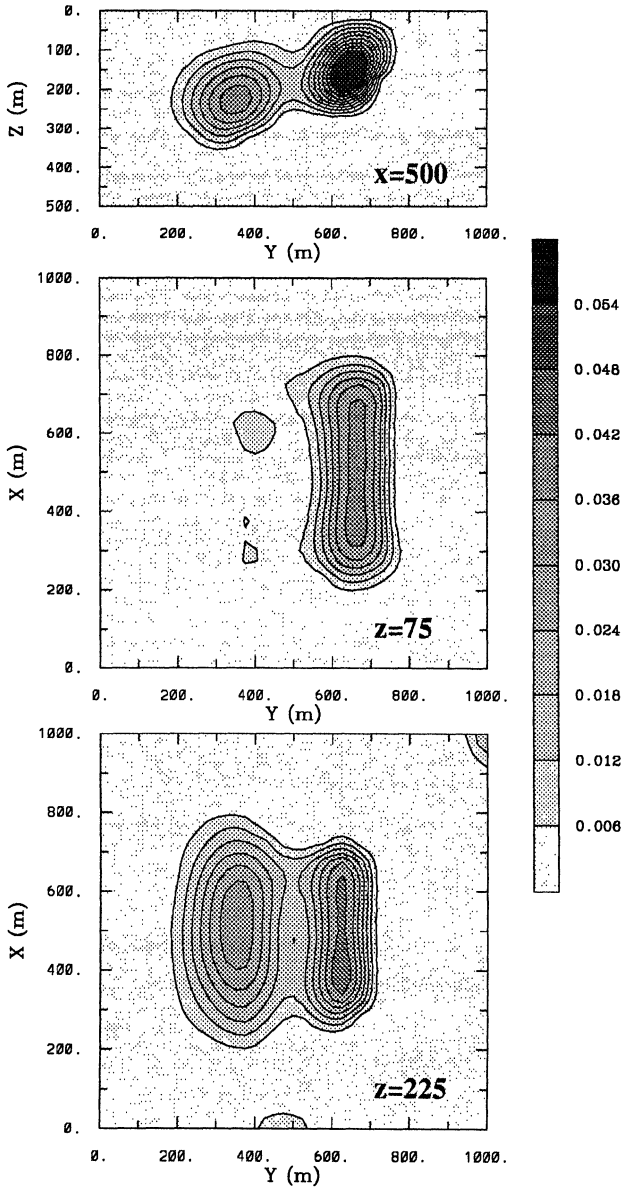


FIG. 15. The susceptibility model recovered from the data shown in Figure 14. This model is similar to that shown in Figure 13.

CONCLUSION

We have developed an algorithm to invert surface magnetic data for general 3-D susceptibility distributions. Although we have illustrated the algorithm using examples on the scale pertinent to mining applications, the method is general and applicable to problems on different scales ranging from environmental to regional investigations. To overcome the inherent nonuniqueness, we obtain the solution by minimizing a

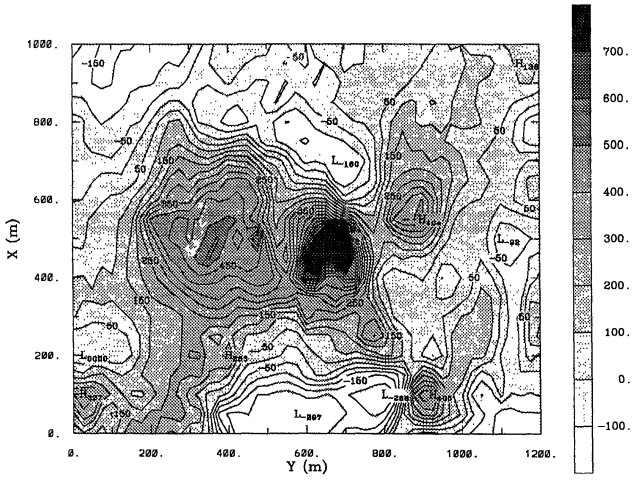


FIG. 16. The extracted total field anomaly from ground magnetic data at Mt. Milligan Copper-gold porphyry deposit. The data are contoured according to their horizontal locations in this map, although thev are at different elevations.

specific objective function of the model. Our model objective function has the ability to incorporate prior information into the inversion via a reference model and 3-D weighting functions. A crucial feature of the objective function is a depth weighting function that counteracts the natural decay of the kernel functions. The parameters of the depth weighting depend upon the discretization of the model but are easily calculated. The minimization is carried out using a subspace technique that reduces the computational effort and allows the positivity constraint of susceptibility to be incorporated. Both susceptibility and logarithmic susceptibility can potentially be used as the model in the inversion. Since the data are linearly related to susceptibility, and since usually absolute values of susceptibility are required for interpretation rather than relative values, especially in regions of very low susceptibility, we have generally chosen to work with susceptibility. To suppress the noise from small magnetic bodies near the surface, we recommend in general that the data be upward continued to a height comparable with the width of the surface cell before inversion.

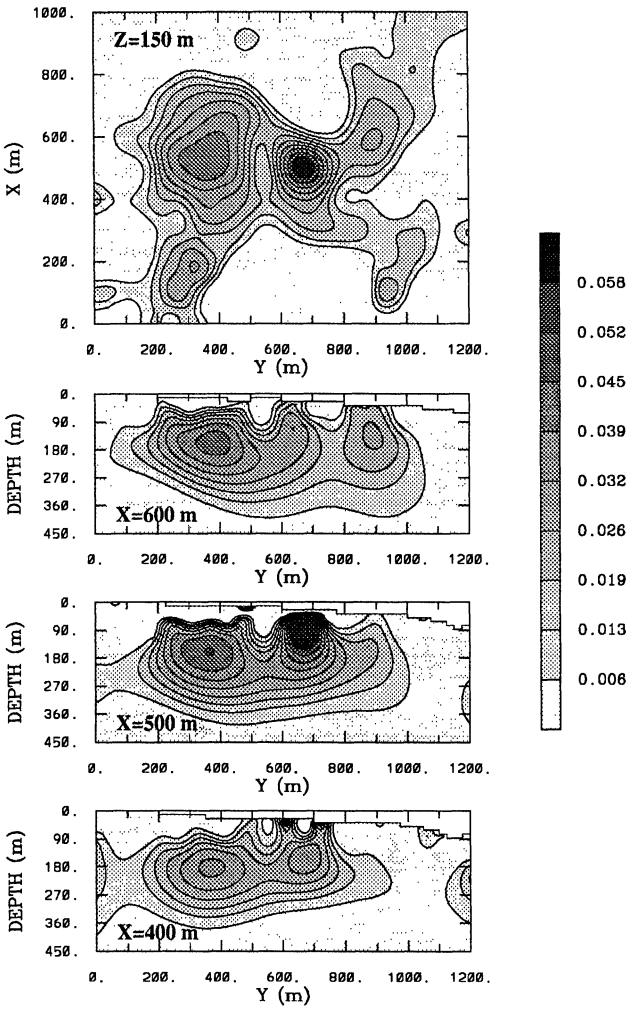


FIG. 17. The recovered susceptibility model shown in one plan-section and three cross-sections. The plan-section is at the depth of 150 m and the three cross-sections are at x = 600,500, and 400 m, respectively.

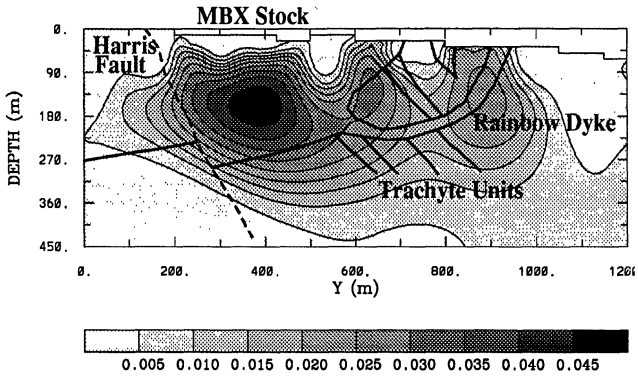


FIG. 18. Comparison of the recovered susceptibility model in a cross-section (x = 600) with the geology for the Mt. Milligan deposit. The susceptibility high within the MBX stock reflects the initial magnetite in the intrusive while the susceptibility highs near the Rainbow dyke are related to the magnetite produced by potassic alteration.

Applications of our inversion to synthetic data sets have produced models representative of the true structures and demonstrated the ability of the algorithm to construct consistent models at different magnetic latitudes. Inversion of field data has produced a susceptibility model that is consistent with the known geology and mineralization information. These results represent an encouraging conclusion: although the inversion of magnetic data seems impossibly nonunique when one has a large number of cells, inversions using a properly designed model objective function can produce susceptibility distributions that yield meaningful geologic information.

ACKNOWLEDGMENTS

This work was supported by an NSERC IOR grant and an industry consortium "Joint and Cooperative Inversion of Geophysical and Geological Data." Participating companies are Placer Dome, BHP Minerals, Noranda Exploration, Cominco Exploration, Falconbridge, INCO Exploration & Technical Services, Hudson Bay Exploration and Development, Kennecott Exploration Company, Newmont Gold Company, Western Mining Corporation, and CRA Exploration Pty.

REFERENCES

Bhattacharyya, B. K., 1964, Magnetic anomalies due to prism-shaped bodies with arbitrary magnetization: Geophysics, **29,** 5 17-53 1.

——— 1980, A generalized multibody model for inversion of magnetic anomalies: Geophysics, **45,** 255-270.

Green, W. R., 1975, Inversion of gravity profiles by use of a Backus-Gilbert approach: Geophysics, **40,** 763-772.

Guillen, A., and Menichetti, V., 1984, Gravity and magnetic inversion with minimization of a specific functional: Geophysics, **49,** 1354-1360.

Last, B. J., and Kubik, K., 1983, Compact gravity inversion: Geophysics, **48,** 713-721.

Oldenburg, D. W., and Li, Y., 1994, Subspace linear inversion methods, Inverse Problems, **10,** 915-935.

Rao, D. B., and Babu, N. R., 1991, A rapid methods for three-dimensional modeling of magnetic anomalies: Geophysics, **56,** 1729-1737.

Wang, X., and Hansen, R. O., 1990, Inversion for magnetic anomalies of arbitrary three-dimensional bodies: Geophysics, **55,** 1321-1326.

Zeyen, H., and Pous, J., 1991, A new 3-D inversion algorithm for magnetic total field anomalies: Geophys. J. Int., **104,** 583-591.

APPENDIX

MODEL OBJECTIVE FUNCTION

Our inversion method uses a model objective function of the form

$$\phi_m(m) = \alpha_s \int_V w_s\{w(z)[m(\mathbf{r}) - m_0]\}^2\, dv + \alpha_x \int_V w_x \left\{\frac{\partial w(z)[m(\mathbf{r}) - m_0]}{\partial x}\right\}^2 dv + \alpha_y \int_V w_y \left\{\frac{\partial w(z)[m(\mathbf{r}) - m_0]}{\partial y}\right\}^2 dv + \alpha_z \int_V w_z \left\{\frac{\partial w(z)[m(\mathbf{r}) - m_0]}{\partial z}\right\}^2 dv. \quad \text{(A-1)}$$

The numerical evaluation of this functional is carried out by introducing the model mesh and evaluating all terms using a finite-difference approximation. The discretized model objective function has the form

$$\phi_m(\mathbf{m}) = (\mathbf{m} - \mathbf{m}_0)^T(\mathbf{W}_s^T\mathbf{W}_s + \mathbf{W}_x^T\mathbf{W}_x + \mathbf{W}_y^T\mathbf{W}_y + \mathbf{W}_z^T\mathbf{W}_z)(\mathbf{m} - \mathbf{m}_0) \equiv (\mathbf{m} - \mathbf{m}_0)^T\mathbf{W}_m^T\mathbf{W}_m(\mathbf{m} - \mathbf{m}_0) \quad \text{(A-2)}$$

Each component matrix can be written as the product of three individual matrices and one oefficient. That is,

$$\mathbf{W}_i = \alpha_i \mathbf{S}_i \mathbf{D}_i \mathbf{Z}, \qquad i = s, x, y, z, \quad \text{(A-3)}$$

where $\mathbf{S}_i$ are diagonal matrices representing the spatially dependent 3-D weighting functions, $\mathbf{D}_i$ are the finite-difference operators for each component, and $\mathbf{Z}$ is a diagonal matrix representing the discretized form of depth weighting function $w(z)$.

The elements of $\mathbf{S}_i$ are given by $\sqrt{w_i}$. They are defined over each cell for $\mathbf{S}_s$, and over each interface between adjacent cells in the respective directions for $\mathbf{S}_x$, $\mathbf{S}_y$, and $\mathbf{S}_z$. $\mathbf{D}_s$ has elements $\sqrt{\Delta x \Delta y \Delta z}$ on its diagonal, where Ax, Ay, and Δz are the cell width. The matrix $\mathbf{D}_x$ has two elements $\pm\sqrt{\Delta y \Delta z/\delta x}$ in each row, where δx is the distance between the centers of cells adjacent in the x - direction. Similarly, $\mathbf{D}_y$ and $\mathbf{D}_z$ have elements $\pm\sqrt{\Delta x \Delta z/\delta y}$ and $\pm\sqrt{\Delta x \Delta y/\delta z}$, respectively, where δy and δz are the distances between centers of adjacent cells in the y- and z - directions. Once the mesh is defined and all weighting functions, w_s, w_x, w_y, w_z, and $w(z)$ are chosen, equation (A-3) is evaluated straightforwardly and $\mathbf{W}_m^T\mathbf{W}_m$ is formed.

New enhancement filters for geological mapping

Zhiqun Shi*
Encom Technology Australia
zhiqun.shi@encom.com.au

Graham Butt
Encom Technology Australia
graham.butt@encom.com.au

SUMMARY

Two types of filters have been developed for the purpose of enhancing weak magnetic anomalies from near-surface sources while simultaneously enhancing low-amplitude, long-wavelength magnetic anomalies from deep-seated or regional sources. The Edge filter group highlights edges surrounding both shallow and deeper magnetic sources. The results are used to infer the location of the boundaries of magnetised lithologies. The Block filter group has the effect of transforming the data into "zones" which, similar to image classification systems, segregate anomalous zones into apparent lithological categories. Both filter groups change the textural character of a dataset and thereby facilitate interpretation of geological structures.

The effect of each filter is demonstrated using theoretical model studies. The models include both shallow and deep sources with a range of magnetisations. Comparative studies are made with traditional filters using the same theoretical models. In order to simulate real conditions, Gaussian noise has been added to the model response. Techniques for noise reduction and geological signature enhancement are discussed in the paper.

The new approaches are applied to actual magnetic survey data covering part of the Goulburn 1:100 000 scale map sheet area, New South Wales. Some new geological inferences revealed by this process are discussed

Key words: Enhancement filters, magnetic sources, geological mapping.

INTRODUCTION

High-resolution aeromagnetic survey data represent a rich source of detailed information for mapping surface geology as well as for mapping deep tectonic structure. Traditional enhancement techniques, such as first vertical and horizontal derivatives (1VD, 1HD), analytic signal (AS), and high-pass in-line or grid filters are used in enhancing magnetic anomalies from near-surface geology.

In recent years the potential field tilt filter has been introduced (Miller and Singh, 1994) and it has achieved recognition for its value in the analysis of potential field data for structural mapping and enhancement of both weak and strong magnetic anomalies (Verduzco *et al*, 2004). The total horizontal derivative of the TMI reduced to the pole is also widely used for detecting edges or boundaries of magnetic sources (Cordell and Grauch, 1985; Blakely and Simpson, 1986; Phillips, 1998).

Several disadvantages pertain to the use of these traditional filters. They often only diffusely identify source location and boundaries, particularly in colour image presentations. They usually emphasise short wavelength anomalies at the expense of signal from deeper magnetic sources and the range of amplitudes remaining in the filtered output may dominate the source boundary information being sought. In addition, some traditional filters emphasise noise with resultant impact on the interpretation of source boundaries.

This paper identifies new processes which have been developed to address these disadvantages and provide output which can improve map-based interpretations.

Unless otherwise stated, all filters have been operated on TMI data reduced to the pole (RTP).

METHOD AND RESULTS

Theoretical Model Testing

A theoretical 2D grid of total magnetic intensity (TMI) computed at the surface was created by forward 3D modelling of the TMI response from a set of theoretical magnetic sources having variable width, strike extent, depth, depth extent (DE), dip, magnetic susceptibility and strike azimuth. A list of these parameters is presented in Table 1. In two of the sources, remanence was simulated using negative magnetic susceptibility. The TMI of the theoretical models was computed at a geomagnetic inclination of -60 degrees using a notional east–west line spacing of 200 m and a grid cell size of 40 m. The TMI grid was then reduced to the pole (RTP) (Figure 1).

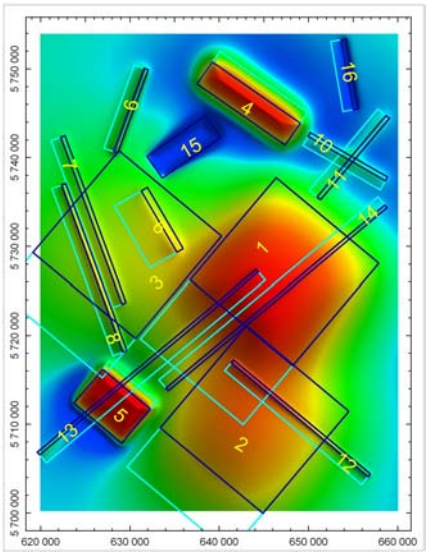


Figure 1. RTP image derived from multiple theoretical 3D magnetic sources, shown as wire frame outlines

A set of traditional filters was operated on the theoretical RTP grid. They include AS, 1VD, modulus of horizontal derivatives (MS) and Tilt and the results are presented in

Figure 2. The output grids variously show discontinuous trending (crossed sources in upper right of AS image), diffuse, weak edges (deep source in centre right of the MS image) and lack of precise source edge definition (1VD and Tilt).

Model Label	Depth (m)	Width (m)	DE (m)	Dip (deg)	Magnetic Susceptibility (SI)	Strike Length (m)	Azimuth (deg)
1	4000	15000	15000	120	0.010	15000	-050
2	6000	15000	10000	120	0.010	15000	-050
3	10000	15000	10000	120	0.010	15000	-050
4	1000	3000	4000	70	0.010	12000	-055
5	500	5000	2000	60	0.010	7000	-050
6	1000	800	2000	150	0.005	8000	-030
7	600	500	2000	120	0.001	20000	-020
8	200	500	2000	120	0.001	20000	-020
9	500	500	2000	120	0.003	10000	020
10	1000	500	2000	120	0.003	10000	-060
11	1000	500	2000	120	0.003	12000	040
12	200	400	2000	120	0.001	20000	-050
13	500	400	1000	40	0.002	32000	050
14	500	400	1000	140	0.001	32000	050
15	600	3000	4000	90	-0.002	8000	055
16	400	600	2000	120	-0.010	8000	-010

Table 1. List of parameters of theoretical magnetic sources

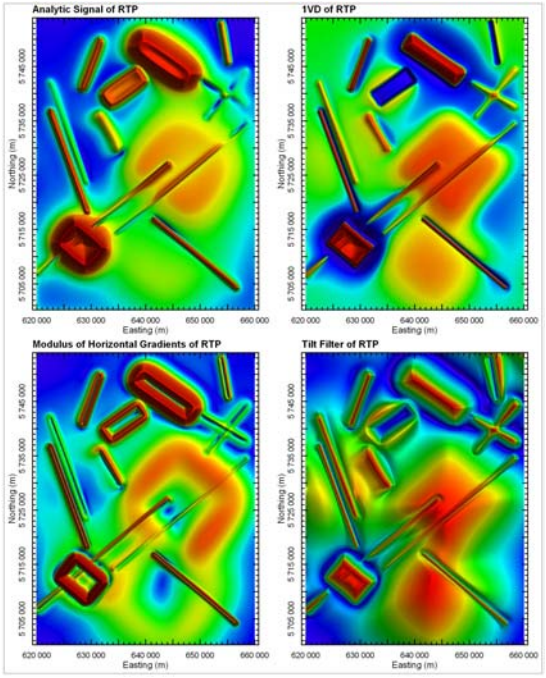


Figure 2. Comparison of enhancement filters of RTP: AS, 1VD, MS and Tilt filter. The models used are those depicted in Figure 1.

Edge Filters

The first avenue of development was to increase the sharpness of the anomalies used to map the edge of the magnetic sources. The MS grid yields anomaly peaks over the source edge locations, whereas these edges coincide with gradients in the 1VD, Tilt and AS filtered outputs. None of these filters produces easily interpreted edges in image form when the sources are weakly magnetised or are deep.

A new linear, derivative-based filter termed the ZS-Edgezone filter has been developed to improve edge detection in these situations. Its effect is shown in Figure 3 using the same theoretical models discussed earlier. The advantages of the filter are greatly increased anomaly sharpness over source edges and compression of the amplitude range so that differences in the original TMI amplitudes do not persist to dominate the edge interpretation. This has the ancillary effect that the method can be modified to provide automated edge conversion to vectors for use in GIS systems.

Although this filter significantly improves the precision of edge determination, it is subject to normal potential field limitations which determine that source edges cannot be resolved where the source is narrow relative to its depth. The filter also can produce a "halo" type artefact due to superposition of the response of a limited depth extent shallow source (Figure 1, Model 6) on that of deeper sources. A similar "halo" effect can be seen around the edges of remanently magnetised Model 15, also in Figure 1.

The ZS-Edge filter (Figure 4) has also been developed to map source edges. This filter differs from the ZS-Edgezone filter in that a greater contribution of the TMI anomaly amplitude over the source is retained, thereby improving anomaly characterisation at the expense of edge sharpness.

Both these filters produce edges which migrate down-dip towards the deepest edge of the source. This effect produces anomaly asymmetry that can assist interpretation of dip, although this effect is more pronounced for the ZS-Edge filter than for the ZS-Edgezone filter. Down-dip source extensions are depicted in cyan in Figure 1.

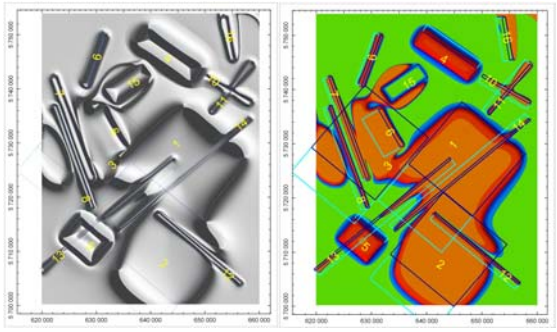


Figure 3. Anomaly edge and block enhancements using the ZS-Edgezone (left) and ZS-Block filters (right). Model positions are shown using wire frames.

Block Filters

In attempting to improve edge detection filters, an obvious progression is to highlight the magnetic regions whose edges have been mapped. To do this, a set of filters called "block" filters has been developed.

The Block filter group has the effect of transforming the potential field data into "zones" which, similar to image classification systems, segregate anomalous zones into apparent lithological categories. These filters can be imported for use in image classification systems or displayed in RGB space with other grids for empirical classification purposes.

The block filters, like the edge filters, are linear, derivative-based filters which use a combination of derivative and amplitude compression techniques to render the magnetic data into regions whose edges are sharply defined and whose amplitudes have a reduced range in comparison to the original TMI.

The ZS-Block filter (Figure 3) and the ZS-Plateau filter (Figure 4) depict the magnetic data as a 2D plan of apparent magnetic source distribution. Artefacts may occur as discussed for the edge filters.

The choice of ZS-Block, ZS-Plateau or ZS-Area filters will depend on the data characteristics of each magnetic survey and on the end-use requirement. The ZS-Plateau filter, for example, yields less variation in amplitude "texture" over a magnetic unit that either the ZS-Block or ZS-Area filters.

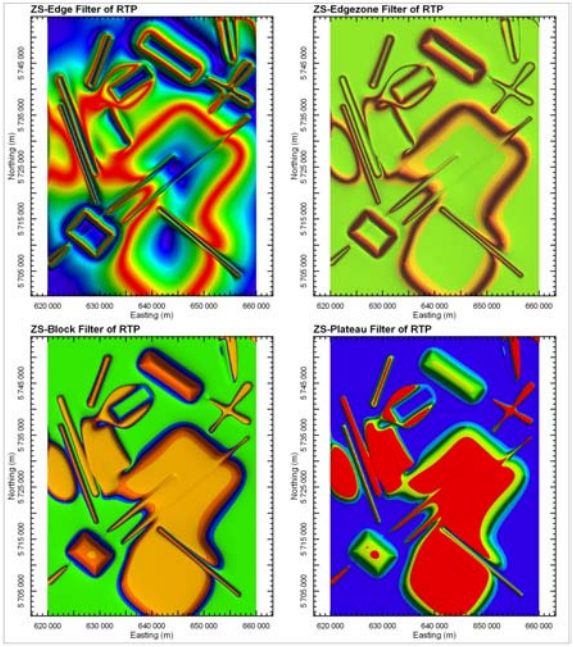


Figure 4. Comparison of ZS-Edge, ZS-Edgezone, ZS-Block and ZS-Plateau filtered outputs of RTP data

Effects of Noise

The influence of noise on the operation of these enhanced grids was tested by adding a large component of noise to the theoretical TMI profile data. This noise had a Gaussian distribution with a standard deviation equal to ten percent of the TMI standard deviation. The noise-modified TMI profile data were then de-spiked using a non-linear technique. Both the noise-affected and the de-spiked TMI data were then gridded and converted to RTP. The RTP data were then processed both with the traditional and newly developed filters.

Figure 5 shows the effect of the noise on the computations. The image of the noise-affected 1VD RTP data (top right) shows that weak and deep sources have been severely masked by the noise. Significant improvement can be achieved by using de-spiked data (lower left) or by low-pass grid filtering — for example, using an upward continuation filter (lower right).

Figure 6 shows that if real data with significant noise is encountered, a standard de-spiking or low-pass smoothing procedure may be used to achieve successful application of both the traditional and newly developed filters.

Figure 6 also depicts the use of enhanced outputs in RGB space to provide examples of how the combination of amplitude information (red colour) with edge information (green and blue colours) can be used to highlight source boundaries and remanence in a single image.

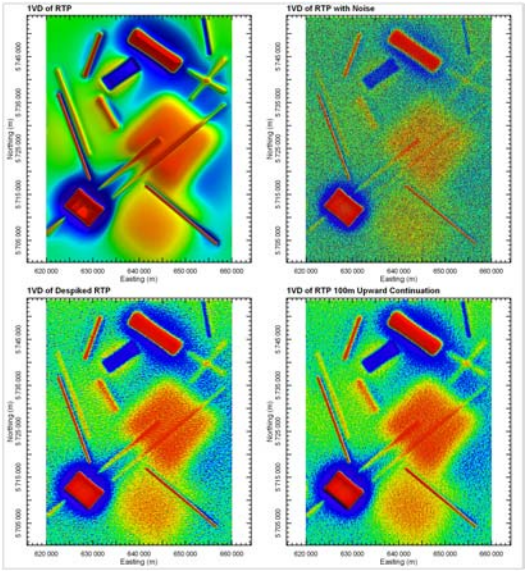


Figure 5. Comparison of 1VD of original model RTP data (top left) with noise-affected RTP data (top right) and noise-reduced RTP data (lower images)

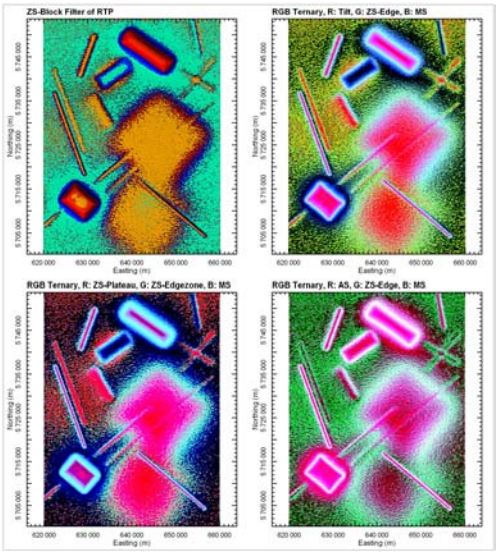


Figure 6. ZS-Block filter using noise-reduced RTP data (top left) and examples of filter combinations in RGB space using noise-reduced RTP data

Application to Field Data, Goulburn 1:100 000 Scale Map Sheet Area, New South Wales

Both the traditional and new enhancement filters were applied to test their suitability for geological definition to airborne magnetic survey data over the Goulburn 1:100 000 scale map sheet area (Johnson *et al,* 2003). These data were acquired as part of a joint program between the NSW Department of Mineral Resources and Geoscience Australia, with 250 m–spaced east–west flightlines. The magnetometer sensor occupied a nominal terrain clearance of 80 m. This dataset was selected since new detailed geological mapping had been recently completed. All the enhancements have been computed using TMI data reduced to the pole.

Figure 7 shows a comparison of part of the Goulburn 1:100 000 map sheet area surface geology with the ZS-Area

filter output. In the area surrounding location C, the ZS-Area filter transforms the magnetic data into separate magnetic units, which comprise the Devonian Bindook Volcanic Complex. The magnetic regions correlate closely with mapped andesites (Dkqa–cream coloured unit in Figure 7) whilst the intervening less-magnetic units correlate with rhyolitic ignimbrites (Dkqy–red unit in Figure 7)

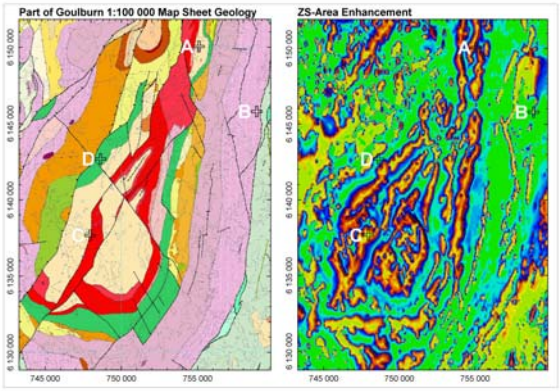


Figure 7. Comparison of geology and ZS-Area enhancement over the Bindook Volcanic Complex

Figure 8 displays some of the advantages of the edge detection filters. At location A, ambiguity concerning the continuity of Quialigo Formation units (cream and red units in Figure 7) is resolved by the ZS-Edgezone filter. At location B, a subtle lineament is confirmed, whilst at location D, the extent of the Bullamalita Conglomerate (green unit in Figure 7) is clearly mapped by the ZS-Edge filter. Structural breaks are often more easily interpreted using these transforms, for example, immediately southwest of location D.

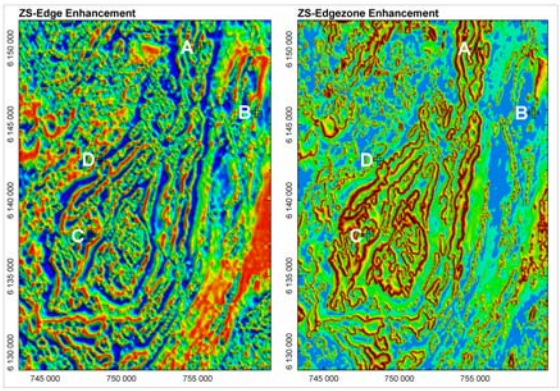


Figure 8. Comparison of ZS-Edge and ZS-Edgezone enhancements over the Bindook Volcanic Complex

Figure 9 shows standard RTP and Tilt transforms over the same area for reference.

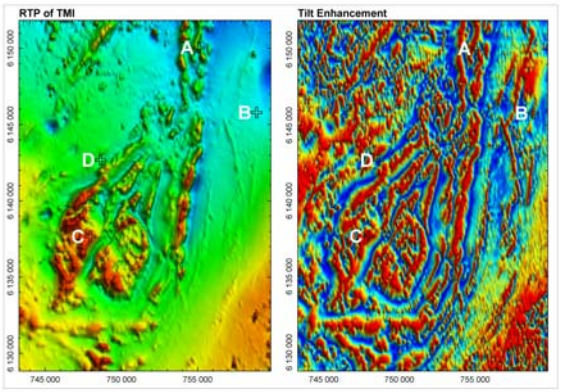


Figure 9. Comparison of RTP and Tilt filters over the Bindook Volcanic Complex

CONCLUSIONS

Traditional filters used to enhance magnetic data, including the more recently developed potential field tilt filter, are currently used to assist in determination of the location and extent of magnetic units.

Newly developed derivative-based filters may be used to improve the precision of source edge detection and, by extension, the determination of the spatial extent of magnetic units. These filters are demonstrated to perform successfully on both strongly magnetised features as well as on weakly magnetised or deep magnetic features. Artefacts may result particularly where anomaly superposition occurs.

The impact of noise in real data may be accommodated by these new methods provided noise-reduction techniques are employed.

The new filter outputs may be used as part of regional or detailed geological mapping projects, including in classification systems or in RGB space, to improve lithological discrimination and mapping.

The speed of magnetic unit mapping can be considerably increased through reliance on edge detection filters. Further improvements in mapping speed can be envisaged through automated conversion of edge anomalies to vector files.

ACKNOWLEDGMENTS

The authors would like to acknowledge the New South Wales Department of Mineral Resources for permission to use aeromagnetic and geological data from the Goulburn 1:100 000 map sheet area and helpful comments by David Robson during the project.

The authors wish to acknowledge Encom Technology for permission to publish the results of research into the proprietary filters used in this paper. The 3D modelling was carried out using Encom ModelVision Pro software, whilst processing and data visualisation were accomplished using Geosoft OASIS montaj and Encom Geoscape.

REFERENCES

Blakely, R. J. and Simpson, R. W., 1986, Locating edges of source bodies from magnetic or gravity anomalies, Geophysics, 51, 1494-1498.

Buckingham, A.J, Dentith, M.C., and List, R.D, 2003, Towards a system for content-based magnetic image retrieval: Exploration Geophysics, 34, 195-206.

Cordell, Lindrith, and Grauch, V.J.S., 1985, Mapping basement magnetization zones from aeromagnetic data in the San Juan Basin, New Mexico pp.181-197. In Hinze, W.J., ed,. The utility of regional gravity and magnetic maps: Society of Exploration Geophysicists,

Johnson A.J. *et al.*, 2003, Goulburn 1:100 000 Sheet 8828 Geology Map, New South Wales Department of Mineral Resources.

Miller, H.G., and Singh V., 1994, Potential field tilt — a new concept for location of potential field sources: Journal of Applied Geophysics, 32, 213-217.

Phillips, J.D., 1998, Processing and interpretation of aeromagnetic data for the Santa Cruz Basin–Patagonia Mountains Area, South-Central Arizona: United States Geological Survey Open-File Report 02-98.

Verduzco, B., Fairhead, J. D., Green, C. M., and MacKenzie, C., 2004, New insights into magnetic derivatives for structural mapping: The Leading Edge, 23 (2), 116-119.

Tarsis - Mor – 3D Magnetic Inversion Specifications

The University of British Columbia 3D magnetic inversion program, version 4.0, was used for the inversions.

The area to invert was determined by the extents of the magnetic data: 658300E, 664200E, 6660600N, 6665625N.

The original TMI data came from a Geosoft grid: Mag1_lev.grd. The topography came from the grid Dem_ml.grd. The magnetic data was gridded at 50 m cells, the topography was gridded at 20 m cells. Both grids, although being leveled, were further decorrugated by Condor Consulting prior to the inversion.

Since the data was TMI, not RTP, the magnetic field information was provided to the inversion program. For both the inducing magnetic field and the induced magnetic field, an inclination of 76.6 degrees and a declination of 26.1 degrees were used. The Earth's field strength of 57765 nT was used.

A magnetic sensor height above topography of 70 m was used. The inversion results are not considered to be highly dependent on the survey height and 5m error would not be significant.

The finite element mesh for the inversion employed a cell size of 50 m by 50 m in the east and north dimensions, and the cell height varied wrt depth. There were 119 cells in the easting, 101 in the northing. In the vertical direction, there were 33 air cells, being 20 m thick and the ground cells started at 30 m thick and progressively increased in thickness through 40 vertical cells. Depth of mesh, excluding rim & air cells, was 1500m. In addition to the cells specified above, seven rim (buffer) cells required by the finite element algorithm were used on the sides of the mesh and five added to the bottom.

Over the spatial extents of the windowed data there was negligible regional trend and only a simple 0^{th} order shift of 57421 nT was performed on the data. No further preparation of the data was required.

The error estimate provided to the inversion program was .504 nT for all data, which was 0.0001 times the standard deviation of the data plus 0.5 nT.

Two inversions were run, the first with a starting and reference model of 0.0 nT. The model from the first inversion was sharpened then used as the reference for the second inversion. The final inversion finished with the final data misfit ranging from 0.000 nT to 9.36 nT and an average of 0.303 nT. The standard deviation of the misfits was 0.399 nT.

The final finite element voxel model was trimmed by 7 cells on the east and west, 7 cells on the north, and south, and 5 cells from the bottom to removed the finite element buffer cells. The voxel model was further cleaned by nulling the voxels where there was no data.

Scott Thomas, February 4, 2009

APPENDIX D: ARCHIVE DVD

ARCHER, CATHRO & ASSOCIATES (1981) LIMITED
1016 – 510 West Hastings Street
Vancouver, B.C. V6B 1L8
Telephone: 604-688-2568 Fax: 604-688-2578



AFFIDAVIT

I, Joan Mariacher, of Vancouver, B.C. make oath and say:

That to the best of my knowledge the attached Statement of Expenditures for exploration work on CC 7-54 mineral claims on Claim Sheets 105C/1 and 8 is accurate.

Joan Mariacher

Sworn before me at Vancouver, B.C.

this 5th day of September 2008.

Notary Public, Yukon Territory

Statement of Expenditures
CC 7-54 Mineral Claims
September 4, 2008

Contract VTEM Survey

Geotech Ltd.	$46,783.41

48 claims = $974.65/claim

Geotech Ltd.

245 Industrial Parkway North, Aurora, ON L4G 4C4

BILL TO:
Archer, Cathro & Associates (1981) Limite 1016-510 West Hastings Street Vancouver, BC Canada V6B 1L8

DATE:	INVOICE:
7/30/2008	991575

TERMS:	Project
Due on receipt	8077

Description		Amount
Helicopter-borne time domain electromagnetic geophysical survey with VTEM system Interm Billing - Nintey Five (95%) of the estimated total charge plus GST is payable before receipt of prelimnary data		389,862.00
Contract (Yukon and northern BC.)		
For an estimated 2948 line km basic survey charge @$70/km	$206,360.00	
Charges per bvlock 15 blocks @$2000/block	$30,000.00	
Charges per day for estimated 51 days @$6000/day	$306,000.00	
Helicopter time chanrges for estimated 150 hours @$1800/hr	$270,000.00	
Helicopter mob/demob	$28,000.00	
Crew and equipment mob/demob	$26.000.00	
Minimum Survey Charge	$866,360.00	
95% of the Minimum Survey Charge	$823,042.00	
Less Previous Billing Invoice 991388	($433,180.00)	
Total Amount Owing	$389,862.00.	
Business Number: 110859469		

Please Remit By Bank Transfer To:
ROYAL BANK OF CANADA
3300 Highway#7 West,
Suite100,Concord,
Ontario L4K 4M3
SWIFT:ROYCCAT2
TRANSIT # 00192
ACCOUNT #1114834

Subtotal	Can$389,862.00
GST	Can$19,493.10
TOTAL	Can$409,355.10

Tel: 905-841-5004 Fax: 905-841-0611 email: info@geotech.ca